Dissertation

Alexander Fernández Scarioni
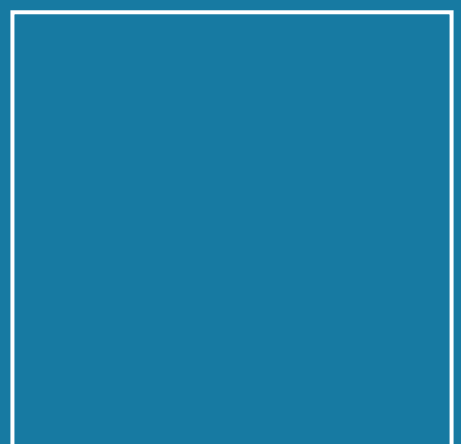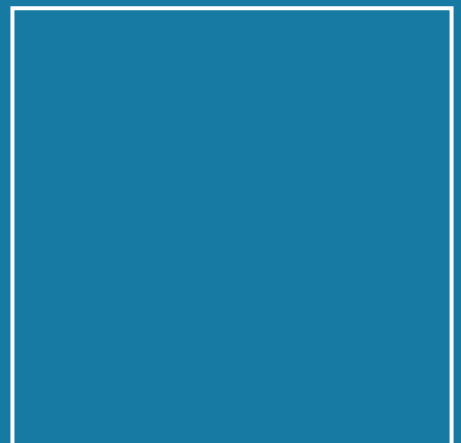
Thermoelectric measurements in magnetic nanowires

Physikalisch-Technische Bundesanstalt

Alexander Fernández Scarioni

Thermoelectric measurements in magnetic nanowires

Thermoelectric measurements in magnetic nanowires

Der Fakultät für Elektrotechnik, Informationstechnik, Physik
der Technischen Universität Carolo-Wilhelmina zu
Braunschweig

zur Erlangung des Grades eines Doktors
der Naturwissenschaften (Dr. rer. nat.)

genehmigte Dissertation

von Alexander Fernández Scarioni
aus Caracas, Venezuela

Abstract

The use of non-trivial spin textures such as domain walls and skyrmions holds promise in future applications like magnetic high-density memories and magnetic logic devices. Domain walls in perpendicular magnetized nanowires are narrow and can be driven by spin-torques. Skyrmions due to their particular non-trivial topology makes them to be robust against external perturbations, are small in size and can be driven in the same manner as domain walls with spin-torques. The precise detection of position and motion of these non-trivial spin textures is crucial for future applications. Usually the detection and characterization are performed electrically by their signature in the anomalous Hall effect (AHE), among other magneto-resistive effects. In the case of the AHE the detection is limited to Hall crosses and an electrical current is needed for the detection.

The results in this work show that thermoelectric effects such as the anomalous Nernst effect (ANE), which is the thermoelectric analogue of the AHE, allows a non-invasive measurement, detection of the position, the counting and the characterization of non-trivial spin textures. By using domain detection and observation techniques such as magneto optical Kerr microscopy and magnetic force microscopy the presence of the non-trivial spin structures in the devices is corroborated. Not only the presence of the non-trivial spin textures is verified, but also the ANE based detection is demonstrated. This allowed to detect with nanometer precision the movement of domain walls and the signature of individual skyrmions in the devices. Furthermore, a new procedure, the "two-heater" procedure, is presented which allows to separate the contributions of the different thermal gradients to the total measured thermoelectrical signal. It can be used to remove signal contributions arising from unwanted thermal gradients.

Zusammenfassung

Die Verwendung nicht-trivialer Spintexturen wie Domänenwände und Skyrmionen ist vielversprechend für zukünftige Anwendungen wie magnetische Speicher hoher Dichte und magnetische Logikbausteine. Domänenwände in senkrecht magnetisierten Nanodrähte sind schmal und können durch "spin-torques" angetrieben werden. Skyrmionen sind aufgrund ihrer besonderen, nicht-trivialen Topologie robust gegenüber äußeren Störeinflüssen, haben eine geringe Größe und können auf die gleiche Weise wie Domänenwände mit "spin-torques" bewegt werden. Die präzise Erfassung von Position und Bewegung dieser nicht-trivialen Spintexturen ist für zukünftige Anwendungen entscheidend. In der Regel erfolgt die Detektion und Charakterisierung elektrisch über ihren charakteristischen, anomalen Hall-Effekt (AHE) Beitrag oder über andere magnetoresistiven Effekte. Im Falle des AHE ist die Detektion auf Hall-Kreuze beschränkt und für die Detektion wird ein elektrischer Strom benötigt.

Die Ergebnisse dieser Arbeit zeigen, dass thermoelektrische Effekte wie der anomale Nernst-Effekt (ANE), der das thermoelektrische Analogon zum AHE ist, eine nicht invasive Messung, Positionsbestimmung, Zählung und Charakterisierung nicht-trivialer Spin- Texturen ermöglicht. Durch den Einsatz von Domänen-Detektions- und Beobachtungstechniken, wie der magnetooptischen Kerr-Mikroskopie und der Magnetkraftmikroskopie, wird zunächst das Vorhandensein nicht-trivialer Spintexturen in den Geräten bestätigt. Nach Nachweis der nicht-trivialen Spin-Texturen wird die ANE-basierte Detektion demonstriert. Dies ermöglicht es, mit hoher Präzision die Bewegung der Domänenwände und die Signatur einzelner Skyrmionen in den Proben zu detektieren. Darüber hinaus wird eine neues Verfahren, das "two-heater" Verfahren, vorgestellt, das es erlaubt, die Beiträge der unterschiedlichen thermischen Gradienten zum gesamten, gemessenen thermoelektrischen Signal zu bestimmen. Dieses kann verwendet werden, um Signalbeiträge zu diskriminieren, die durch unerwünschte thermische Gradienten entstehen.

Acknowledgments

v

Michelle, every day I appreciate more having you by my side, thank you for your love, care, support and making me a better person everyday.

Finally, a mi familia Luciana, Fidel y Javier que siempre han creído en mí y me han respaldado en las buenas y en las malas. Gracias por todo lo que me han dado hasta ahora y lo que en el futuro me van a seguir dando. No se les puede agradecer lo suficiente.

Table of contents

1. Introduction

The giant magnetoresistance (GMR) was discovered more than 30 years ago by Grünberg and Fert [1]. This remarkable breakthrough of this field of investigation led to not only important scientific investigations later, but also to the creation of magnetic field sensors that were integrated in computer hard drives enabling the reduction of the size of the hard drives. Before the discovery of GMR, such magnetic sensors were typically based on the concepts of anisotropic magnetoresistance (AMR) and Hall effects [2]. The GMR allowed to reduce the size and the power efficiency in comparison to the available magnetic sensors . This set a milestone in the research field that is today called spintronics [3]. The field of spintronics studies the spin of the electron and its potential applications in magnetic sensors and memories. The rapid reduction of the sensor size and the memories over the years brought a new problem concerning the ohmic energy dissipation arising from the conducting circuits. However, this "waste" heat generated from these circuits might also be used to manipulate the spin state using temperature gradients and thermally generated spin currents. The combination of spintronics with temperature gradients gave rise to a field called spin caloritronics [4]. This field addresses the phenomena that involve spin, charge, entropy and energy transport in spintronic devices driven by thermal gradients. Some of the thermoelectric effects that are studied in the field of spin caloritronics are: the anisotropic magneto-Seebeck (AMS) effect [5], planar Nernst effect (PNE) [6] and anomalous Nernst effect (ANE) [7]. In general, these different effects arise from the geometrical dependency of the orientation between the magnetization of the spins with respect to the thermal gradient.

The thermoelectric effects have an advantage in comparison to the resistive based effects: Here, no electric current through the device and hence no leads are needed to generate the effect since the signal is generated by thermal currents. Also, the temperature needed to create a sufficiently large thermal gradient could be only of the order of a few milli Kelvins. This allows to produce the heat by means of Joule heating of a metallic stripe next to the devices where low currents are sufficient to generate the corresponding temperature increase. This way it was possible to thermoelectrically

1

detect the signature of single non-trivial spin structures such as single magnetic domain wall in a permalloy nanowire [5]. Here, other experimental methods such as magneto-optical Kerr (MOKE) microscopy [8] are limited in spatial resolution, whereas high resolution imaging methods such as magnetic force microscopy (MFM) [9] can be time consuming and invasive. Thus, thermoelectric measurements provide a tool for a non-invasive single shot measurements to detect and characterized individual nano-scale non-trivial structures.

Depending on the measurement geometry and orientation of the heat gradient different thermoelectric effects like the Seebeck- and the Nernst effect become relevant can be detected. However, thermal gradients are usually not as well defined as the current paths in an electrical transport experiment. This makes it difficult to measure the signal of interest without artifacts resulting from ill-defined thermal gradients. This problem has been addressed in experiments that involve the spin Seebeck effect [10–13], where the ANE a spin dependent effect rises due to an unwanted component of the thermal gradient. As a consequence, the signal due to the ANE can obscure the spin Seebeck effect and can hinder the correct data interpretation. To avoid this, complex substrate-free or membrane based devices need to be fabricated [10]. By using such measurement setups where the direction of the thermal gradient is well defined the different thermoelectric effects can be measured simultaneously [14]. However, the complex sample structures limits the application and hinders wide spread applications. Therefore, in Chapter 4 a new methodology is explored that allows to separate and quantify the thermoelectrical contributions of the different thermal gradients of thermoelectric measurements using easily accessible substrate-based samples.

Novel magnetic memory concepts use the advantage of materials with perpendicular magnetization anisotropy (PMA) to scale down the memories in order to reach higher storage densities [15]. These magnetic memories rely on controllably positioning and propagating of domain walls. Resistive effects such as the anomalous Hall effect (AHE) allow to detect domain walls with high precision. However, the Hall effect is only sensitive within the Hall cross, whereas outside the cross no detection is possible. Here, as shown in Chapter 5, the thermoelectric effects can provide a new tool to overcome this problem and allow to precisely detect the position and motion of a magnetic domain wall inside a magnetic wire.

Non-trivial spin structures like magnetic skyrmions [16, 17] have been a recent focus of spintronics research both with respect to fundamental spin properties as well as potential applications. Skyrmions were proposed to replace domain walls in future

magnetic memories as information carrying objects since they are robust due to their topology [18]. This new concepts has been discussed under the name skyrmion race-track memory [19, 20]. In such memory skyrmions can be moved efficiently by electrical currents [21] making them also promising candidates for novel logic type devices [22]. Recently, skyrmions have been stabilized at room temperature in multilayer materials systems [23]. Also, their electrical characterization and manipulation have been intensely investigated over the last years [23–31] leading to observations such as the skyrmion Hall effect [32, 33] and the topological Hall effect [16, 31]. But, the thermo-electrical properties of skyrmions have only been addressed in very few studies [34–37]. Further experimental investigations into thermally induced phenomena could indicate topological contributions to the Nernst effect [38] and could provide a new toolkit for skyrmion detection and manipulation. Chapter 6 of this thesis is devoted to experimentally demonstrate that spin dependent thermoelectric effects can be used as a tool to detect, count, and characterize individual skyrmions in magnetic micro- and nano-wires.

This thesis thus presents thorough experimental studies of thermoelectric properties of non-trivial nano-scale magnetic textures like domain walls and skyrmions in magnetic micro- and nanowires.

The content of this thesis is organized as follows:

Chapter 2 provides the theory needed to understand the concepts and definitions used in this thesis. This includes the physics and concepts of ferromagnetic models, domain walls and magnetic skyrmions. The chapter ends with the magnetoresistive effects and magneto-thermoelectric effects relevant for this work and their respectively equations.

In **Chapter 3**, the experimental techniques employed are listed and explained. Beginning with the fabrication of the devices, the experimental procedure for the thermovoltage measurements, and ending with the domain detection and observation techniques. At the end of the chapter the different thermoelectrical measurement setups are described.

In **Chapter 4**, the "two-heater" procedure is introduced that allows to separate the thermoelectrical contributions of the different components of the thermal gradients in the thermoelectrical data. The consequences of unwanted thermal gradients are explained, the "two-heater" procedure is explained and the importance of having two balanced heaters is underlined. At the end of the chapter the procedure is experimentally applied to characterize the thermoelectrical response of a saturated permalloy

nanowire.

Chapter 5 shows a study of the detection of domain walls using the anomalous Nernst effect. Firstly, the device under test, a ferromagnetic semiconductor microwire with perpendicular magnetic anisotropy, is characterized by measuring the ANE depending on the internal magnetization of the microwire. Then, the magnetic field driven domain wall motion is thermoelectrically measured and compared with magneto optical Kerr microscopy and ANE voltage measurements. Then, a similar experiment is repeated by moving the domain wall by means of spin-torque. Thermal finite element modelling of the temperature increase produced by the heater is presented at the end of the chapter.

In **Chapter 6**, the detection and characterization of single skyrmions by measuring the ANE in combination with magneto force microscopy measurements is presented. First, the device in the measurements is described and the controlled nucleation of skyrmions in the microwire is investigated. A concept using a magnetic force microscope probe to controllably annihilate skyrmions in the microwire is presented allowing to reduce the number of skyrmions in the wire one by one. This mechanism is then applied to study the anomalous Nernst effect contribution of few and single skyrmions. For the detailed data analysis MFM measurements are used to derive the area of the skyrmions and to relate it to the skyrmion's Nernst signal. Based on this the measured thermoelectrical signal can be attributed to the anomalous Nernst effect of the reversed spin structure of the skyrmion. Additionally, the magnetic field dependence of the Nernst response of single skyrmions is studied. At the end of the chapter possible contributions of a topological Nernst effect in the measurement data are discussed.

In **Chapter 7**, presents a summary and the major conclusions obtained from the measurements.

2. Theoretical background

This chapter provides a theoretical basis for the comprehension of the physical phenomena discussed in this thesis. After the description of some concepts in ferromagnetism and some ferromagnetic models, the concept of domain walls and their dynamics is introduced. Also, the concept of magnetic skyrmion is introduced, where due to the competition between different interactions such as the Heisenberg exchange and the Dzyaloshinskii-Moriya interaction, these non-trivial magnetic structures appear in materials with high spin-orbit interaction and broken inversion symmetry. At the end of the chapter themagneto-thermoelectric effects relevant for this thesis and their respectively equations are introduced, which are explained parting from the transport equations known from anisotropic magnetoresistance effects and Hall effects.

2.1. Magnetic materials

The magnetic properties of any material can be characterized by the magnitude and sign of its magnetization M. Another way to characterize the magnetic properties is to observe how M varies as a function of a uniform field H. The ratio between these two quantities is called susceptibility χ:

$$\chi = \frac{M}{H} \tag{2.1}$$

χ is dimensionless since M has units of $\mathrm{A\,m^{-1}}$, and H has units of $\mathrm{A\,m^{-1}}$. When measurements M of as a function of H (magnetization curves) are performed other parameters such as the saturation magnetization M_s can be obtained. The parameter M_s describes the value of M when at high enough values of H, M becomes constant even as H is still increases. In general the magnetic behavior of different materials can be characterized by its corresponding χ value [39]:

5

- Empty space: $\chi = 0$.

- Diamagnetic materials: χ is small and negative.

- Paramagnetic and antiferromagnetic materials: χ is small and positive.

- Ferromagnetic and ferrimagnetic materials: χ is large and positive and both are functions of H.

The hysteresis is another characteristic feature of ferromagnets. When after M_s is reached, a decrease of H to zero does not reduce M to zero.

The magnetic materials used in the experiments in this thesis were ferromagnetic metals and ferromagnetic semiconductors. The basic concepts to understand the physics behind these materials are going to be introduced next.

2.1.1. Ferromagnetism

Ferromagnetic materials are characterized by a long-range ordering of their atomic moments, even in the absence of an external magnetic field. The physical reason of the spontaneous ordering of the magnetization in ferromagnetic materials lies in the quantum mechanical exchange interaction due to the orientation of the spins of the electrons. The spontaneous, long-range magnetization of a ferromagnet is observed to vanish above an ordering temperature that is called the Curie temperature T_C [40]. Pierre Curie found that the susceptibility was independent of the temperature for diamagnetic materials, but that it varied inversely with the absolute temperature for paramagnetic materials $\chi = C/T$, where C is the Curie constant, this relation is called the Curie law.

In the case of a ferromagnetic materials, above its Curie temperature, the ferromagnetic material becomes paramagnetic. This is because, the magnetic moments are oriented randomly, resulting in a zero net magnetization, and its susceptibility follows the Curie-Weiss law $\chi = C/(T - T_\mathrm{C})$ [39]. In this equation, T_C is a constant that has a finite and positive value. The Curie-Weiss law can be derived on the assumptions made by Pierre Weiss, who proposed that a molecular field acts in a ferromagnetic material below its Curie temperature as well as above, and that this field is so strong that it can magnetize the material to saturation even in the absence of an applied magnetic field. Pierre Weiss also proposed that a ferromagnetic material in the demagnetized

state is divided into a number of small regions called domains. This idea arise due to the question in why some ferromagnetic materials are unmagnetized. Therefore, he proposed that, each domain is spontaneously magnetized to the saturation value M_s, but the directions of the magnetization of the various domains are such that the specimen as a whole has no net magnetization. The boundary that separates the different domains was called domain wall. Then, the process of magnetization is one of converting the ferromagnetic material from a multi-domain state into one in which it possesses a single domain magnetized in the same direction as the applied field. The two postulates (spontaneous magnetization and division into domains) proposed by Weiss led to what today is called the molecular field theory.

In the molecular field theory or also called mean field theory, the molecular field H_w is proportional to the magnetization, $H_w = \beta M$, where β is the molecular field constant. In a ferromagnetic material, the magnetic moments are exposed to a field that is the sum of the external magnetic field H and the molecular field H_w. The molecular field theory can be explained better by considering the case where the atomic moments are generated by a single unpaired electron of spin $s = 1/2$. The temperature dependence of the magnetization of a ferromagnetic material can be expressed using the so called Brillouin function according to the following manner [41]:

$$M^* = \frac{M(T)}{M(0)} = \tanh\left[\frac{\mu_B (H + \beta M(T))}{\kappa_B T}\right] \tag{2.2}$$

$$M^* = \frac{M(T)}{M(0)} = x = \frac{\mu_B (H + \beta M(T))}{\kappa_B T} \tag{2.3}$$

where κ_B is the Boltzmann constant, μ_B the Bohr magneton and x is a parameter introduced for simplicity. The saturation magnetization corresponding to zero temperature is given by $M(0) = N\mu_B$, where N is the volume density of the spins. Also, the relative magnetization parameter is included M^* with values of $0 \leq M^* \leq 1$. This parameter makes the theory independent of specific material properties due to the variation of the magnitude of the spontaneous magnetization.

In figure 2.1 the relative magnetization M^* as a function of the reduced temperature $T^* = T/T_C$ is shown. The spontaneous magnetization is calculated by considering the limit $H \to 0$ when both equations 2.2 and 2.3 are satisfied simultaneously. By solving this, it is found that at a certain temperature T_C (the curie temperature), M^* disappears abruptly. But when $T \to 0$, M^* converges to a value of 1. The value of

T_C is obtained by finding the interception between equation 2.2 and equation 2.3 when $H = 0$ and in the limit when $x \to 0$. For small values of $x \to 0$ the expression for T_C for $s = 1/2$ is obtained:

$$T_{\mathrm{C}} = \frac{N\mu_{\mathrm{B}}^2 \beta}{\kappa_{\mathrm{B}}} = \frac{\mu_{\mathrm{B}}}{\kappa_{\mathrm{B}}} \beta M\left(0\right) \tag{2.4}$$

by using this equation, the molecular field can be estimated in materials with atomic spins $s = 1/2$, using the simple expression of $H_{\mathrm{w}} = \kappa_{\mathrm{B}} T_{\mathrm{C}}/\mu_{\mathrm{B}}$.

Figure 2.1. – The realtive magnetization M^* as a function of the reduced temperature T^* derived for a $s = 1/2$ and for a macrospin with no quantization as derived from the Langevin function. Figure taken from [41].

In the theory of Weiss, the molecular field constant β needs to have a large value to agree with the high values of T_C that were found in nature. If only dipole fields were considered, it was not possible to find an internal field which needs to be in the order of $\approx 10^3$ T to account for the Curie temperature of iron [42].

Long after Weiss proposed his theory, Heisenberg showed that it was the exchange interaction, which involves large Coulomb energies, which is responsible for this large molecular field. In section 2.1.2 an insight in the exchange interaction is going to be presented. The theory described above is based on the Curie-Weiss model or also called molecular field theory of a ferromagnet.

2.1.2. Energies in magnetic systems

The micromagnetism theory of magnetic materials is based on a variational principle derived from thermodynamic principles that started with the paper by Landau and Lifshitz in 1935. This theory describes the spatial dependence of the magnetization $M(x, y, z)$ when the total free energy of the system reaches an absolute or relative minimum. In a magnetic material the total free energy can obtained by imposing a minimum on the Gibbs free energy and is expressed by:

$$E_{\text{tot}} = U - \mu_0 \int_V \mathbf{M} \cdot \mathbf{H}_{\text{ext}} \, dV \tag{2.5}$$

where U, $\mathbf{M}$ and $\mathbf{H}_{\text{ext}}$ denote the internal energy, local magnetization and an external magnetic field, respectively. If the magnetoelastic energy is not considered, the total energy can be written as:

$$E_{\text{tot}} = E_{\text{ex}} + E_{\text{K}} + E_{\text{D}} + E_{\text{H}} + E_{\text{DM}} \tag{2.6}$$

where E_{ex}, E_{K}, E_{D}, E_{H} and E_{DM} are the exchange, anisotropy, demagnetization, Zeeman and asymmetric exchange energies, respectively [43]. The free energy is the essence of the micromagnetism theory where the interplay the different energy contributions determines the magnetic microstructure such as the domain structure. The different energy contributions are going to be discussed briefly.

Exchange energy

The exchange interaction results from the quantum mechanical interaction between the spins of the electrons. This interaction is a consequence of the Pauli exclusion principle, applied to the two atoms as a whole. This principle states that two electrons can have the same energy only if they have opposite spins [39]. The exchange interaction can be divided into different classes, in this thesis the Heisenberg exchange interaction or sometime called symmetric exchange interaction and the asymmetric exchange interaction are described.

The Heisenberg exchange interaction favors the alignment between neighboring electronic spins, which allows to form magnetic domains where the magnetization is uniform. The Hamiltonian according to the Heisenberg model can be expressed as follows:

$$H_{\text{ex}} = \sum_{i,j} J_{i,j} \, \mathbf{S}_i \cdot \mathbf{S}_j \qquad (2.7)$$

where $J_{i,j}$ is the exchange constant between the two spins and $\mathbf{S}_i$ and $\mathbf{S}_j$ are the moments of two adjacent spins. For a ferromagnet $J_{i,j}$ is positive (spins parallel to each other) whereas for an antiferromagnet it is negative (spin opposite to each other). By means of Taylor expansion of the equation 2.7, an approximate expression for the exchange energy is obtained:

$$E_{\text{ex}} = A \int_V \left[(\nabla m_x)^2 + (\nabla m_y)^2 + (\nabla m_z)^2 \right] dV \qquad (2.8)$$

where m represents the magnetization along the different spatial directions. The parameter $A = \left(2nJS^2\right)/x$ is the exchange stiffness constant with n the number of atoms per unit cell and x is the nearest-neighbor distance. This energy tends to reduce the magnetization gradient.

The asymmetric exchange interaction is directly related to the spin-orbit interaction. It appears in materials where the inversion symmetry is broken, in their lattice or at the interfaces of the material structure. This exchange interaction is usually called Dzyaloshinskii-Moriya interaction (DMI), and its corresponding Hamiltonian can be written as:

$$H_{\text{DM}} = \sum_{i,j} \mathbf{D}_{i,j} \cdot [\mathbf{S}_i \times \mathbf{S}_j] \qquad (2.9)$$

where $\mathbf{D}_{i,j}$ is the Dzyaloshinskii vector. One difference in comparison to the Heisenberg exchange is that the DMI prefers a perpendicular alignment of the spins in order to minimize its cross product. Usually in some materials the DMI and the Heisenberg exchange compete against each other and the governing determines the behavior of the magnetization. The corresponding term of the DMI in the free energy is:

$$E_{\text{DM}} = \int_V D \left[\mathbf{M} \cdot (\nabla \times \mathbf{M}) \right] dV \qquad (2.10)$$

where D is the effective DMI constant which favors non-uniform magnetic structures. One type of magnetic structures that can be formed in the presence of the DMI are magnetic skyrmions, this is going to be discussed in detail in section 2.1.3.

Magnetostatic energies

When a magnetic material is placed in the presence of a magnetic field $\mathbf{H}_{\text{ext}}$, the magnetic moment tends to align to the applied magnetic field. When the moments are aligned with the magnetic field the energy is minimal. The energy that describes this process is called Zeeman energy and can be expressed as follows:

$$E_{\text{H}} = -\mu_0 \int_V \mathbf{M} \cdot \mathbf{H}_{\text{ext}} \, dV \tag{2.11}$$

The Zeeman energy depends on the average magnetization of the material and not on the internal domain structure or the shape of the sample. There is also an energy associated with the magnetic field generated by the magnetic material by itself, which is called stray field energy. When the external field is zero, the divergence of the stray field $\mathbf{H}_{\text{D}}$ is equal to the divergence of the magnetization of the material $\nabla \mathbf{H}_{\text{D}} = -\nabla \mathbf{M}$, according to Maxwell's equations. The stray field energy can be expressed as follows:

$$E_{\text{D}} = -\frac{1}{2} \mu_0 \int_V \mathbf{M} \cdot \mathbf{H}_{\text{D}} \, dV \tag{2.12}$$

In the particular case of ferromagnetic materials, to minimize the stray field energy the ferromagnetic material transforms its uniform magnetization into domains that are oriented along different directions.

Anisotropy energies

The energy of a ferromagnet depends on the direction of the magnetization relative to the structural axis of the material. An additional energy term arises when the magnetization is oriented in a direction that is different from the structural axis, this structural axis is usually called easy axis. The name of this additional energy is anisotropy energy. Depending on the material, different anisotropies might arise that correspond to different anisotropy energy terms. Briefly the shape, uniaxial, cubic and the surface anisotropy energy are going to be described.

The energy term due to the demagnetization energy associated with the sample shape is referred to as the shape anisotropy. The shape anisotropy arises due to the dipole-dipole interaction between the magnetic moments. Due to the shape of the samples some magnetic moments can be uncompensated, as an example at the surface and at

the sample borders. This generates a demagnetization field $\mathbf{H}_{\mathrm{D}}$. When the sample has the shape of an ellipsoid the demagnetization field can be expressed as:

$$\mathbf{H}_{\mathrm{D}} = -\hat{\mathrm{D}}\mathbf{M} \tag{2.13}$$

where $\hat{\mathrm{D}}$ is a tensor called the demagnetization tensor and the elements inside the tensor as demagnetization factors. If $\mathbf{M}$ is parallel to one of the principal axis of the ellipsoid, then $\hat{\mathrm{D}}$ is a number and it is called demagnetizing factor. The trace of the tensor $\hat{\mathrm{D}}$ is 1. Equation 2.13 and 2.12 can be combined and the magnetostatic energy density for an ellipsoid can be expressed as [44]:

$$E_{\mathrm{D}} = \frac{1}{2}\mu_0\mathbf{M}\hat{\mathrm{D}}\mathbf{M} \tag{2.14}$$

If the principal axes of the ellipsoid a, b, c lie on the x, y and z axes respectively, and θ and ϕ represent the polar and the azimuthal angles respectively, equation 2.14 can be rewritten as:

$$E_{\mathrm{D}} = \frac{\mu_0 M_s^2}{2}\left(D_x \sin^2\theta\cos^2\phi + D_y\sin^2\theta\sin^2\phi + D_z\cos^2\theta\right) \tag{2.15}$$

If the ellipsoid is assumed to be infinite along the x-y plane, so that a,b $\to\infty$ and c $\to 0$, thus meaning that $D_x, D_y = 0$ and $D_z = 1$, equation 2.15 simplifies to:

$$E_{\mathrm{D}} = \frac{\mu_0 M_s^2}{2}\cos^2\theta \tag{2.16}$$

This shows that the form anisotropy in thin films favors the orientation along the plane of the sample. To orient the magnetization perpendicular to the sample plane would require high magnetic films, so that in thin films the component perpendicular to the sample plane can be neglected. With this knowledge equation 2.15 can be simplified to:

$$E_{\mathrm{D}} = \frac{\mu_0 M_s^2}{2}\left(D_x\cos^2\phi + D_y\sin^2\phi\right) = \frac{\mu_0 M_s^2}{2}\left(D_x + (D_y - D_x)\sin^2\phi\right) \tag{2.17}$$

The part of the equation that does no depend on the rotations angle can be omitted since it gives a constant offset in the energy. Thus, equation can be expressed as follows:

$$E_{\mathrm{D}} = K_{\mathrm{D}} \sin^2 \phi \qquad (2.18)$$

with $K_{\mathrm{D}} = \mu_0 M_s^2 \left(D_y - D_x\right)/2$. This energy term is usually described as the uniaxial anisotropy term denoted with $E_{\mathrm{K,uni}} = K_{\mathrm{u}} \sin^2 \phi$. The shape anisotropy of an ellipsoid in particular has a uniaxial anisotropy character with an anisotropy constant, being the anisotropy constant K_{D} dependent on the ratio between the two axes of the ellipsoid (D_x and D_y). The longest of the two axis would then describe the easy axis.

In the case for samples that show a shape anisotropy with cubic anisotropy character, the anisotropy can be described by [45]:

$$E_{\mathrm{K,cubic}} = \int_V \left[K_{\mathrm{c1}} \left(m_1^2 m_2^2 + m_1^2 m_3^2 + m_2^2 m_3^2 \right) + K_{\mathrm{c2}} \left(m_1^2 m_2^2 m_3^2 \right) + \cdots \right] dV \qquad (2.19)$$

where m_i are the magnetization components along the cubic axes. In most cases the higher order terms such as K_{c2} can be neglected. Depending on the sign of K_{c1}, the easy axis is oriented along the $\langle 100 \rangle$ or the $\langle 111 \rangle$ crystallographic direction.

The surface anisotropy becomes relevant in materials that consist of thin films or multilayers. Since this anisotropy is very sensitive to the thickness and to the covering of the magnetic material with a non-magnetic material, it allows to change the magnetic properties of the material and make it possible to fix the magnetization along one axis. The energy that corresponds to the surface anisotropy can be written in first approximation by two independent quantities as:

$$\begin{aligned} E_{\mathrm{K,s}} = \int_S \Big[&K_{\mathrm{s1}} \left(1 - m_1^2 n_1^2 - m_2^2 n_2^2 - m_3^2 n_3^2 \right) \\ &- 2 K_{\mathrm{s2}} \left(m_1 m_2 n_1 n_2 + m_1 m_3 n_1 n_3 + m_2 m_3 n_2 n_3 \right) \Big] dS \end{aligned} \qquad (2.20)$$

where n is the surface normal. Notice that the energy is integrated over the surface in comparison to the other energies described before. When the two anisotropy coefficients are equal $K_{\mathrm{s1}} = K_{\mathrm{s2}}$, which is the case for an isotropic medium the energy can be rewritten in first order approximation as follows:

$$E_{\mathrm{K,s}} = \int_S K_{\mathrm{s}} \left[1 - (\mathbf{m} \cdot \mathbf{n}) \right] dS \qquad (2.21)$$

13

for positive values of K_s the magnetization is oriented parallel along the direction of the surface. In the next section it will be discussed how this specific anisotropy is used to induce a perpendicular magnetic anisotropy in ferromagnetic materials.

2.1.3. Perpendicular magnetic anisotropy

In magnetic films when the thickness of the films is changed, or the thickness of its individual layers, or by combining it with non-magnetic materials, the anisotropy also changes. This allows by varying the thickness of individual layers of the magnetic material and choosing appropriate materials, it is possible to tailor the magnetic anisotropy. The phenomenon when the magnetization changes from the commonly observed in-plane orientation in magnetic films to the direction perpendicular to the plane, is called perpendicular magnetic anisotropy (PMA) [46].
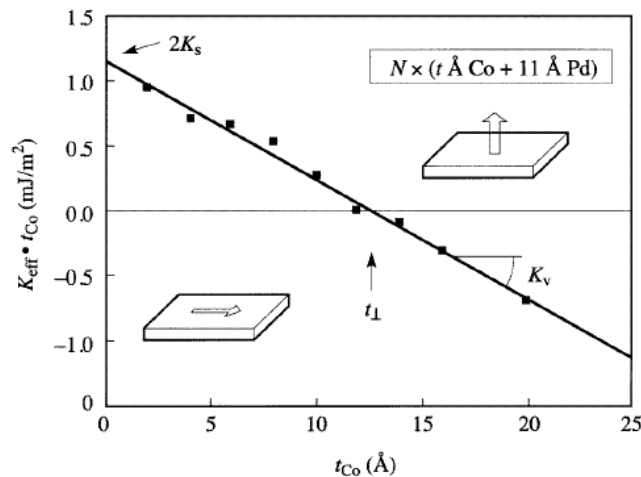
Figure 2.2. – Magnetic anisotropy energy times the individual Co layer thickness versus the individual Co layer thickness of Co/Pd multilayers. The rectangles with the arrows indicate at which thickness the magnetization changes from in-plane to perpendicular to the plane. Figure taken from [46].

In 1954 Néel introduced a phenomenological model where the effective magnetic anisotropy energy K_{eff} could be separated in a volume contribution K_V and a contribution from the interfaces K_s that in approximation obeyed the relationship:

$$K_{\text{eff}} = K_V + 2K_s/t \rightarrow K_{\text{eff}}t = tK_V + 2K_s \tag{2.22}$$

14

where t represents the thickness of the magnetic layer. The factor 2 that multiplies K_s arises since the layer is assumed to be bounded by two identical interfaces. Also, the relation is presented under the convention that K_s/t represents the difference between the anisotropy of the interface atoms with respect to the inner or bulk atoms. Experimentally the determination of K_V and K_s is obtained by plotting the product of $K_{eff}t$ vs t. In figure 2.2 one example of an Co/Pd multilayer is shown. The slope of the curve is negative, this means that K_V is negative, favoring in-plane magnetization. At zero t, K_s is positive which favors perpendicular magnetization. This means that at a critical $t = -2K_s/K_V$ the surface anisotropy outweighs the volume anisotropy and the results is that the film is no longer magnetized in-plane but perpendicular to the plane.

2.1.4. Ferromagnetic semiconductor

The interest in ferromagnetic semiconductors arose due to the possibility of combining the semiconducting and ferromagnetic properties in the same device. In memory elements, magnetic storage and the logic are two separated architectures based on different materials. A ferromagnetic semiconductor device could not only solve technical issues such as the heat dissipation generated by transferring information between the two architectures, but also could offer the possibility of a fully nonvolatile information processing system [47]. The discovery of ferromagnetism at relatively high temperatures ($T_C > 100K$) in diluted magnetic semiconductors (DMS) derived from technologically important III–V compounds InAs and GaAs gave researchers the opportunity to use these materials in spintronic devices [48].

One of the best understood DMS is (Ga,Mn)As (see figure 2.3 for its crystallographic structure), when Mn is substituted for Ga in a GaAs lattice, it acts as an acceptor, providing holes that mediate a ferromagnetic interaction between the local moments of the open d shells in the Mn atoms. To have an ferromagnetic order in (Ga,Mn)As a minimum of 2% of the Ga ions need to be replaced by Mn ions, so that a sufficient carrier density of the carriers is provided. These films are usually grown by molecular beam epitaxy at low temperatures of $T_{substrate} \approx 250$ °C, to incorporate a large concentration of Mn in the GaAs lattice without forming inclusion of the thermodynamically more stable metallic MnAs. This fabrication method results in a high density of point defects, and the most important of these are known as As anti-sites and Mn interstitials that act as double donors, reducing the hole concentration [48].

The ferromagnetism in (Ga,Mn)As can be explained trough the Zener model [49]. This model describes using the double-exchange magnetic interaction the hole-mediated ferromagnetism in (Ga,Mn)As. When the magnetic ion Mn is substituted for Ga in (Ga,Mn)As, it acts as an acceptor and at the same time it provides a localized spin. The Mn acceptors compensate the crystallographic defects that are present in GaAs grown by low-temperature molecular beam epitaxy and produce a p-type conduction. The holes provide a ferromagnetic interaction between the local moments of the open d shells in the Mn atoms. Because of the spin orbit interaction the carriers become spin polarized to lower their free energy. At lower temperatures the free energy is higher than the energy that is necessary to polarize the localized spins. This means that below at a certain temperature (Curie temperature) the ferromagnetic alignment becomes energetically favorable. The findings in this theory has served to describe the T_C as a function of the carrier density and the Mn concentration.
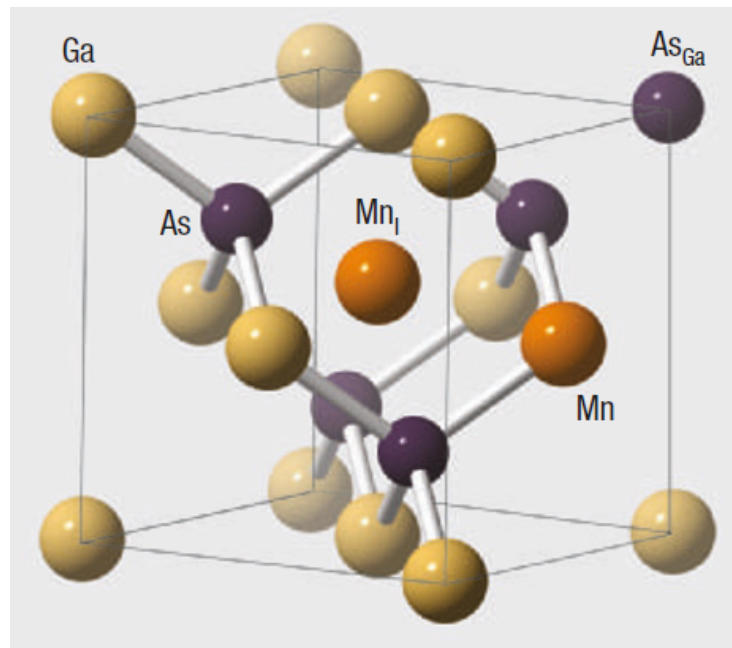
Figure 2.3. – Crystal structure of (Ga,Mn)As. As_{Ga} is an As anti-site and Mn_I represents a Mn interstitial. Figure taken from [48].

2.2. Domain walls

In section 2.1.1, it was already introduced that the ferromagnetic materials can split into different domains separated by domain walls. In general, ferromagnetic domains

16

form to minimize the stray field energy.

A representation of domain walls is shown in figure 2.4. Domain formation often leads to flux closure of the magnetization to reduce the dipolar (stray field) energy. The domain walls can be classified according to the angle between the magnetization of the two domains. There are 180° and 90° domain walls as is shown in figure 2.4a, the 180° domain wall separates domains with opposite magnetization and a 90° domain wall separates domains of perpendicular magnetization [42].
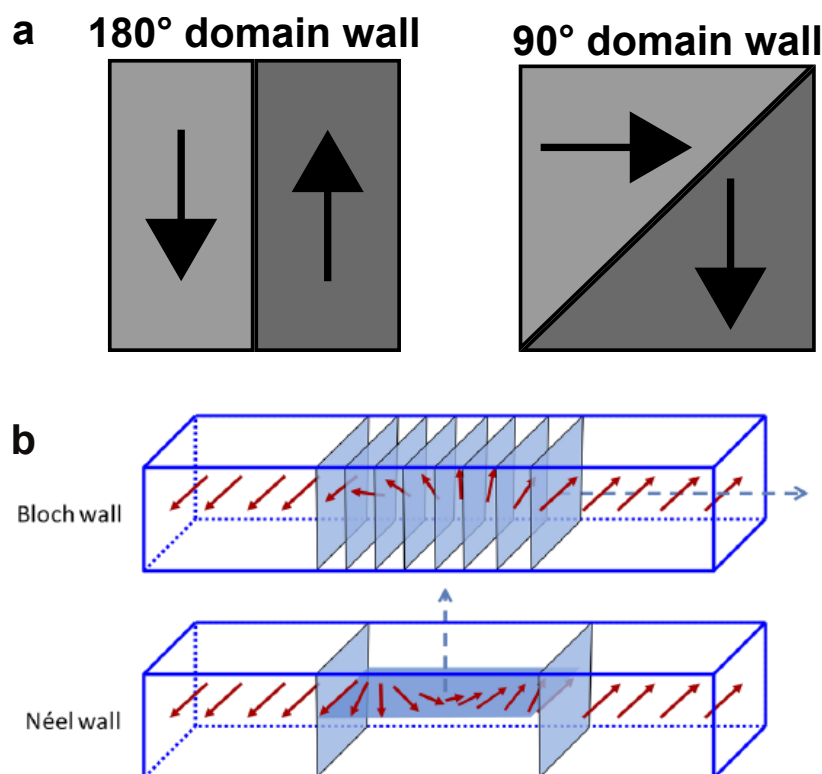
Figure 2.4. – Domain walls. **a**, sktech of a 180° and a 90° domain wall. **b**, representation of a Bloch and Néel domain wall. Figure adapted from [50].

The most common type of domain walls are the 180° domain walls, they can be separated into two different types: Bloch walls and the Néel walls, as shown in figure 2.4b. In Bloch walls the magnetization rotates parallel to the plane of the wall, whereas in a Néel wall the magnetization rotates perpendicular to the plane of the wall. Bloch walls are more common in bulk-like thick films, while Néel walls often occur in thin films [41]. The characteristics of a Bloch domain wall are discussed briefly next.

Let's assume that a 180° Bloch domain wall is in an infinite uniaxial medium with

negligible magnetostriction, separating two domain of opposite magnetization [45]. In equation 2.8 the exchange energy, for a pair of atoms of the same spin can be rewritten in the following way [39]:

$$E_{\text{ex}} = -2JS^2 \cos \phi_{\text{ij}} \tag{2.23}$$

Since a continuum medium was assumed the expression can be written as:

$$E_{\text{ex}} = -2A \cos \frac{d\phi}{dx} \tag{2.24}$$

where $A = \left(2nJS^2\right)/x$ is the exchange stiffness described in section 2.1.2. The $d\phi/dx$ quantity represents the rate at which the direction of local magnetization rotates with the position in the wall. The expression in equation 2.24 can be change by assuming that ϕ is small and by series expansion of the cosine, the equation can be written as:

$$E_{\text{ex}} = -2A + A \left(\frac{d\phi}{dx}\right)^2 \tag{2.25}$$

The first term in equation 2.25 does not depend on the angle ϕ so it can be neglected, therefore the extra energy within the wall is given by:

$$E_{\text{ex}} = A \left(\frac{d\phi}{dx}\right)^2 \tag{2.26}$$

In general, the anisotropy energy can be written as $E_{\text{K}} = g\left(\phi\right)$, where ϕ is measured from the easy axis. Depending on the type of anisotropy (uniaxial or cubic) the term $g\left(\phi\right)$ changes. The wall energy is then given by the sum of the exchange energy and the anisotropy energy, integrated over the wall thickness:

$$\sigma_{\text{wall}} = \int_{-\infty}^{\infty} \left[A \left(\frac{d\phi}{dx}\right)^2 + g\left(\phi\right)\right] dx \tag{2.27}$$

The width of the domain can be calculated by minimizing equation 2.27. The thickness of the domain wall is formally infinite. An effective wall thickness can be defined as the thickness of a wall with constant value of $d\phi/dx$ equal to that at the center of the

wall. For a uniaxial anisotropy, the slope $d\phi/dx$ has its maximum value $\sqrt{A/K_{\mathrm{u}}}$ at the center of the wall, so the effective domain wall thickness for this case is:

$$x_{\mathrm{wall}} = \pi\sqrt{\frac{A}{K_{\mathrm{u}}}} \tag{2.28}$$

Here in this equation is clear to see that the width of the domain wall is a competition between the exchange energy and the anisotropy energy.

2.2.1. Domain wall dynamics: field driven and current driven domain wall motion

In the previous section it was discussed that the exchange, dipolar, and anisotropy energy compete in ferromagnetic materials to stabilized domains. When stable, the domains, have a specific alignment along the material, up or down as an example. If a magnetic field is applied in the up direction, the magnetic moments in the material that are oriented in the up direction are going to be energetically favored (due to the Zeeman energy) in comparison to the magnetic moments oriented down. Causing the up moments to expand, in other words, the down moments reorient in the direction of the applied field and the domain wall moves its position. This is called domain wall motion. The domain walls can be moved by magnetic fields (field driven domain wall motion) and by electrical currents (current induced domain wall motion) due to current induced transfer of angular momentum also called spin torque [51, 52].

The temporal evolution of the magnetization in magnetic materials or their dynamics, can be described by the Landau-Lifschitz-Gilbert (LLG) equation which establishes that the temporal evolution of the magnetization is equal to all the torques that act on the magnetization, the equation can be written:

$$\frac{d\mathbf{m}}{dt} = -\gamma\left(\mathbf{m} \times \mathbf{H}\right) + \frac{\alpha}{M_s}\left(\mathbf{m} \times \frac{d\mathbf{m}}{dt}\right) \tag{2.29}$$

where γ is the gyromagnetic ratio, m_{s} the saturation magnetization and α is known as the Gilberts damping parameter. In this equation H is the effective field ($H = H_{\mathrm{eff}}$) that acts on the magnetization including all anisotropy fields. In figure 2.5 is shown an illustration of the precession of the magnetization m according to equation 2.29. The

first term in equation 2.29 represents the precession of m at a fixed angle θ around H (marked as T in figure 2.5), and the second term describes m due to a damping torque T_D, which causes that m orients in the direction of H. The dynamics of the domain walls follow the LLG equation 2.29, which is going to be explained briefly later.
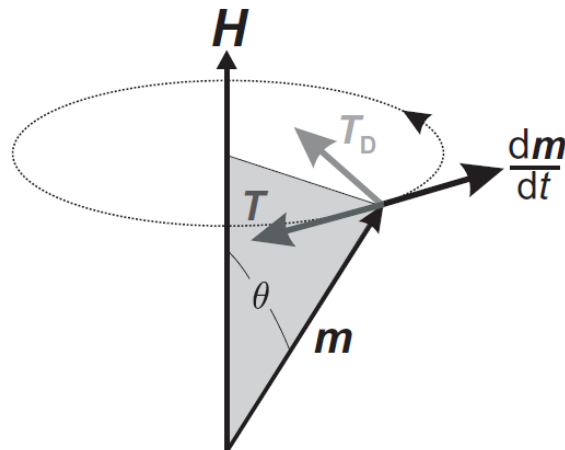
Figure 2.5. – Representation of the torques acting on the precessing magnetization in the presence of a magnetic field H. T represents the precesional torque and T_D the damping torque. Figure taken from [41].

Before describing the two mechanism of domain wall motion, one important point is to address the effect of pinning. One example of pinning is imperfections in magnetic thin films, which modify how the domain wall moves. When pinning is present the motion of the domain wall is thermally activated, and the velocity of the domain depends on the driving force. In figure 2.6a three different regimes are represented for the domain velocity according to the driving force and the temperature. At zero temperature the domain wall would be pinned for all depinning forces f, below the depinning force f_{dep}, at which a critical depinning transition occurs. At finite temperatures the depinning transition becomes obscured due to thermal activation and a finite velocity is expected for non-zero driving forces. When $f \ll f_{\text{dep}}$ the domain wall still moves and the thermally activation motion is called creep regime. When $f > f_{\text{dep}}$ the pinning sites become irrelevant resulting in a flow motion of the domain wall [53].

The magnetic field can act as a driven force to move the domain walls, this is called field driven domain wall motion. When the magnetic field that is applied is high enough, the domain wall is going to move from its equilibrium position. This can be understood according to the LLG equation, when a magnetic field is applied a torque acts on the magnetization and rotates the magnetization ($-\gamma \left(\mathbf{m} \times \mathbf{H}_{\text{ext}} \right)$), this

generates an imbalance in the magnetic moments so that a demagnetizing field is generated. This demagnetizing field generates then an aditional torque $(-\gamma\,(\mathbf{m} \times \mathbf{H}_{\mathrm{d}}))$ which is responsible to drive the domain wall forward. Without pinning sites in the material small magnetic fields would always move the domain wall. A model for field driven domain walls was introduced by Schryer et al. [54], they found that the velocity of the domain wall v_{wall} is proportional to the gyromagnetic ratio γ, the domain wall width x_{wall}, the damping constant α and the applied field H, following:

$$v_{\mathrm{wall}} = (\gamma x_{\mathrm{wall}}/\alpha) \cdot H \tag{2.30}$$

In figure 2.6b the description of the model is summarized. As the magnetic field increases the domain wall starts to deform and when it reaches a critical field H_{w}, the walker breakdown is reached, and at this point the domain wall spin structure starts to transform. After the walker breakdown the velocitiy of the domain wall decreases and at higher fields the domain wall is in a regime that is called linear precessional regime.
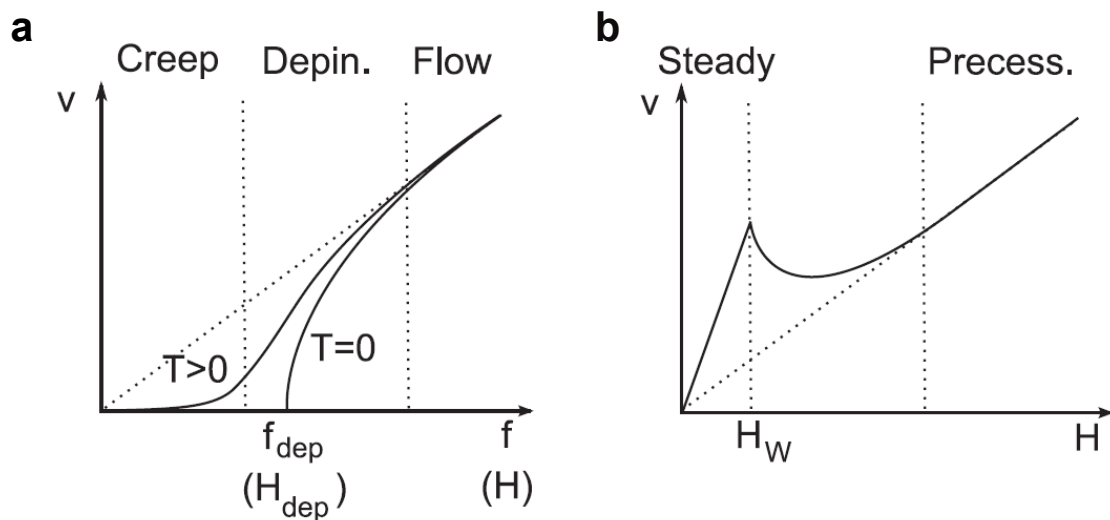
Figure 2.6. – **a**, variation of the velocity of a domain wall depending on the driving force, at zero and infinite temperatures. **b**, domain wall motion in a ferromagnet without pinning. Figure taken from [53].

In similar manner as an applied magnetic field moves domain walls, electrical currents through a mechanism called spin transfer torque (STT) can also move domain walls. The movement of domain walls by means of spin transfer torque is called current induced domain wall motion. Also, in this case the LLG equation describes the evolution

21

of the magnetization, but two extra terms need to be included, the adiabatic STT and the non-adiabatic STT.

The adiabatic STT term is: $-\left(u \cdot \nabla\right) m$, where u is the drift velocity. This term describes the transfer of angular momentum from the spins of the conducting electrons to the magnetization. The conducting electrons change their spin when they cross the domain wall, due to the conservation of the total angular momentum, the magnetic moments of the domain wall change. This results in a movement of the domain wall in the direction of the conducting electrons.

The non-adiabatic STT term is: $-\beta m \times \left[-\left(u \cdot \nabla\right) m\right]$, where β is the non-adiabacity parameter. This term alters the dynamics of the domain wall and in particular the critical current density to move the domain wall and its terminal velocity. The non-adiabatic STT acts on a domain wall similar as the torque that is generated by applying a magnetic field. Below a certain current the domain wall does not move, this mainly due to the balance of the internal torques, after a certain threshold current there is an imbalance in the internal torques and the domain wall starts to move.

2.3. Skyrmions and the Dzyaloshinskii Moriya Interaction

Magnetic skyrmions are chiral spin structures with a whirling configuration [55]. Representations of two typical skyrmions are shown in figure 2.7a and figure 2.7b, the Néel type and the Bloch type skyrmion. Inside the skyrmions the spins rotate with a fixed chirality from one edge of the magnetic material that it is magnetized up to the center of the skyrmion that is magnetized downwards, and then the spins further rotate from the center to the up direction at the other edge [18]. The name "skyrmion" originates from Tony Skyrme who in 1962 developed a nonlinear field theory for interacting pions and found topological stable field configurations behaving as particles [56]. One particular property of skyrmions is their non-trivial topology, which gives a topological protection of the spin configuration, so that the spin configuration can be not twisted into another magnetic configuration. Skyrmions can be classified by their topological winding number, which is a measure of the winding of the normalized magnetization.

Skyrmions can be stabilized due to the competition of the exchange and the magneto-static energy, and the bulk or interfacial Dzyaloshinskii-Moriya interaction (DMI) [57].

The bulk DMI arises because of the break of the crystal inversion symmetry and the presence of high spin orbit coupling atoms in ferromagnetic alloys, as is shown in figure 2.7c. This appears in B20 materials such as MnSi. The origin of the interfacial DMI lies in the interfaces of magnetic multilayers, where the ferromagnetic layers are coupled to other layers that consist of materials that have large spin orbit coupling, as is shown in figure 2.7d. Usually in bulk materials it has been found that Bloch skyrmions are stabilized, whereas Néel skyrmions tend to stabilize in multilayers. The Dzyaloshinskii-Moriya vector $D_{1,2}$ depicted in figure 2.7d, in blue, is perpendicular to the S_1 and S_2 vectors connecting two neighboring spins within the interface plane. When the sign of $D_{1,2} > 0$ the interfacial DMI prefers anticlockwise magnetization rotations for S_1 to S_2, for $D_{1,2} < 0$ clockwise magnetization rotations. Due to this fixed chirality the motion of the skyrmions is chirality-dependent, so that the skyrmions can be driven by spin torques [26]. Skyrmions in multilayers at room temperature with perpendicular magnetization and uniaxial anisotropy are going to be discussed briefly next.
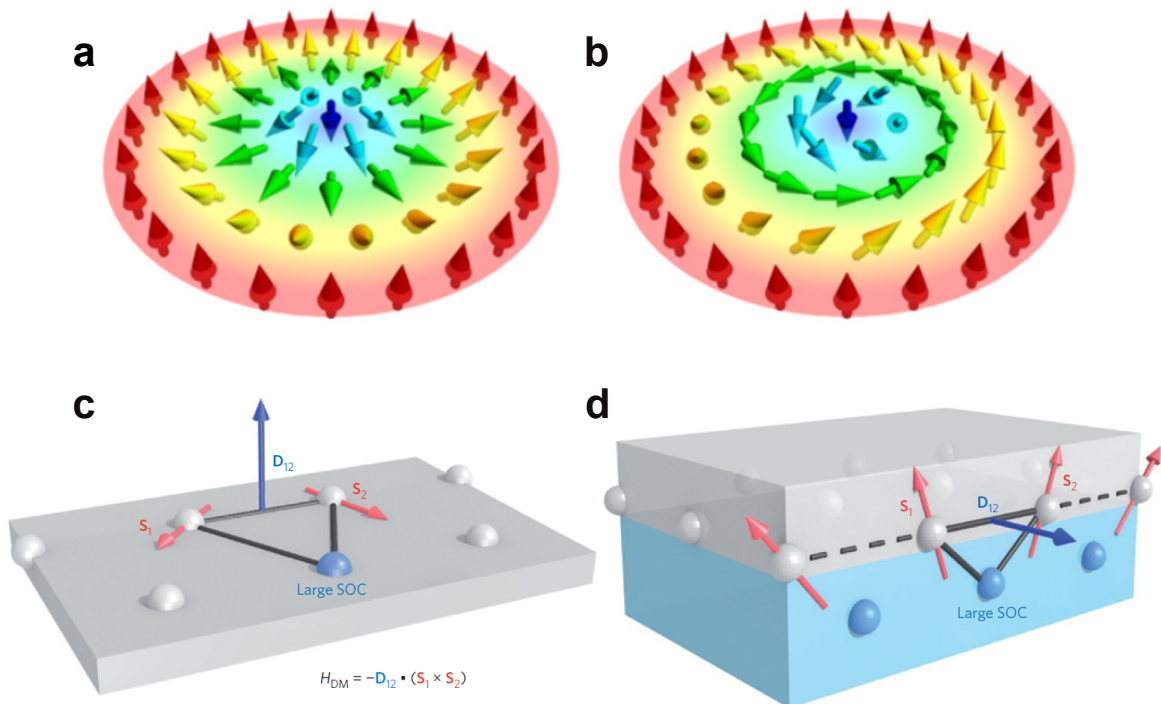
Figure 2.7. – Skyrmions and the Dzyaloshinskii-Moriya interaction (DMI). **a**, sketch of a Néel skyrmion. **b**, sketch of a Bloch skyrmion. Figures were taken from [21]. **c**, representation of the DMI in a bulk crystal. **d**, DMI in an interface between a material with large spin orbit coupling and a ferromagnet. Figures were taken from [55].

The various energies mentioned in section 2.1.2, exchange, anisotropy, demagnetization, Zeeman and asymmetric exchange energies can all be present in multilayer systems and all can contribute to the stabilization of the skyrmions. There are different models that predict a stable skyrmion phase depending on different material parameters (such as the saturation magnetization of the film, the exchange constant and the DMI), temperatures and magnetic fields [58–61]. Also, the models allow to calculate the skyrmion radius in the presence of an applied magnetic field, which is a key parameter for technological applications. In this thesis the skyrmions where stabilized in multilayers that consist of thin magnetic layers that are alternated asymmetrically between two heavy metals, this generates a structural inversion symmetry and thus provides an interfacial DMI. One example of such multilayer is a stack that consist of alternating Pt/Co/Ir layers [23]. In such a multilayer stack a large DMI can be induced at the magnetic layers (compared to single layers as [24]), so that the skyrmion structure is replicated in each magnetic layer thus increasing the total volume of the skyrmions. This allows the observation of small skyrmions at room temperature, due to the high thermal stability of the skyrmions in such multilayers. Also, depending on the material which is chosen for the two heavy metals in the stack the effective DMI can be increased if the materials induce interfacial chiral interaction of opposite symmetries and a parallel Dzyaloshinskii-Moriya vector.

There are different mechanisms to generate or nucleate skyrmions in magnetic systems, by magnetic fields, by thermal excitations, by spin torques, and by electric fields [21]. One of the most promising mechanism is the nucleation by means of spin torques (electrical current pulses) since this allows to controllably nucleate single skyrmions at specific positions [26,62] and not randomly. Skyrmion nucleation in multilayers by means of electrical current pulses is shown experimentally in chapter 5 section 5.3 of this thesis and was proven to be a reliable mechanism to nucleate single skyrmions.

2.4. Transport phenomena: from magneto-resistive effects to magneto-thermoelectric effects

In the last decade the field of spin caloritronics has given important results to the understanding of the coupling of heat and the charge currents. It can be said that this field of study can be traced back almost two centuries ago to Thomas Seebeck and William Thomson, but new interest in this field, arose from the experimental results

shown by Gravier et al. [63] where the magneto-thermoelectrical power in multilayers was experimentally determined. The spin caloritronic phenomena can be roughly classified into: independent electron, collective and relativistic effects according to [4]. The independent electron effects consist of the thermoelectric generalization of collinear magnetoelectronics and effects such as giant magnetoresistance and tunnel magnetoresistance. The collective effects are generated by the collective dynamics of the magnetic order parameter that couple to single particle spins via spin-transfer torque and spin pumping. The relativistic effects are thermoelectric generalizations of relativistic corrections such as anisotropic magnetoresistance, anomalous Hall effects and spin Hall effects. In this thesis the interest lies in the independent electron phenomena of spin caloritronics where thermoelectric generalization of spintronic effects such as the magneto resistive effects lead to the spin dependent Seebeck effect.

Spin dependent Seebeck effects can be described according to [64,65] for ferromagnetic/non-magnetic nanostructures. The charge current density $\mathbf{J}$ and the heat current density $\mathbf{Q}$ can be related to the voltage $\mathbf{V}$ and temperature $\mathbf{T}$ in the following way:

$$\begin{pmatrix} \mathbf{J} \\ \mathbf{Q} \end{pmatrix} = - \begin{pmatrix} \sigma & \sigma S \\ \sigma \Pi & \kappa \end{pmatrix} \begin{pmatrix} \nabla \mathbf{V} \\ \nabla \mathbf{T} \end{pmatrix} \tag{2.31}$$

where σ is the electrical conductivity, S the Seebeck coefficient, Π is the Peltier coefficient defined by $\Pi = S T_0$ where T_0 is the nanostructure temperature, and κ is the thermal conductivity. The equation 2.31 can also be expressed in two equations that are found in textbooks as [66]:

$$\mathbf{J} = -\sigma \nabla \mathbf{V} - \sigma S \nabla \mathbf{T} \tag{2.32}$$

$$\mathbf{Q} = -\sigma \Pi \nabla \mathbf{V} - \kappa \nabla \mathbf{T} \tag{2.33}$$

these two equations represent the kinetic equations. From the equations can be deduced that the charge current density is constituted from an ohmic part that arises due to a potential difference or electric field using the identity $\mathbf{E} = -\nabla \mathbf{V}$ and a thermoelectric part that arises due to a temperature gradient. In similar manner the heat current density is constituted, one part is proportional to the Peltier effect due to the electrical current and the other part is proportional to the thermal conductivity. With equation

25

2.32 the electric and thermoelectric transport equations that are relevant for this thesis can be obtained and are going to be introduced next.

2.4.1. Anisotropic magnetoresistance and Hall effect

The first known experimental observation of the AMR effect can be traced to William Thomson, Lord Kelvin, in the year 1857 [67], who observed that the resistance of an iron conductor increased by 0.2% when the magnetic field was applied parallel to the current direction in the iron and the resistance decreased by 0.4% when the magnetic field was applied perpendicular to the current direction [41]. Usually in ferromagnetic materials the resistivity is lower, when the magnetization is oriented perpendicular to the applied current than when it is parallel. The origin of the AMR effect lies in the spin-orbit coupling as first suggested by Smit in 1951 [68]. It is based on the two current model suggested by Mott [69] (the name of the model was introduced in 1968 in [70]).

The two current model explains not only the electrical conductivity in metals but also transport properties in ferromagnets and it is based on the band theory of the electronic structure of solids. This model that describes the normal magnetoresistance is going to be introduced next [41]. A representation of the model is illustrated in figure 2.8. In transition metals such as nickel and iron, the major part of the current is carried by light electrons of the s band (the same is for metals) and the electrical resistance is dominated by scattering processes in which electrons are scattered from the s to the d band.

Since the scattering rate depends on the density of states the more d states are available, the stronger is the scattering. The scattering is spin selective so that the s electrons can only jump to d states that have the same spin. Note, that in the model spin-flips are assumed to be negligible. So that only spin-conserving excitation area allowed. The importance of the model is that it explains that the two spin states carry the electrical current in parallel without much mutual interaction as two independent spin channels, and that the total conductivity is given by the sum of the two channels. The resistivity depends on the scattering impurities in the material and on the spin-dependent scattering (from the s to the d band) for the two separated channels which is proportional to the empty d states.

For the particular case of figure 2.8 the resistivity for spin up electrons is larger in

comparison to the spin down electrons, this is because the density of empty states in the d band is larger for the spin up channel (minority spin) than for the spin down channel (majority spin), therefore the scattering probability increases.
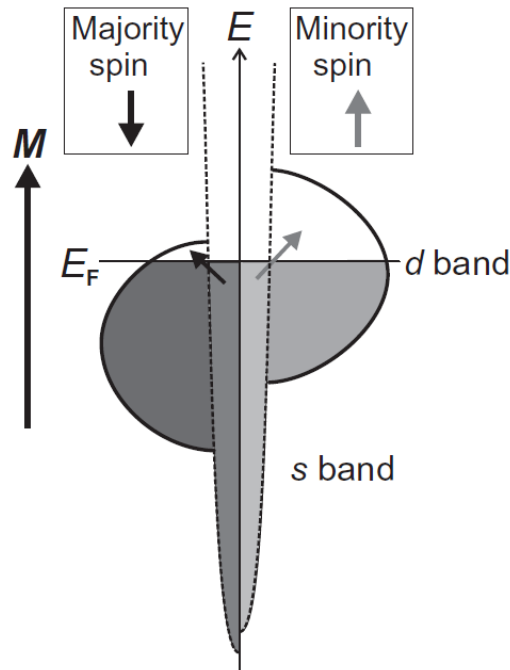
Figure 2.8. – The two current model. The ferromagnetic material is alignet along the up direction, same as its magnetization. The d states are indicated by a semicircle and the s states by parabolas. Spin direction in light gray decscribes the spun up orientation and in dark gray the spin down orientation. Figure adapted from [41].

To explain the physical origin of the AMR effect spin-orbit interaction was introduced in the two current model. Due to the spin-orbit interaction spin-flip scattering is allowed, i.e. spin up electrons can scatter in-to the empty d down band which results in an increase in resistance. Also as a consequence, transitions appear due to the generation of holes from the transitions of the d up band to the s down band providing further channels for the $s-d$ scattering [40]. Therefore, the $s-d$ scattering probability depends on the angle between the magnetic moments (or magnetization) with respect to the electrical current direction leading to the given angular dependence.

When a perpendicular magnetic field is applied to a current carrying conductor it gives rise to a transverse voltage. This effect is known as the ordinary Hall effect and it is proportional to the applied magnetic field and current. It results from the Lorentz force

acting on the conduction electrons [42]. Figure 2.9a shows a representation of the Hall effect. The Hall effect was discovered in 1879 by Edwin Hall. A couple years later by performing similar experiments in ferromagnetic materials he observed that the Hall effect was much larger in ferromagnetic materials than in nonmagnetic metals. The latter effect is called anomalous Hall effect (AHE) and in the same configuration as the Hall effect the transversal resistance not depends strongly on the applied magnetic field but rather on the magnetization of the ferromagnet, as is shown in figure 2.9b. The AHE has is origins not in the Lorentz force but rather on three different mechanism: intrinsic deflection, side jump and skew scattering [71].
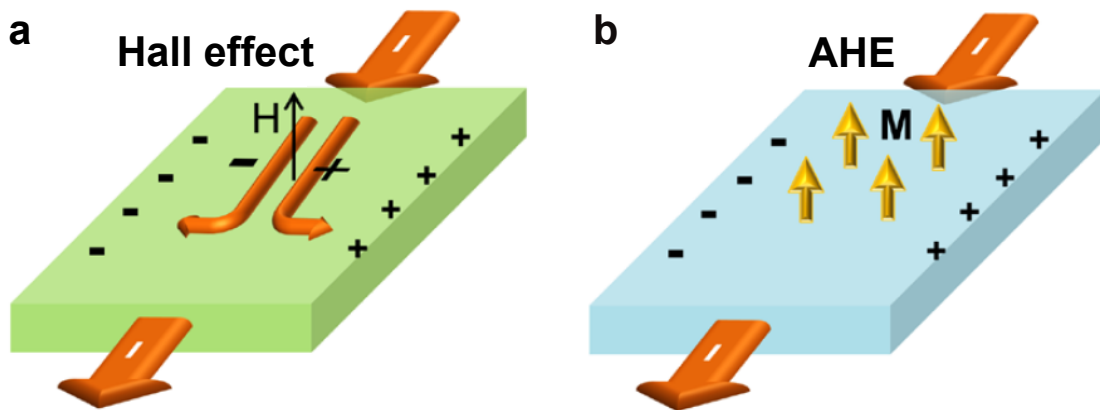
Figure 2.9. – **a**, sketch of the Hall effect. **b**, sketch of the AHE. **H** denotes the applied magnetic field and **M** denotes the internal magnetization. Figures adapted from [72].

In the absence of a temperature gradient and using equation 2.32, the electric transport equations that describe the anisotropic magneto resistance and the Hall effects can be derived. Consider a ferromagnetic conductor material as is depicted in figure 2.9b, which is magnetized along the z-axis and the electrodes connected to the material are perpendicular to its magnetization in the x-y plane. Ohms law for this particular case in its tensorial form can be written in the form [73]:

$$
\mathbf{J} = \begin{pmatrix} \sigma_\perp & \sigma_H & 0 \\ -\sigma_H & \sigma_\perp & 0 \\ 0 & 0 & \sigma_\parallel \end{pmatrix} \mathbf{E} \tag{2.34}
$$

where the off-diagonal coefficients σ_H are defined by the microscopic mechanisms that couple the spin-dependent electric carriers and the magnetization. The main mech-

anism that are involved are named intrinsic deflection, side jump and skew scattering [71].

Due to the magnetization anisotropy the terms in the electrical conductivity tensor have the following properties $\sigma_{xx} = \sigma_{yy} = \sigma_\perp$ but $\sigma_{zz} = \sigma_\parallel \neq \sigma_\perp$. Also due to the Onsager reciprocity relation [74, 75] the cross coefficients are antisymmetric $\sigma_{xy} = \sigma_{yx} = \sigma_{\mathrm{H}}$. Ohms law expressed in equation 2.34 can be inverted and be written in terms of a resistivity tensor [76]:

$$\mathbf{E} = \begin{pmatrix} \rho_\perp & -\rho_{\mathrm{H}} & 0 \\ \rho_{\mathrm{H}} & \rho_\perp & 0 \\ 0 & 0 & \rho_\parallel \end{pmatrix} \mathbf{J} \tag{2.35}$$

where $\rho_\perp = \sigma_\perp / (\sigma_\perp^2 + \sigma_{\mathrm{H}}^2)$ and $\rho_\parallel = 1/\sigma_\parallel$ represent the resistivity perpendicular and parallel to the magnetization and $\rho_{\mathrm{H}} = \sigma_{\mathrm{H}}^2 / (\sigma_\perp^2 + \sigma_{\mathrm{H}}^2)$ is the Hall resistivity.

The Hall effect can be obtained directly from equation 2.35 being the electric field $E_y = \rho_{\mathrm{H}} J_x$, this is when the current is flowing along the x-axis and the magnetization is along the z-axis. Depending on the orientation of the magnetization in the material the terms in the resistivity tensor in equation 2.35 change. A more general equation for any direction of the magnetization can be obtained and was introduced in [2]:

$$\mathbf{E} = \rho_\perp \mathbf{J} + \left(\rho_\parallel - \rho_\perp \right) (\mathbf{J} \cdot \widehat{\mathrm{m}}) \, \widehat{\mathrm{m}} + \rho_{\mathrm{H}} \widehat{\mathrm{m}} \times \mathbf{J} \tag{2.36}$$

where $\widehat{\mathrm{m}}$ is a unit vector pointing in the direction of the magnetization. In this equation three different terms can be identified. The first term defines the normal resistance, the second term the AMR effect which includes the planar Hall effect (PHE) or transversal AMR effect contribution and the last term is defined as the AHE. From equation 2.36 the relevant equation of the AMR effect for this thesis can be obtained, assuming that the magnetization and the electrodes are oriented according to figure 2.10a, magnetization in the x-y plane and the electrical current and the electric field are in the y-axis, the following equation is obtained:

$$E_y = J_y \left[\rho_\perp - \rho_\perp \sin^2 a + \rho_\parallel \sin^2 a \right] \tag{2.37}$$

In equation 2.37 the magnetization and the current density were defined in cartesian coordinates $\widehat{\mathrm{m}} = \sin(b)\cos(a)\,\widehat{\mathrm{x}} + \sin(b)\sin(a)\,\widehat{\mathrm{y}} + \cos(b)\,\widehat{\mathrm{z}}$ and $\mathbf{J} = J_x \widehat{\mathrm{x}} + J_y \widehat{\mathrm{y}} + J_z \widehat{\mathrm{z}}$,

where the angles a and b are depicted in figure 2.10b. The angle a is the azimuth angle and b the polar angle. Equation 2.37 can be rewritten and put in terms of resistivity, which is a common denotation that is found in the literature:

$$\rho = \rho_\parallel + \left(\rho_\perp - \rho_\parallel\right) \cos^2 a \tag{2.38}$$

this equation describes the change in the resistivity in a ferromagnetic material when its magnetization is oriented at a certain angle a with respect to the current that is applied to it (for this example the current is in the y-axis), which is the essence of the AMR effect that was described above.
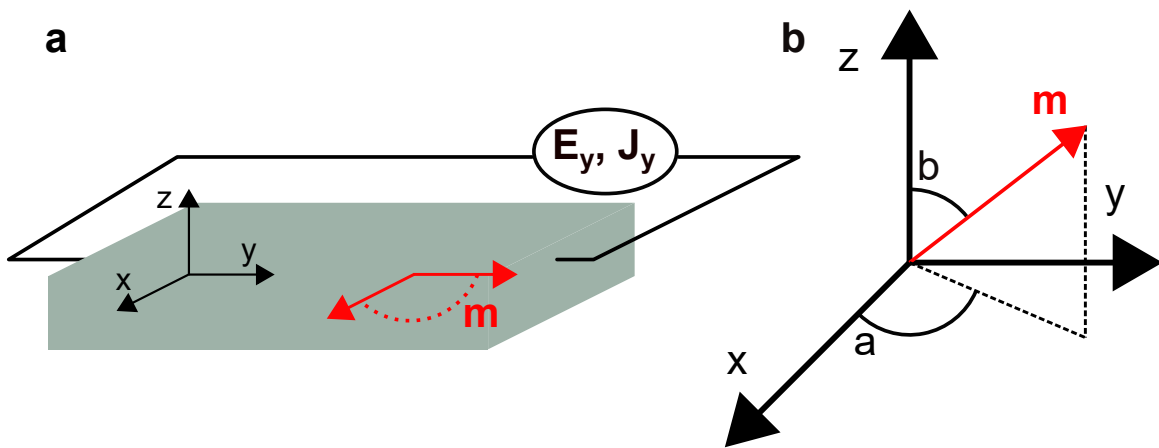
Figure 2.10. – **a**, schematic view of the measurement configuration of an AMR device. The electrical current and the electric field are along the y-axis and the magnetization can rotate in the x-y plane. **b**, reference coordinate system for the magnetization m. The angle a depicts the azimuth angle and the angle b the polar angle.

2.4.2. Anisotropic magneto-Seebeck effect and anomalous Nernst effect

The discovery of the thermopower was attributed to Thomas Seebeck, who discovered in the year 1826 that a compass needle would get deflected when placed nearby a junction between two different metals were one of the junctions was heated and the other one cooled [77]. At the beginning it was though that this effect would have a magnetic origin but later it was shown that the electric current generated by the temperature difference, generates an Oersted field that deflected the needle. In general, a thermoelectric effect

describes the conversion of a temperature difference into electrical voltage and vice versa. When a conducting material is under the influence of a temperature difference (a temperature gradient) along two points in the material the electrons in the hotter area are in a higher energetic level as the electrons in the colder area, this causes the electrons to move from the hotter side to the colder side, see figure 2.11 for an illustration. Therefore, there is an accumulation of electrons in the colder area and in the hotter area holes are formed, generating an electric field. The electric field produced due to this temperature gradient can be expressed as follows:

$$E = -S\nabla T \tag{2.39}$$

where the S is a proportionality coefficient called the Seebeck coefficient.

To obtain experimentally the absolute value of the Seebeck coefficient is not a trivial measurement; instead, a thermocouple measurement is usually adopted and therefore always two or more materials are involved giving rise to a parasitic Seebeck coefficient from the contact material [78–80].
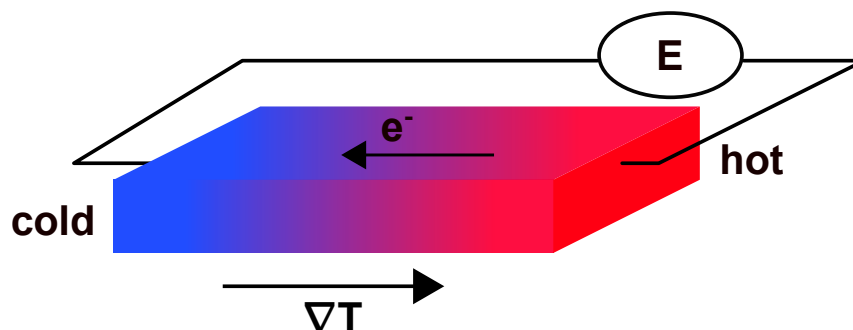
Figure 2.11. – Illustration of the Seebeck effect. E represents the generated electric field produced by a thermal gradient ∇T. The electrons move from the hotter area to the colder area.

Already, in 1851 William Thomson started to study thermoelectric effects in a diamagnetic material such as bismuth [81]. Numerous experimental works have been performed in studying magneto-thermoelectric effects, one experiment relevant for this thesis is the study of the magneto-thermopower in ferromagnetic materials [82,83], this effect was also called magneto-thermoelectrical power [63].

In this thesis the magneto-thermopower effect or magneto-thermoelectrical power effect is going to be called anisotropic magneto-Seebeck (AMS) effect, due to its similitude

with the AMR effect [5]. The AMS effect can be directly related to the AMR effect by using the Mott formula [69]:

$$S = \frac{\pi^2 k_{\mathrm{B}}^2 T}{3|e|} \left[\frac{1}{\rho_{(\epsilon)}} \frac{\partial \rho_{(\epsilon)}}{\partial \epsilon} \right]_{\epsilon = \epsilon_{\mathrm{F}}} \tag{2.40}$$

where k_{B} is the Boltzmann constant, e the electron charge, T the temperature and ρ_ϵ the resistivity when evaluated at the fermi energy ϵ_{F}. This formula describes the Seebeck coefficient in the electron free model. The equation is based on the assumptions that the electron diffusion is the dominant contributor, the scattering is elastic and that a relaxation time can be defined so that the Wiedermann-Franz law is obeyed.

The first ones to show that the derivative term in equation 2.40 was independent of the magnetic field were Nordheim and Gorter [84], meaning that the Seebeck coefficient should behave in the same manner as the resistivity. It was also shown that the two current model can also be applied in the similar manner as the resistivity using spin dependent Seebeck coefficients as was showed in [83]. All this leads to the conclusion that the theory presented in section 2.4.1 explains the AMS effect in similar manner as the AMR effect.

Similar as the Hall effect, when due to a thermal gradient, electrical carriers are driven, they can move transversally in the presence of an applied magnetic field, generating a transversal electric field. This effect is called Nernst effect and was discovered in 1886 by Nernst and Ettingshausen. Same as the AHE the Nernst effect behaves differently in ferromagnetic materials as in nonmagnetic materials and it depends stronger on the magnetization than the applied magnetic field, this effect is called anomalous Nernst effect (ANE). The Hall effects and Nernst effects not show at first sight a relationship, but one can think that they share the same microscopic origin. Similar as the Seebeck coefficient and the resistivity there is a link between the AHE and the ANE through the Mott relationship [85].

To obtain the magneto-thermoelectric relations, equation 2.32 is going to be used in a similar manner as in section 2.4.1. In an open circuit condition, a charge current can be driven by a temperature gradient generating a thermopower in the form of an electric field. In the case of a ferromagnetic conductor with a magnetization pointing in the z-axis the equation 2.32 can be rewritten including the Seebeck tensor obtaining the following equation:

$$\mathbf{E} = \begin{pmatrix} S_\perp & S_N & 0 \\ -S_N & S_\perp & 0 \\ 0 & 0 & S_\parallel \end{pmatrix} \nabla \mathbf{T} \tag{2.41}$$

where the off-diagonal term S_N is called Nernst coefficient and the terms $S_\perp$ and $S_\parallel$ are the Seebeck coefficients perpendicular and parallel to the magnetization, respectively. Equation 2.41 has the same form as the equation that includes the resistivity tensor (equation 2.35), therefore equation 2.41 can be rewritten in terms of the Seebeck coefficients, Nernst coefficient and the thermal gradient in the following form:

$$\mathbf{E} = S_\perp \nabla \mathbf{T} + \left(S_\parallel - S_\perp \right) \left(\nabla \mathbf{T} \cdot \hat{\mathrm{m}} \right) \hat{\mathrm{m}} - S_N \hat{\mathrm{m}} \times \nabla \mathbf{T} \tag{2.42}$$

this equation represents the thermoelectrical analogue to the resistivity equation 2.36. The first term in the equation is the Seebeck effect, the second term includes the AMS effect and the planar Nernst effect (PNE) and the last term is the ANE.

The AMS effect and the ANE are the main interest of study in this thesis therefore examples of their representative equations are going to be derived parting from equation 2.42. For the magnetization the same coordinate system as figure 2.10b is going to be taken and the thermal gradient is going to be represented by $\nabla \mathbf{T} = \nabla T_x \hat{\mathrm{x}} + \nabla T_y \hat{\mathrm{y}} + \nabla T_z \hat{\mathrm{z}}$. Equation 2.42 can be decomposed in the three spatial coordinates of the electric field as follows:

$$
\begin{aligned}
E_x = S_\perp \nabla T_x + \left(S_\parallel - S_\perp \right) & \left[\nabla T_x \sin^2(b) \cos^2(a) \right. \\
& \left. + \nabla T_y \sin^2(b) \sin(a) \cos(a) + \nabla T_z \sin(b) \cos(b) \cos(a) \right] \\
& - S_N \left[\nabla T_z \sin(b) \sin(a) - \nabla T_y \cos(b) \right]
\end{aligned}
\tag{2.43}
$$

$$
\begin{aligned}
E_y = S_\perp \nabla T_y + \left(S_\parallel - S_\perp \right) & \left[\nabla T_x \sin^2(b) \sin(a) \cos(a) \right. \\
& \left. + \nabla T_y \sin^2(b) \sin^2(a) + \nabla T_z \sin(b) \cos(b) \sin(a) \right] \\
& - S_N \left[\nabla T_x \cos(b) - \nabla T_z \sin(b) \cos(a) \right]
\end{aligned}
\tag{2.44}
$$

$$E_z = S_\perp \nabla T_z + \left(S_\parallel - S_\perp \right) \Bigg[\nabla T_x \sin{(b)} \cos{(b)} \cos{(a)}$$

$$+ \nabla T_y \sin{(b)} \cos{(b)} \sin{(a)} + \nabla T_z \cos^2{(b)} \Bigg] \qquad (2.45)$$

$$- S_{\mathrm{N}} \Bigg[\nabla T_y \sin{(b)} \cos{(a)} - \nabla T_x \sin{(b)} \sin{(a)} \Bigg]$$

these tree equations can be implemented depending on the direction of the material or device with respect to the thermal gradient and the magnetization.

Experimentally this means that depending how a material or device is electrically connected, from which direction the heat source that generates the thermal gradient is coming and the magnetization is oriented, the system can be described with one of these three equations. Also, the effects such as the Seebeck effect, the AMS effect and the ANE depend on the orientation and the magnitudes that were mentioned.
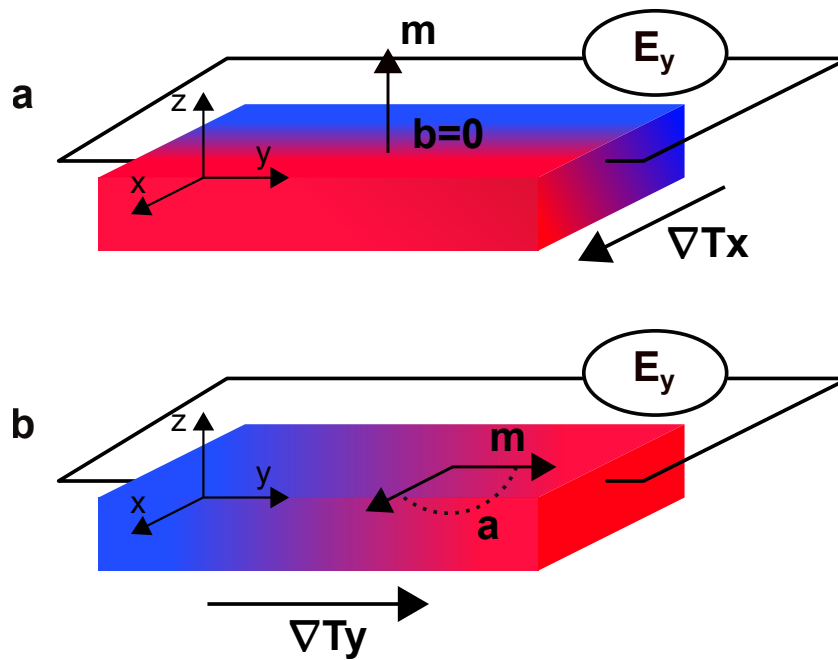
Figure 2.12. – Possible device configurations. **a**, the magnetization is oriented along the z-axis, the electrical connections are along the y-axis and thermal gradient is along the x-axis. **b**, the magnetization is in the x-y plane, the electrical connections and thermal gradient is along the y axis.

As an example, in figure 2.12 two possible device configurations are illustrated. In figure 2.12a the magnetization is oriented out-of-plane in the positive direction (polar angle,

34

$b = 0°$ or z-axis), the electrical contacts are along the y-axis and the thermal gradient is along the x-axis. The equation 2.44 describes the thermoelectrical transport in this case since the electrical contacts are oriented along the y-axis, and so the equation simplifies to:

$$E_{y;out-of-plane} = -S_\text{N}\nabla T_x \tag{2.46}$$

Equation 2.46 describes the ANE for the particular device geometry in figure 2.12a. Notice that the ANE arises only when the magnetization, the thermal gradient and the electric field are perpendicular to each other. This is mainly due to the cross product in the last term in equation 2.42.

In figure 2.12b the magnetization is oriented in-plane (polar angle, $b = 90°$ or x-y plane), the electrical contacts and the thermal gradient are in the y-axis. In this case the equation 2.44 simplifies to:

$$E_y = S_\perp \nabla T_y + \left(S_\parallel - S_\perp\right)\nabla T_y \sin^2{(a)} \tag{2.47}$$

this equation is similar to the AMR effect equation 2.38 and describes the AMS effect in the particular device geometry of figure 2.12b.

The equations presented in this section are going to be used to introduce a new procedure for the analysis of thermoelectrical measurement data in chapter 4 and are the fundamental basis to understand the measured signal in the experiments performed in this work.

3. Experimental techniques

A variety of methods is available to prepare nanowires with different shape, size and aspect ratios for technological applications and study of physical phenomena. The reduction of device dimensions requires spatially resolved analysis techniques with a high sensitivity. In particular, the interest in the fields of spintronic and nanomagnetism leads to the need to find local techniques [86] that allow for a detailed description of the magnetic states in each part of the device under study.

This chapter gives an overview of the different experimental techniques used along this investigation. First, the fabrication methods of the micro/nanodevices are presented, then the method used to measure the thermoelectric voltage on the devices fabricated is described.

The micro/nanowires are made of magnetic materials such as permalloy (NiFe). To study the magnetization behavior two domain detection and observation techniques were used. Finally, the different measurement setups used in this investigation are shown.

3.1. Fabrication of the micro/nanodevices

The devices fabricated in this investigation consisted of a micro/nanowire of magnetic material several micrometers long, which was centered between one or two metallic stripes that were used as heaters (see sketch in figure 3.3 for an example). Scanning electron microscope images of the real devices can be found in the respective chapters. To simplify the nomenclature, wire refers to the magnetic microwire or nanowire in the center of the device and heater refers to the metallic stripe that is next to the wire. The following fabrication steps that are explained refer to the devices in which the wire was made of permalloy or the of the multilayer structure Pt/Co/Ru.

The fabrication steps can be divided in two main steps, the fabrication of the wires (figure 3.1) and the fabrication of the heater and contacts (figure 3.2). Standard lithography techniques such as e-beam patterning, lift-off, sputtering and argon ion plasma etching were used for the fabrication of the devices. Details of all parameters of the clean room processes used within this thesis are listed in Annex A.

3.1.1. Fabrication of the wires

Usually the substrates of the magnetic films used in this thesis for the wire fabrication were much smaller than a 3-inch wafer used as standard substrate for processing in the PTB clean room center. Therefore, the magnetic film substrate was glued with TEM wax on top of a Si wafer. Before starting the lithography process, the magnetic films were cleaned with standard cleaning methods (figure 3.1a). In the following the term "wafer" will be used for the whole combination of the magnetic film with its substrate glued on the Si wafer.

To fabricate an Al mask for the wire fabrication by etching, the wafer was coated with a commercial two-layer e-beam positive resist (figure 3.1b). The thickness of the two resist layers combined was 138 nm. A negative mask was written using PTB's e-beam lithography system (EBPG 5200 from Raith Nanofabrication) followed by standard developing methods (figure 3.1c as a reference).

Using a standard thermal evaporator, 50 nm of Al were evaporated on the wafer (figure 3.1d). The desired Al mask on top of the magnetic film, is obtained by a lift-off process (figure 3.1e).

At this point the envisaged structural characteristics for the wires are defined by the Al layer on top on the magnetic film, this type of mask is usually called a "hard mask". The unwanted magnetic material was then removed by using conventional dry argon etching technique. A mass spectrometer inside the sputtering machine was used to control the etching process. This allowed to measure, as a function of time, the intensity of the ion signal corresponding to the atomic mass of the elements etched away. The etching process was stopped when the ion signal of the magnetic material vanished. As a final step to control the etching process, the resistance of the unmasked substrate areas was measured. Since the magnetic films in this thesis were grown on a Si/SiO_2 substrate the unmasked substrate areas should become highly resistive after the magnetic film is etched away if the etching process of the magnetic film was successful.

At this step the wires with the desired pattern are defined, but the Al layer that was used for the hard mask is still on top of the magnetic material (figure 3.1f). This Al layer is removed wet chemically using a specific developer, which contains sodium hydroxide (NaOH). The NaOH based developer transforms the Al into sodium aluminate (NaAlO$_2$) and at the same time it releases hydrogen to the surrounding atmosphere. This dissolves the Al in the developer leaving the magnetic material intact. This specific Al removing process was performed on many other films and wafers made of different materials for other purposes not related to this thesis and none of the processes showed a damage to the wires. After this step the magnetic wire with the desired pattern are finished, as shown in figure 3.1g.
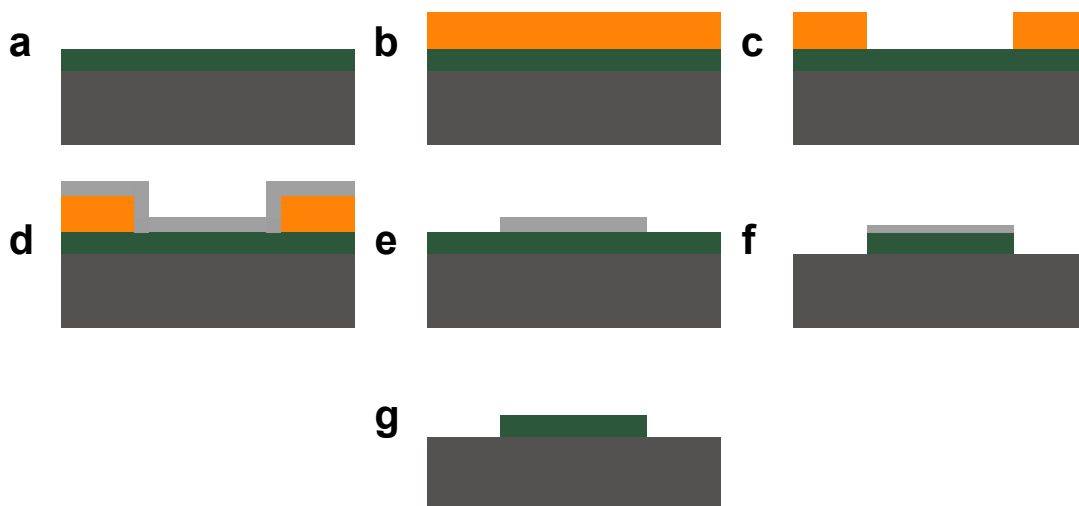
Figure 3.1. – Fabrication steps to obtain single wires in a substrate. **a**, the magnetic film in green which was grown on a Si/SiO_2 substrate glued to a Si wafer. **b**, after coating the wafer was covered with two layers of resist. The resist is colored in orange. **c**, the wafer after the patterning of the desired structures and developing process. **d**, Al was evaporated on the wafer. **e**, after the lift-off process the desired pattern of the wires is on top of the magnetic film creating a hard mask. **f**, the unwanted material was removed by means of argon etching. **g**, the Al layer was removed, and the magnetic wires are finished.

3.1.2. Fabrication of the heater and contacts

As mentioned above, a metallic stripe line that serves as a heater was patterned next to the wire. Also, the wire needs to be electrically contacted. The heater line fabrication and the fabrication of the electrical contacts for the wire were performed in the same wire fabrication process step. To this end, the film with the patterned magnetic wires again needed to be glued to a Si wafer (figure 3.2a). The wafer was then coated with two commercial positive resists, covering the top and the surroundings of the wire as shown in figure 3.2b. The two resist layers had a thickness of approximately 534 nm. The patterning of the positive mask for the heater and the contact deposition was performed in the same step by standard e-beam lithography and developing (figure 3.2c).
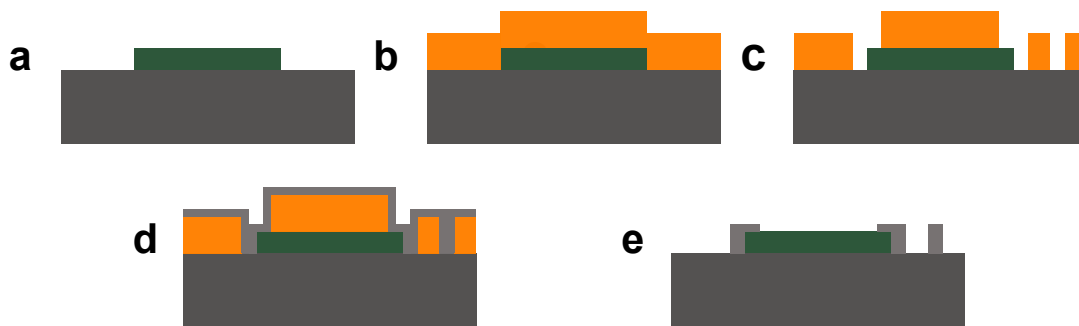
Figure 3.2. – Fabrication steps to pattern the heater and contacts in the devices. **a**, the magnetic wires after the fabrication process. Green represents the magnetic material and dark grey the substrate in which the magnetic material was grown. **b**, after coating the wafer with the two layers of resist. The resist is colored in orange. **c**, the wafer after the patterning of the desired structures and developing process. **d**, Ta/Pt was evaporated on the wafer. **e**, after the lift-off process the desired pattern of the heater and electrical contacts is finished.

The wafer was coated by sputter deposition with Ta and Pt, with thicknesses of 5 nm and 95 nm respectively, material chosen for the heater and contacts. Here, the Ta serves as an adhesion material for the Pt (figure 3.2d). The unwanted resist and material were removed by a lift-off process and thereby the devices were ready to be used, see figure 3.2e.

3.2. Thermoelectric voltage measurements

The main focus in this work was to measure the thermoelectric voltage response to changes in the magnetization in the magnetic wires. All devices studied consisted of a central magnetic wire and one or two, heaters parallel to the magnetic wire separated by a certain distance (usually in the range of 1 µm to 2 µm). In the devices, depending on the direction of the magnetization, the anomalous Nernst effect (ANE) or the anisotropic magneto-Seebeck effect (AMS) could be measured. In the devices these effects are induced by means of the Joule heating of the heater, or sometimes called resistive heating, that creates a temperature gradient along the magnetic wire. The origin of the thermoelectric voltage due to this temperature difference was explained in detail in chapter 2 section 2.4.2. Two different thermoelectric voltage measuring techniques can be employed: nanovolt DC measurements and AC lock-in. A schematic view of one device where the thermoelectric voltage measuring principles are demonstrated can be found in figure 3.3.

3.2.1. Nanovolt measurements

In this technique a DC current was applied to the heater. After the current is applied to the heater it takes some time until the device is in thermal equilibrium. This was observed by measuring the thermoelectric voltage for a known magnetization direction. After 10 min the thermoelectric voltage does not rise anymore for a fixed current to the heater indicating stable conditions. The thermoelectric voltage generated by the temperature difference was measured in the wire with a nanovoltmeter (Keithley 2182A). The connections were chosen such that the plus pole was connected to the upper contact and the negative pole to the bottom contact (figure 3.3). In this way, when the magnetization points completely out-of-plane in the positive direction and the temperature difference is along the x-axis, the thermoelectric voltage measured is positive according to the ANE.

3.2.2. Lock-In technique

In this case the current applied to the heater is an AC current. Different frequencies in the range from 10 Hz to 2000 Hz were put on test for these measurements and depending on the device the proper frequency was chosen. It is known from Joule's first
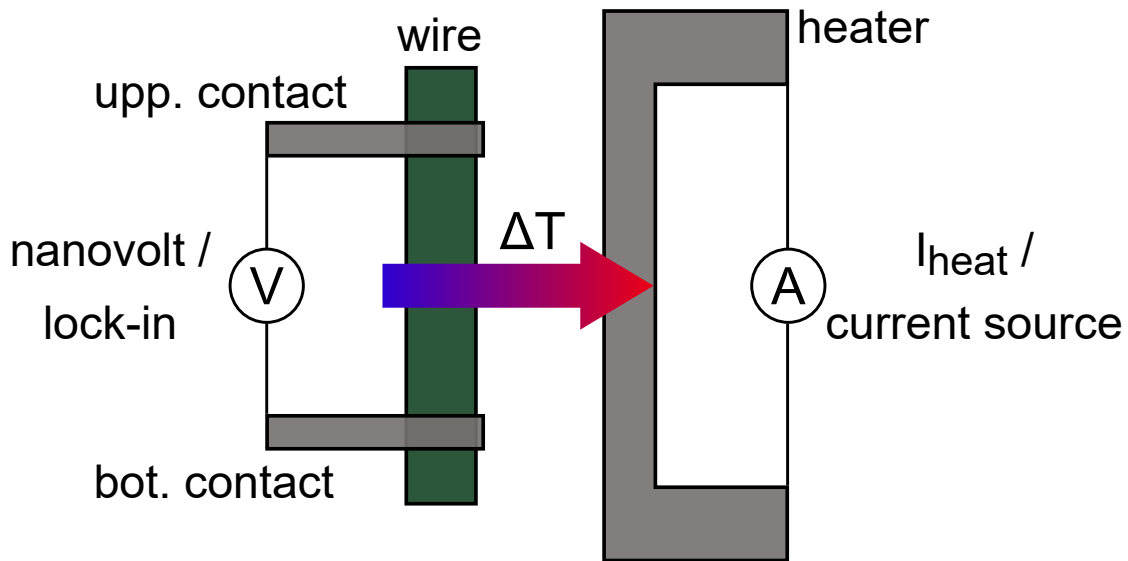
Figure 3.3. – Schematic view of the thermoelectric voltage measuring techniques. For the DC measurements a nanovoltmeter and current source are used. For the AC measurements a combination of a lock-in amplifier with a current source are used.

law that the heating power generated from a conductor is proportional to the resistance of the conductor and the squared current ($P_{heat} = I_{AC}^2 R_{heater}$). If the current $I_{AC}(t) = \sqrt{2}I_{heat}\cos\omega t$, with the angular frequency $\omega = 2\pi f$ is applied to the conductor, the heating power becomes:

$$P_{heat}(t) = I_{heat}^2 R_{heater}(1 + \cos 2\omega t) \tag{3.1}$$

In steady state, the temperature is proportional to the power and changes with the same frequency as the power in the form:

$$T_{heater}(t) = T_0 + \Delta T_{heater}(1 + \cos(2\omega t + \phi)) \tag{3.2}$$

This means that also the thermoelectric voltage signal is alternating, but with the double frequency of the AC current applied to the heater. To detect this thermoelectric voltage a lock-in amplifier (SR 830) was used. The lock-in gives the possibility to filter out all other signals that could influence the measurements and just "lock" a specific

frequency. Since for these measurements the thermoelectric voltage has double the frequency of the input signal to the heater the lock-in measurements were performed on the second harmonic. For the AC case, the connections for the thermoelectric voltage detection were chosen in such a way that when the magnetization points completely out-of-plane in the positive direction and the temperature difference created by the heater is in the x-axis the voltage should be positive.

3.3. Domain detection and observation techniques

In the next section the methods employed in this thesis to visualize and measure the magnetic domain structure are explained. For each method the principle and the basic experimental procedure are presented.

3.3.1. Magneto optical Kerr effect

Domain observation by optical means have a long history. Depending on the characteristics of the magnetic sample there are two effects allowing to visualize the surface magnetization or the bulk magnetization of the magnetic sample: the Kerr effect and the Faraday effect, respectively. Both effects are based on rotations in the polarization plane of the reflected or transmitted light and this rotation depends on the orientation of the magnetization either at the surface of the magnetic material or in the bulk. For magnetic materials that are transparent the bulk magnetization can be visualized only in transmission using the Faraday effect [87]. Most magnetic materials are non-transparent which means that the reflected light experiences a rotation in the polarization plane by the Kerr effect [88]. The text book of Hubert and Schäfer [45] described a detailed discussion of these magneto-optical methods and techniques. A review of applications using these both methods can be found in [89]. In this thesis the Kerr effect or also called the magneto-optical Kerr effect (MOKE) was used to visualize domain walls in nanowires in some of the experiments performed.

Depending on the orientation of the relative magnetization in magnetic materials to the plane of incidence and the orientation of the polarization of light, three fundamentally different types of MOKE can be distinguished: the longitudinal MOKE, the polar MOKE, and the transverse MOKE. In figure 3.4 the different types of MOKE are shown. Experimentally, the MOKE sensitivity axis is defined by the plane of incidence
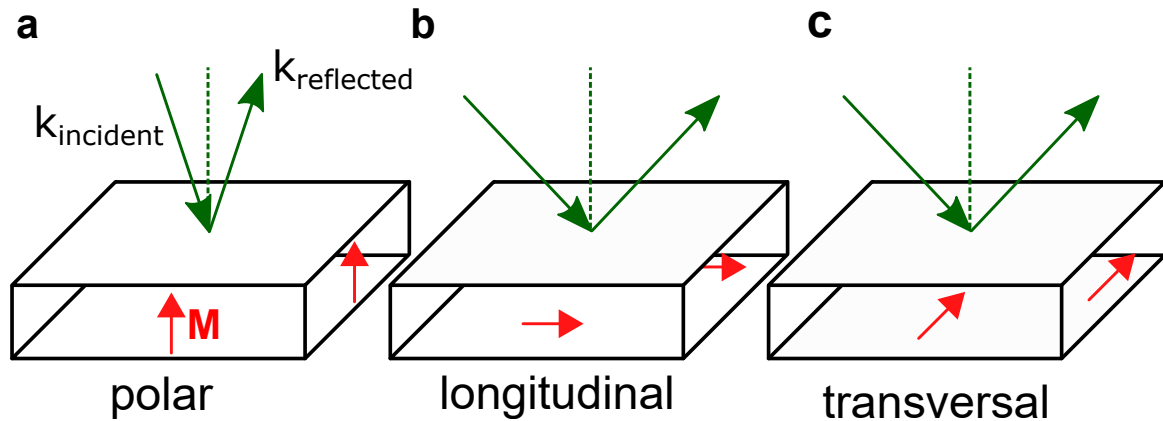
Figure 3.4. – Diagrams of the different types of MOKE. In the diagrams the green arrows represent the direction of the incident and reflected light and the red arrows represent the magnetization orientation. **a**, Polar MOKE, **b**, Longitudinal MOKE. **c**, Transversal MOKE.

of the light. For the polar MOKE (figure 3.4a) the magnetization is aligned along the surface normal, the out-of-plane direction of the magnetic material. This effect is maximal when the angle of incidence is zero, meaning that the rotation of the plane of polarization is the same for all polarization directions of the incident light. For the longitudinal MOKE (figure 3.4b) the magnetization is aligned parallel to the surface of the magnetic material, along the plane of the material, and parallel to the plane of the incident light. The angle of incidence needs to be different to zero or the effect disappears for this geometry. Thus, in this case the incoming light has to be inclined relative to the surface of the material to observe a rotation of the polarization plane of the incident light. For the transverse MOKE (figure 3.4c) the magnetization is aligned parallel to the surface of the magnetic material but perpendicular to the plane of the incident light. The transverse effect causes an amplitude change to the reflected light, but the polarization direction of the Kerr amplitude is the same as that of the regularly reflected light, meaning that it does not experience any rotation. The different types of MOKE can be combined in a quantitative way and a general formula for the MOKE can be derived, see [45] and [90] for detail analysis and description.

A basic MOKE microscope to image magnetic domains or domain boundaries in magnetic materials can be build using regular polarization optics. The scheme of the MOKE microscope used for the MOKE experiments in this thesis can be observed in
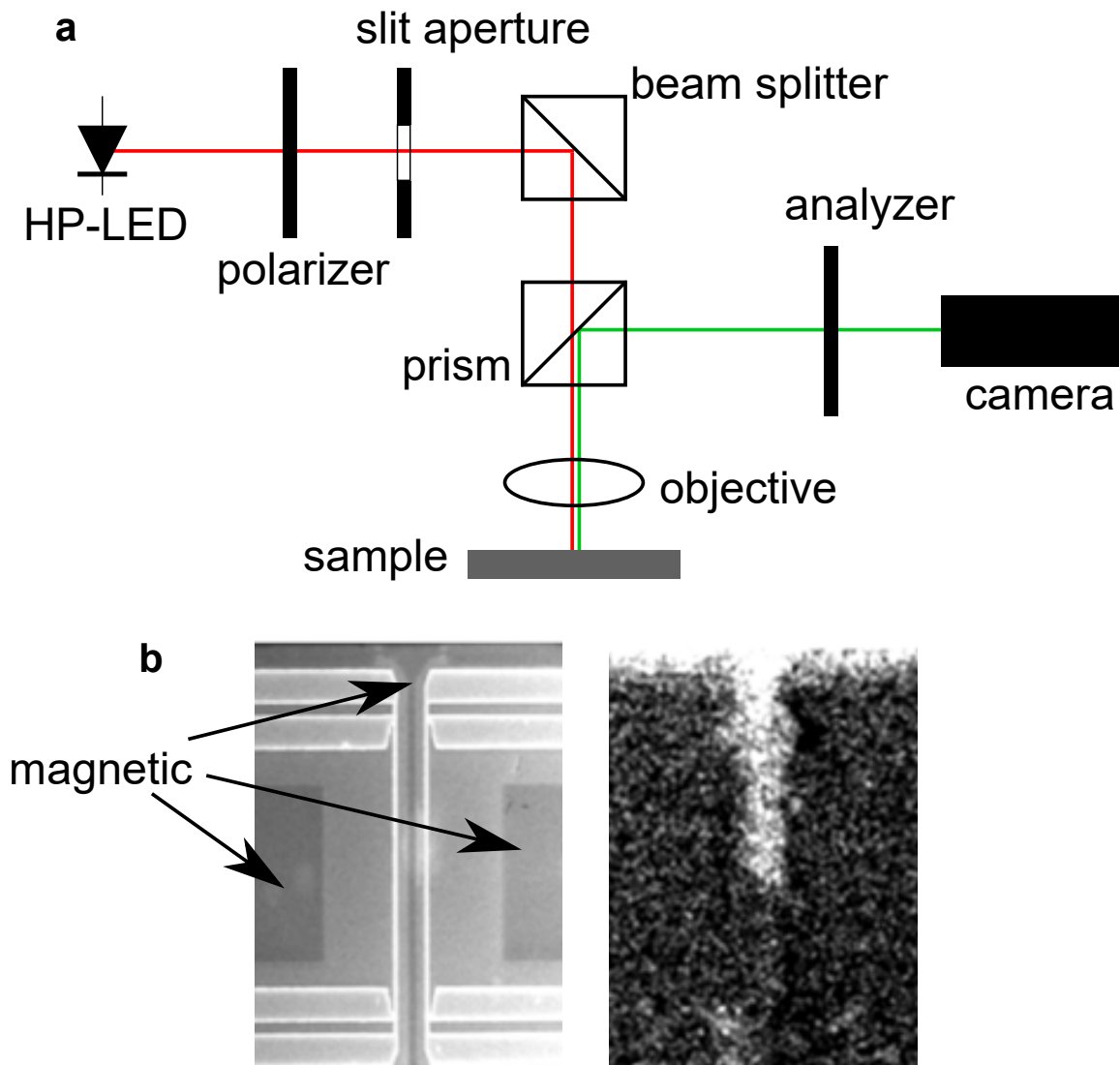
Figure 3.5. – **a**, schema of the MOKE microscope setup. **b**, on the left a microscope image taken with the CCD camera. The arrows indicate the magnetic area of the sample. On the right is the corresponding MOKE image. The magnetization pointing up correspond to the white contrast in the image. The black areas correspond to the magnetization pointing down or nonmagnetic areas. This technique is used to trace the motion of the magnetic domain wall inside the wire.

figure 3.5a. The setup consists of a collimated high power light emitting diode (HP-LED). Optical polarization elements like a rotatable polarizer and analyzer as well an objective lens and a prism. For the detection and imaging of magnetic domains a CCD-based camera was used. To obtain the maximal contrast in the system, between opposite magnetization directions, the polarizer was fixed at an angle and the analyzer was rotated. The maximal contrast was achieved by comparing the intensity of the two different magnetization directions and taking the analyzer angle with the major intensity. The camera system gives also another advantage in which a background image taken at certain magnetization state can be subtracted from the live image, thus the domain structure changes can be visualized with better resolution.

An example of the images taken with the MOKE microscope used in this thesis is depicted in figure 3.5b. On the left side of the figure is a normal picture taken with the camera and on the right side is the corresponding MOKE image. For the MOKE image the contrast was optimized so that the white contrast indicates the magnetization that is pointing perpendicular to the surface of the film in the positive direction. This is achieved by subtracting a reference image when the magnetization was pointing down. The image that is depicted is then a subtraction of the actual state of the magnetization minus the reference image. This means also that the areas that appear black are the areas that are magnetized in the negative direction or the nonmagnetic areas. In this case the type of MOKE measured is the polar MOKE since the magnetization is oriented perpendicular to the surface of the magnetic sample. The image can be used to determine the position of the magnetic domain wall between the up and down magnetized regions inside the wire.

3.3.2. Atomic force microscopy

Since the invention of the scanning tunneling microscope (STM) [91] various types of scanning probe techniques were developed. All these techniques are based on a common principle, that a sharp probe is set to scan very close to the sample surface. Various kinds of probe-sample interactions can be detected with extremely high spatial resolution. One of the most important developments was in 1986 when the atomic force microscope (AFM) was developed [92]. In comparison to the STM, which is restricted only to conducting materials, AFM can determine the topography of any sample. Voigtländer [93] presents a detailed discussion of the principles and other topics for the STM and AFM techniques.
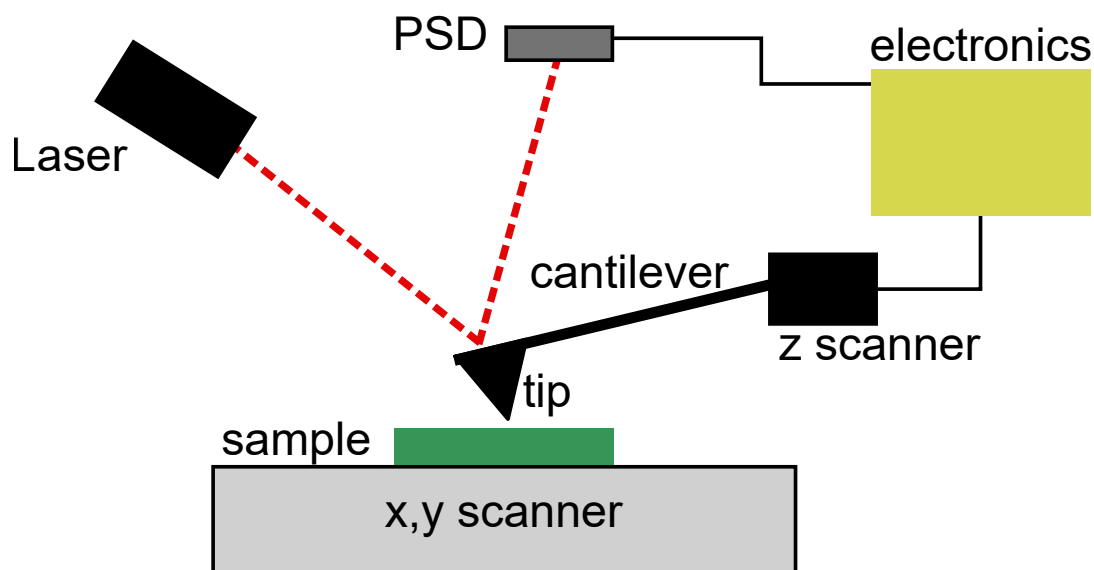
Figure 3.6. – Schematic diagram of an AFM.

Today in common AFMs a cantilever is used to measure the force between the probe and sample. On this cantilever a tip is mounted. The cantilever acts as a spring and its deflection is proportional to the tip-sample force. The force between the tip and sample can be determined by measuring the deflection of the cantilever, which is measured usually by focusing a laser beam on the back side of the cantilever. The reflected beam is crossed with a position sensitive photodetector (PSD). In this arrangement, a small deflection of the cantilever will tilt the reflected beam and change the position of beam on the photodetector. The difference between the two photodiode signals indicates the position of the laser spot on the detector and thus the angular deflection of the cantilever. In figure 3.6 a schematic of an AFM is shown.

There are several AFM operational modes that are divided in two main groups, the static and dynamic modes. One of the most used in the static modes is the contact mode. In this mode, the topography of the sample is mapped while scanning the tip in contact with the sample surface. This is performed by changing the height position of the tip so that the tip-sample force and the tip-sample distance are kept constant. Then the corresponding changes in the height trajectory of the cantilever required to maintain a constant tip-sample distance correspond to the topography of the sample. In the dynamic modes, changes in vibrational properties of the cantilever due to the tip-sample interactions are measured. The cantilever in this case is excited to vibrate close to its resonance frequency. Then, when the tip approaches the surface, the resonance frequency of the cantilever changes due to the tip-sample interaction force which also

results in a change of the cantilever amplitude. The change in amplitude or phase is then used for the force detection and is the feedback parameter to regulate the distance tip-sample. The distance is typically regulated in such way that a constant amplitude and thus a constant force is provided. There are two different approaches in the dynamic modes, the non-contact mode and the intermittent contact mode that is also sometimes called tapping mode. In the non-contact mode, the tip is brought into proximity of the sample surface but without touching it. For the tapping mode, the tip touches the sample surface during the oscillation so that damping of the cantilever oscillation amplitude is induced by the tip-sample interaction that is also present in contact mode. This last operational mode is one of the most common modes in AFM and is used for many applications. The AFM operational modes can be distinguished from a physical point of view, depending on the sign of the forces involved in the tip-sample interaction. In figure 3.7, an idealized plot of the tip-sample forces is shown.
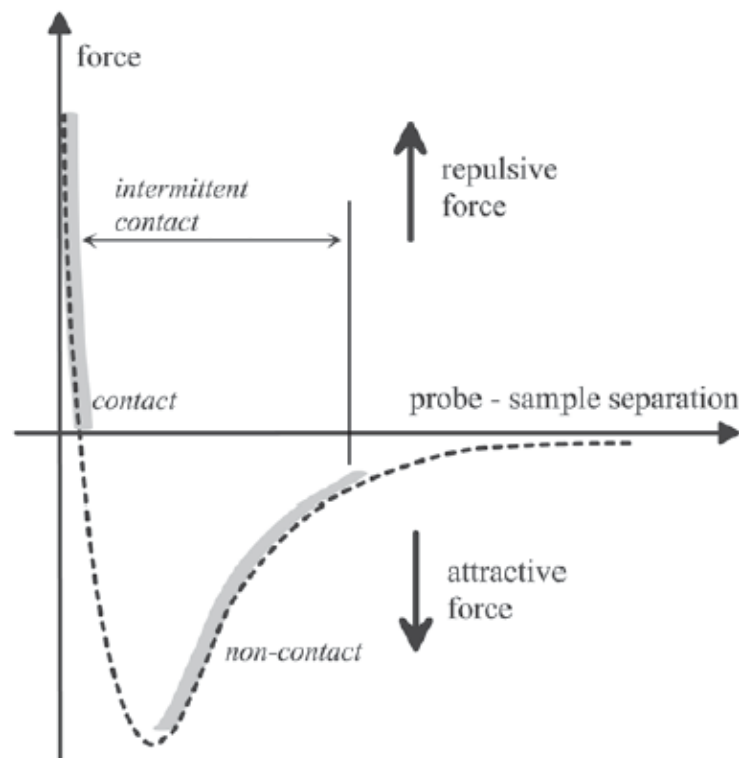
Figure 3.7. – Three different AFM operational modes depending on the force between tip and sample. The region where the AFM operational modes work is highlighted. Figure taken from [94].

48

Independent of the AFM mode used there are several interactions that lead to different types of forces were different parts of the tip and cantilever contribute to the total force that is measured by the AFM. These forces depend strongly on the distance between the tip and the sample. A brief description of the main relevant forces is explained according to [95].

One of the long-range interactions are the electrostatic forces [96]. Their origin can be due to many reasons from charges trapped in the sample surfaces to a potential difference between the tip and the sample. Their strength and distance dependence obey Coulombs law. If the tip-sample system can be considered as a capacitor with a capacitance C distance dependent, the force is given by:

$$F_{\mathrm{el}} = \frac{\partial C}{\partial z} \left(U_{\mathrm{bias}} - U_{\mathrm{cpd}}\right)^2 \tag{3.3}$$

where U_{bias} is the total of an externally applied bias potential between the tip and sample and U_{cpd} is the contact potential difference between the tip and sample. The term $\partial C/\partial z$ depends strongly on the tip shape, and it is difficult to quantify the electrostatic contribution to the total force.

Magnetic forces cause also long-range interactions when the tip and the cantilever are made of an magnetic material. This interaction similar as the electrostatic forces are still present for wide separation of tip and sample well above 10 nm. In section 3.3.3 this interaction is discussed in more detail.

Short-range forces such as the interatomic forces arise in a tip-sample distance below 1 nm. These forces have their origin from the overlap of the electron wave functions and from the repulsion of the ion cores. They decrease very fast with distance because only a few atoms at the very front of the tip contribute to the interaction. This variation in the short-range forces makes it possible to obtain real atomic resolution in the AFM.

Another type of the interaction that are present are the van der Waals forces. Below 10 nm of distance between tip-sample, the influence due to these forces increases. They arise due to the electromagnetic dipole interaction between atoms. These forces are always present and attract even chemically inert noble gas atoms. The van der Waals forces are considered usually with a retarded or non-retarded model depending on whether the finite propagation speed of the electrical field had been taken in-to account or not. At short distances in the non-retarded model these forces decay as $F_{\mathrm{vdW}} \propto 1/r^7$, whereas beyond $r \approx 5$ nm this power law reduces to $F_{\mathrm{vdW}} \propto 1/r^8$.

These forces are strongly dependent on the shape of the bodies that interact. One approximation can be made, if the tip represents a sphere that approaches the sample which is a semi-infinite body, the van der Waals force for this configuration is the following:

$$F_\text{vdW} = \frac{HR}{6z^2} \tag{3.4}$$

where H represents the Hamaker constant which is usually of the order of 10^{-19} J, R is the tip radius and z the distance between tip and sample. Since the actual shape of the tip is not trivial to obtain, is difficult to model the actual distance dependence of the van der Waals force.

3.3.3. Magnetic force microscopy

In the measurements performed along this thesis the tip and sample are of magnetic materials, so the main focus was to study the interactions that rise due to the magnetic forces. In 1987 Martin and Wickmasinghe showed that by changing the non-magnetic tip in an AFM to magnetic tip the magnetic field patterns from a sample could be mapped [97]. They named this scanning probe technique magnetic force microscopy (MFM). Practically every scanning force microscope can be used as an MFM if the tip used has a magnetic moment. Same as in the AFM, in most of the measurements the tip to sample distance is controlled to keep the tip to sample interaction constant. This is mainly because the forces that are measured while measuring the topography are three or two orders of magnitude higher than the magnetic forces. Because of this in the MFM experiments the tip is scanned close to the surface of the sample, but the tip to sample distance must be set sufficiently large to avoid a strong non-magnetic tip to sample interactions that arise due to the topography dependent forces.

The origin of the magnetic force is due to the interaction of the magnetic dipole moments of a magnetic tip (or also the cantilever) and the magnetic stray field that is produced by a magnetic sample. This interaction can be calculated from the total magnetostatic energy of the tip-sample system:

$$E\left(r, z\right) = -\mu_0 \int_{r'} \int_{z'} M_\text{tip}\left(r', z'\right) H_\text{sample}\left(r + r', z + z'\right) dr'dz' \tag{3.5}$$
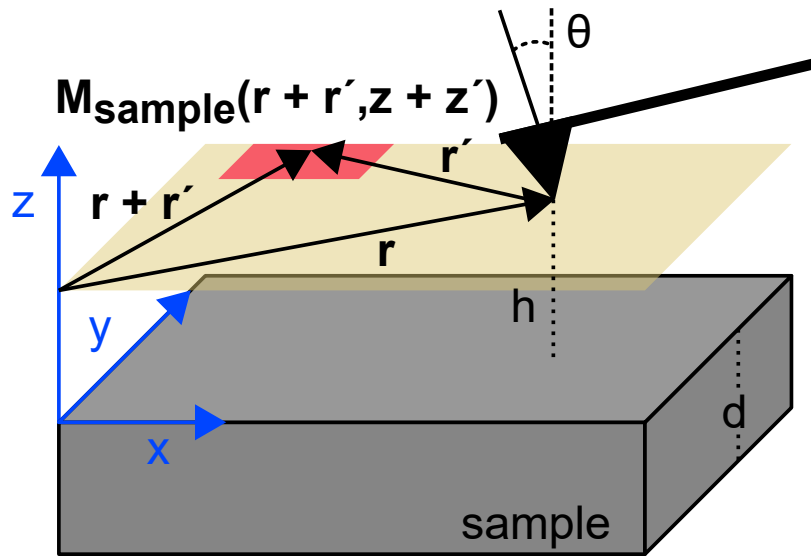
Figure 3.8. – Coordinate system for the magnetic force interaction between tip and sample in the plane of the tip apex. Here h represents the distance between the tip and the sample and d the sample thickness.

where μ_0 is the vacuum permeability, M_{tip} is the local magnetic moment of the tip and H_{sample} is the stray field coming out of the sample. The variables $r' = (x', y')$ and z' refer to the tip coordinate system while $r = (x, y)$ and z are referenced to the global coordinate system of the scanner, see figure 3.8 for coordinate system. From this equation the force acting on the tip can be obtained as follows:

$$F_z\left(r, z\right) = -\frac{\partial E\left(r, z\right)}{\partial z} = -\mu_0 \int_{r'} \int_{z'} M_{\text{tip}}\left(r', z'\right) \frac{\partial H_{\text{sample}}\left(r + r', z + z'\right)}{\partial z} dr' dz' \quad (3.6)$$

Using equation 3.5 and equation 3.6, the size and the range of the magnetic force interaction can be calculated. These quantities depend strongly on the tip-sample configuration. Also, the range of the magnetic force depends strongly on the decay of the stray field outside of the sample and therefore on the size of the domain structure of the sample and its thickness.

There are different modalities how the interaction due the magnetic forces can be measured [98]. One of the most used common modes is the two-pass technique or sometimes called lift mode [99]. This mode consists of two steps (figure 3.9). In the first step the topography is mapped in the tapping mode known from the AFM. Sometimes the two steps are recorded twice (for and back) to rule out some artifacts
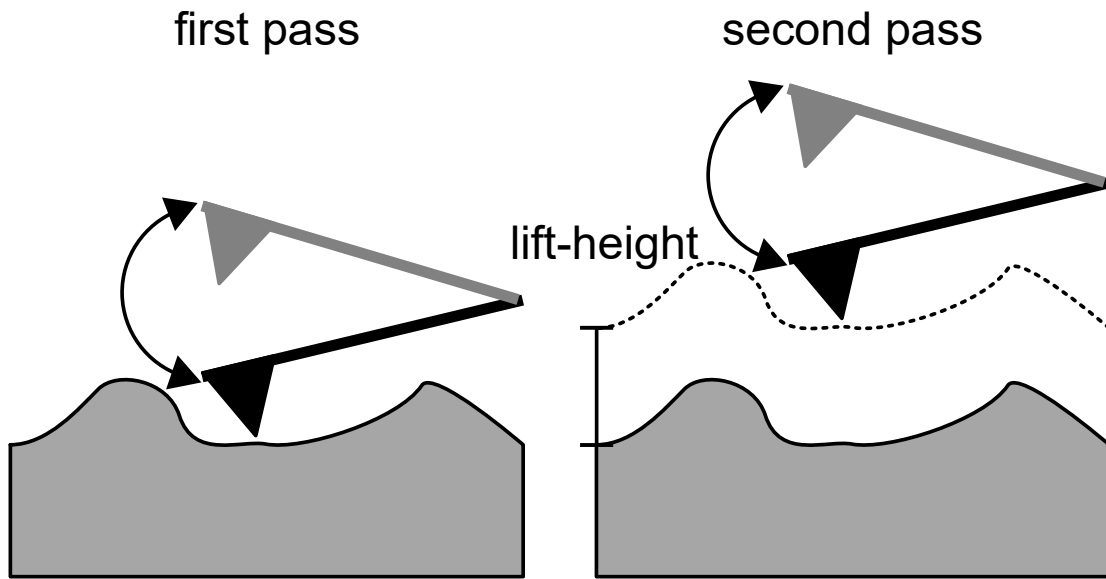
Figure 3.9. – Schematic of the two-pass mode in the MFM. In the first pass the to-
pography of the sample is obtained. In the second pass the long-range
interactions such as the magnetic forces are obtained.

coming from the tip. Then in the second step the same line is scanned again following
the topography measurements in the first step, but the tip is lifted a certain height from
the topography profile, this height is usually called *lift height*. The second step is where
the long-range interactions are mapped such as the magnetic forces. This interaction
is usually determined by the phase shift between the cantilever oscillation and the
corresponding drive amplitude of the cantilever. According to [100] the phase shift in
radians from the cantilever oscillation due to an force interaction can be approximated
as:

$$\Delta\phi \approx \frac{180}{\pi}\frac{Q}{c}\frac{\partial F_z}{\partial z} \tag{3.7}$$

where Q is the quality factor and c the spring constant of the cantilever. The term
$\partial F_z/\partial z$ in first approximation represents all the force gradients that are acting on the
cantilever. The quality factor Q describes the amount of energy that a cantilever dissi-
pates in a single oscillation cycle through vicious damping [101] and can be expressed
as:

$$Q = 2\pi\frac{w}{\Delta w} \tag{3.8}$$

52

where W is the stored vibrational energy and ΔW is he total loss energy per cycle of vibration. There are several physical mechanism that contribute to the energy loss of the cantilever [102]. Experimentally it has been shown that one of the biggest energy loss mechanism its due to the medium surrounding the cantilever so by performing the measurements in vacuum the cantilever quality factor increases dramatically [103].

3.3.4. Quantitative analysis of MFM stray fields

Until this point the working principle and the detection mechanism of the magnetic forces emanating from the sample were explained for an MFM. The signal generation is discussed together with the scanning concept. At this point, it is possible to measure MFM qualitative phase shift images of a given sample. In the following a calibration approach will be shown that allows to calculate quantitative magnetic field data from the measured phase data in conjunction with parameters such as the quality factor and the spring constant of the cantilever. This is based on the determination of a tip transfer function (TTF) [104]. It requires the calibration of the tip using a well characterized reference sample [105]. In such a reference sample the stray field pattern can be calculated from a guess of the sample domain pattern. The magnetic properties of the sample as anisotropies and saturation magnetization must be predetermined. Another important consideration is that the sample should have very well defined perpendicular magnetic anisotropy. A comparison of different suitable samples for the TTF approach was made in [106, 107]. As a good candidate for a reference sample Co/Pt multilayer exhibits stable magnetic properties, strong perpendicular magnetic anisotropy and their domain or stray field pattern can be quantitatively constructed from the measured phase shift MFM data without calibrating the MFM tip.

In figure 3.10 a scheme of the calibration procedure of the MFM tip is shown. This procedure is going to be explained briefly next by deriving the fundamental equations necessary to understand the physical phenomena.

A quantitative analysis of the MFM images requires an inversion of the three-dimensional spatial correlation integral discussed in equation 3.5 to obtain the field from the measured stray field image. This is much simpler if one works in a partial Fourier space. This simplifies the mathematics since the related correlation integrals transform into multiplicative functions called transfer functions [104]. The partial (2D) Fourier transform maps the (x, y, z) space to the (k_x, k_y, z) space with $\mathbf{k} = (k_x, k_y)$ and $k = |\mathbf{k}|$. It can be shown, that above the sample surface, where the magnetic field is rotation free,
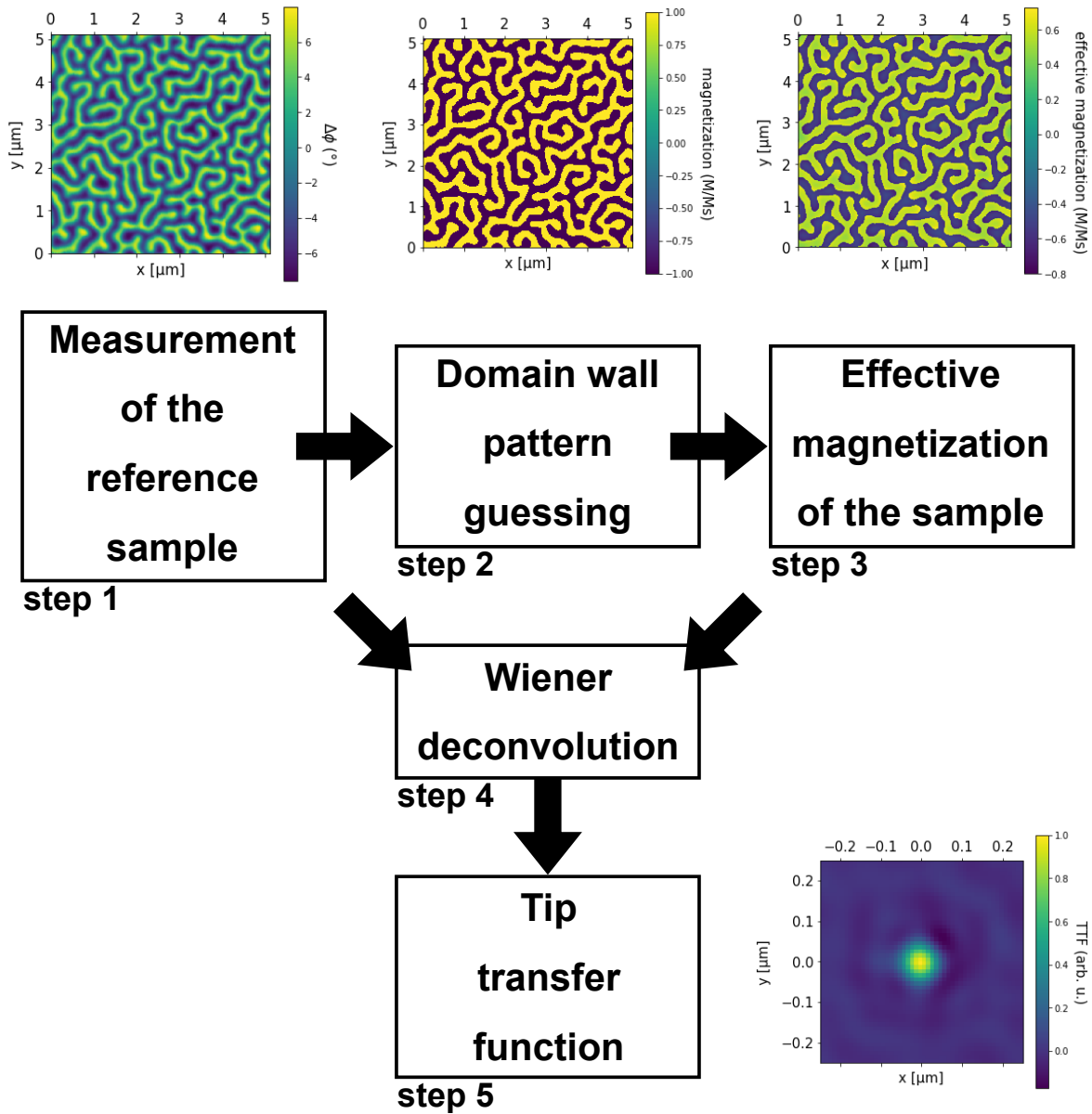
Figure 3.10. – Scheme of the calibration procedure of an MFM tip. Step 1, MFM phase measurement of the reference sample. Step 2, discrimination process and domain wall guessing of the reference sample. Step 3, calculation of the total magnetization of the sample. Step 4, The Wiener deconvolution can be applied using the MFM phase measurement and the calculated effective magnetization of the sample. Step 5, calculation of the TTF of the calibrated MFM tip.

a magnetic scalar potential $\mathbf{M}(\mathbf{k})$ can be used. Here, the ∇ operator becomes:

$$\nabla = (\mathrm{i}k_x, \mathrm{i}k_y, k_z) \tag{3.9}$$

Thereby, in the partial Fourier space, the magnetic field $\mathbf{H}(\mathbf{k}, z)$ can be calculated from its z-component $H_z(\mathbf{k}, z)$ following:

$$\mathbf{H}(\mathbf{k}, z) = -\frac{1}{k}\nabla(\mathbf{k})H_z(\mathbf{k}, z) \tag{3.10}$$

For a sample with film thickness d and independent uniform magnetization $\mathbf{M}(\mathbf{k})$, the stray field can be calculated following:

$$\mathbf{H}(\mathbf{k}, z) = -\frac{\nabla(\mathbf{k})}{k}\frac{\left(1 - e^{-kd}\right)e^{-kz}}{2}\begin{pmatrix} -\mathrm{i}k_x/k \\ -\mathrm{i}k_y/k \\ 1 \end{pmatrix}\mathbf{M}(\mathbf{k}) \tag{3.11}$$

in this equation, z represents the distance above the surface of the sample. When a sample is magnetized only in the perpendicular direction, this equation can be simplified to:

$$\mathbf{H}(\mathbf{k}, z) = \frac{\left(1 - e^{-kd}\right)e^{-kz}}{2}\mathbf{M}(\mathbf{k}) \tag{3.12}$$

From equation 3.6 the magnetic force acting on the MFM tip is known. When applying the partial Fourier transform to equation 3.6, the x-y part of the correlation integral becomes a multiplication, using the identity in equation 3.9 the force can be expressed in the following manner:

$$\begin{aligned} F_z(\mathbf{k}, z) &= \mu_0 \int_{z'} \hat{M}_{\text{tip}}(\mathbf{k}, z')\frac{\partial H_{\text{sample}}(\mathbf{k}, z + z')}{\partial z}dz' \\ &= \mu_0 \int_{z'} \hat{M}_{\text{tip}}(\mathbf{k}, z')(-k)H_{\text{sample}}(\mathbf{k}, z + z')\,dz' \\ &= \mu_0 H_{\text{sample}}(\mathbf{k}, z)\int_{z'} e^{-kz'}(-k)\hat{M}_{\text{tip}}(\mathbf{k}, z')\,dz' \\ &\equiv -\mu_0 H_{\text{sample}}(\mathbf{k}, z)\hat{\sigma}(\mathbf{k}) \end{aligned} \tag{3.13}$$

where $\hat{\sigma}(\mathbf{k})$ is defined as the effective magnetic charge distribution of the magnetic tip, projected onto a plane located at the tip apex. The measured phase shift then can be calculated from equation 3.7 as:

$$
\begin{aligned}
\Delta\phi\left(\mathbf{k}, z\right) &= \frac{180}{\pi} \frac{Q}{c} \frac{\partial F_z}{\partial z} \\
&= -\mu_0 \frac{180}{\pi} \frac{Q}{c} \frac{\partial H_{sample}\left(\mathbf{k}, z\right)}{\partial z} \hat{\sigma}\left(\mathbf{k}\right)
\end{aligned}
\tag{3.14}
$$

If this Fourier transform is transformed from a continuous Fourier transform to a discrete Fourier transform (DFT) the force gradient becomes:

$$
\begin{aligned}
\Delta\phi\left(\mathbf{k}, z\right)|_{DFT} &= -\mu_0 \frac{180}{\pi} \frac{Q}{c} \cdot \delta A_{pixel} \cdot \hat{\sigma}\left(\mathbf{k}\right)|_{DFT} \cdot \frac{\partial H_{sample}\left(\mathbf{k}, z\right)}{\partial z}|_{DFT} \\
&= -\mu_0 \frac{180}{\pi} \frac{Q}{c} \cdot \delta A_{pixel} \cdot \hat{\sigma}\left(\mathbf{k}\right)|_{DFT} \cdot k \cdot H_{sample}\left(\mathbf{k}, z\right)|_{DFT}
\end{aligned}
\tag{3.15}
$$

where the additional term in the equation δA_{pixel} is the pixel area.

In the conventional MFM measurement setups, the cantilever has a canting angle θ with respect to the measurement plane as can be observed in figure 3.8, and the cantilever oscillates with finite amplitude. Both effects can be numerically corrected by multiplying the right side of equation 3.15 with a cantilever correction factor (LCF) that can be derived as discussed in [108]. If the cantilever has an oscillation amplitude A_0 and defining $\hat{z} = A_0 \mathbf{n}\nabla$, where $\mathbf{n}$ is the angle between the tip long axis and the sample surface normal, the LCF becomes:

$$
LCF = -\frac{1}{A_0} \frac{1}{k} \mathbf{n}\nabla I_1\left(\hat{z}\right) \frac{1}{-k}
\tag{3.16}
$$

With the cantilever canting angle and amplitude correction, and using equation 3.12, equation 3.15 becomes:

$$
\Delta\phi\left(\mathbf{k}, z\right) = -\mu_0 \frac{180}{\pi} \frac{Q}{c} \delta A_{pixel} LCF \hat{\sigma}\left(\mathbf{k}\right) k \frac{\left(1 - e^{-kd}\right) e^{-kz}}{2} M_s m\left(\mathbf{k}\right)
\tag{3.17}
$$

with $\mathbf{M}\left(\mathbf{k}\right) = M_s m\left(\mathbf{k}\right)$, where $m\left(\mathbf{k}\right)$ is the normalized magnetization distribution. The goal of this analysis is to determine $\hat{\sigma}\left(\mathbf{k}\right)$ that describes the magnetic tip, so that

the stray field from unknown samples can be quantified. This is done by measuring a reference sample with the MFM tip resulting in a phase shift image, first step in figure 3.10. As already mentioned, the reference sample is well characterized, and its magnetization distribution can be estimated by applying a discrimination process to the measured phase signal (step 2 in figure 3.10), i.e. the image obtained from the measured data is converted in a binary image $m(\mathbf{k})$. To describe better the domains, domain wall transitions are added. The effective magnetization depends also on the thickness of the sample and the distance where the measurements were performed (lift height). Thus, the magnetization of the sample becomes $M_{\text{sample}} = M_s m(\mathbf{k})\left(1 - e^{-kd}\right)e^{-kz}$, this relationship allows to calculate the total magnetization of the sample (step 3 in figure 3.10). The following constant that includes most of the experimental parameters can be defined:

$$C_1 \equiv \mu_0 \frac{180}{\pi}\frac{Q}{c}\delta A_{pixel}M_s \tag{3.18}$$

with this constant, equation 3.17 can be written as:

$$\Delta\phi(\mathbf{k}, z) = -C_1\frac{1}{2}LCF\,k\,m(\mathbf{k})\left(1 - e^{-kd}\right)e^{-kz}\hat{\sigma}(\mathbf{k}) \tag{3.19}$$

In the field of image analysis and signal processing, by using a Wiener filter which is used for the deconvolution an estimate of an unknown signal can be obtained by filtering a noisy observation of the signal. For a convolution formula $G(\mathbf{k}, z) = H(\mathbf{k}, z)F(\mathbf{k}, z)$ the Wiener deconvolution formula can be expressed as:

$$F(\mathbf{k}, z) = G(\mathbf{k}, z)\frac{\hat{H}(\mathbf{k}, z)}{|H(\mathbf{k}, z)|^2 + \alpha} \tag{3.20}$$

where the last term in the equation is the Wiener filter. The constant α is the frequency spectra of the noise. By this constant the Wiener filter attenuates the frequencies dependent on their signal-to-noise ratio. During the deconvolution process, the α constant can be obtained from the L-curve criterion [109]. This is done by determining the α that maximizes the curvature of the L-curve. From equation 3.19 we can define the following:

$$G(\mathbf{k}, z) \equiv \Delta\phi(\mathbf{k}, z) \tag{3.21}$$

57

$$H\left(\mathbf{k}, z\right) \equiv \frac{1}{2} LCF\, k\, m\left(\mathbf{k}\right) \left(1 - e^{-kd}\right) e^{-kz} = LCF\, k\, H_{sample}\left(\mathbf{k}, z\right) \tag{3.22}$$

$$F\left(\mathbf{k}, z\right) \equiv C_1 \hat{\sigma}\left(\mathbf{k}\right) \tag{3.23}$$

By this the Wiener deconvolution can be applied to our problem (step 4 in figure 3.10). A Tip Transfer Function, $TTF\left(\mathbf{k}, z\right) = \hat{\sigma}\left(\mathbf{k}\right)$ can be expressed as:

$$TTF\left(\mathbf{k}, z\right) = \frac{1}{C_1} \hat{F}\left(\mathbf{k}, z\right) \tag{3.24}$$

With this procedure the stray field of the MFM tip determined by measuring the phase shift induced by the magnetic sample-tip interaction and calculating the effective magnetization of the measured sample. Now, that the TTF of the tip is known (the tip is calibrated, step 5 in figure 3.10) the magnetic field distribution of an unknown sample can be calculated by another Wiener deconvolution, defining the following:

$$G\left(\mathbf{k}, z\right) \equiv \Delta\phi\left(\mathbf{k}, z\right) \tag{3.25}$$

$$H\left(\mathbf{k}, z\right) \equiv C_1 \frac{1}{2} LCF\, k\, \hat{\sigma}\left(\mathbf{k}\right) \tag{3.26}$$

$$F\left(\mathbf{k}, z\right) \equiv H_{sample}\left(\mathbf{k}, z\right) \tag{3.27}$$

3.4. Thermo-electrical measurement setups

In this thesis three different main measurement setups for thermo-electrical measurements were used. These setups correspond to the different investigations performed on the devices presented in this thesis. The setups are going to be introduce accordingly to the specific device used.

3.4.1. Permalloy devices

The measurements were performed in a He flow cryostat with variable temperature inset (VTI). from Oxford Instruments NanoScience. Temperatures could be varied from 1.2 K to 300 K. In figure 3.11 the setup is shown. In particular this cryostat was equipped with a vector magnet in which a 3D-vector magnetic field could be applied up to 1 T, enabling rotational measurements with a fixed magnetic field along different planes. Also, in one direction (z direction, or out-of-plane direction in our reference system) a magnetic field up to 9 T could be applied. The devices were glued to a chip carrier and electrically connected by means of bonding. The chip carrier was mounted on a sample rod which was electrically connected to the outside of the cryostat and connected to a connection box to further connect the measuring equipment. Near the chip carrier a Cernox temperature sensor was installed so that the real ambient temperature of the device could be measured.

3.4.2. (Ga,As)(Mn,P) devices

The measurements were performed in collaboration with Jörg Wunderlich, Tomas Janda and Vit Saidl at the Faculty of Mathematics and Physics in the Charles University in Prague in the Laboratory of Opto-Spintronics. In figure 3.12 an image of the experimental setup is shown. The setup is based on the schema presented in section 3.3.1 in figure 3.5a. The setup consisted of a variable temperature cold-finger cryostat, were temperatures in the range of 4 K to 300 K could be stabilized. A commercial Cernox temperature sensor was installed near the device area so that the real ambient temperature of the device could be measured. For the measurements the device was glued on a PCV chip carrier and electrically contacted by means of bonding. The PCV chip carrier was electrically connected to the outside of the cryostat and connected vi a connection box to further connect the measuring equipment. The cryostat had windows so that optical experiment could be performed at low temperatures. Magnetic fields were applied by an electromagnet which was surrounding the cold-finger cryostat, so that the device area was centered between the pole shoes of the electromagnet.

3.4.3. Skyrmion devices

The anomalous Nernst effect and MFM measurements were performed in a NT-MDT Aura scanning probe microscope (SPM) in ambient temperature. The setup is shown in figure 3.13. The measurements were carried out at the National Physical Laboratory, NPL, Teddington, UK in the group of Olga Kazakova in collaboration with Craig Barton and Héctor Corte-León. In this SPM system all the electronics (i.e. the laser and the position sensitive photodetector) was built in the scanning head. The height and the position of the scanning head was controlled by the corresponding software provided by the manufacturing company of the SPM. Cantilever chips with an MFM tip were fixed mechanically to the scanning head. The sample was glued to a PCV chip carrier and the sample was electrical connected by means of bonding. The PCV chip carrier was electrically connected to a connection box to further connect the measuring equipment. The bonding was performed in such manner that while scanning the MFM tip on the sample surface the cantilever and tip would not touch the bonding wires.

In the measurements the magnetic fields were applied by a built-in electromagnet below the sample. Commercial low magnetic moment MFM tips (NT-MDT MFM/LM) were used. Before performing the MFM measurements, the magnetic tip was magnetized in the positive direction out-of-plane with respect to the sample (same as the applied field). From just the direction of the magnetization of the tip the contrast of the phase shift cannot at priory be known. To determine the contrast shift, the magnetization of the sample was studied in the presence of an applied magnetic field. The black domains decreased in size as the magnetic field was applied in the out-of-plane positive direction, so that the white contrast areas correspond to the opposite direction. This is the case for almost all the measurements. In the measurements where this does not apply it is indicated in the text. The MFM images were taken with an estimated oscillation amplitude of 170 nm of the cantilever and a lift height of 50 nm. In all the MFM measurements where the ANE was measured simultaneously, a current was applied to the microheater during the whole measurement.
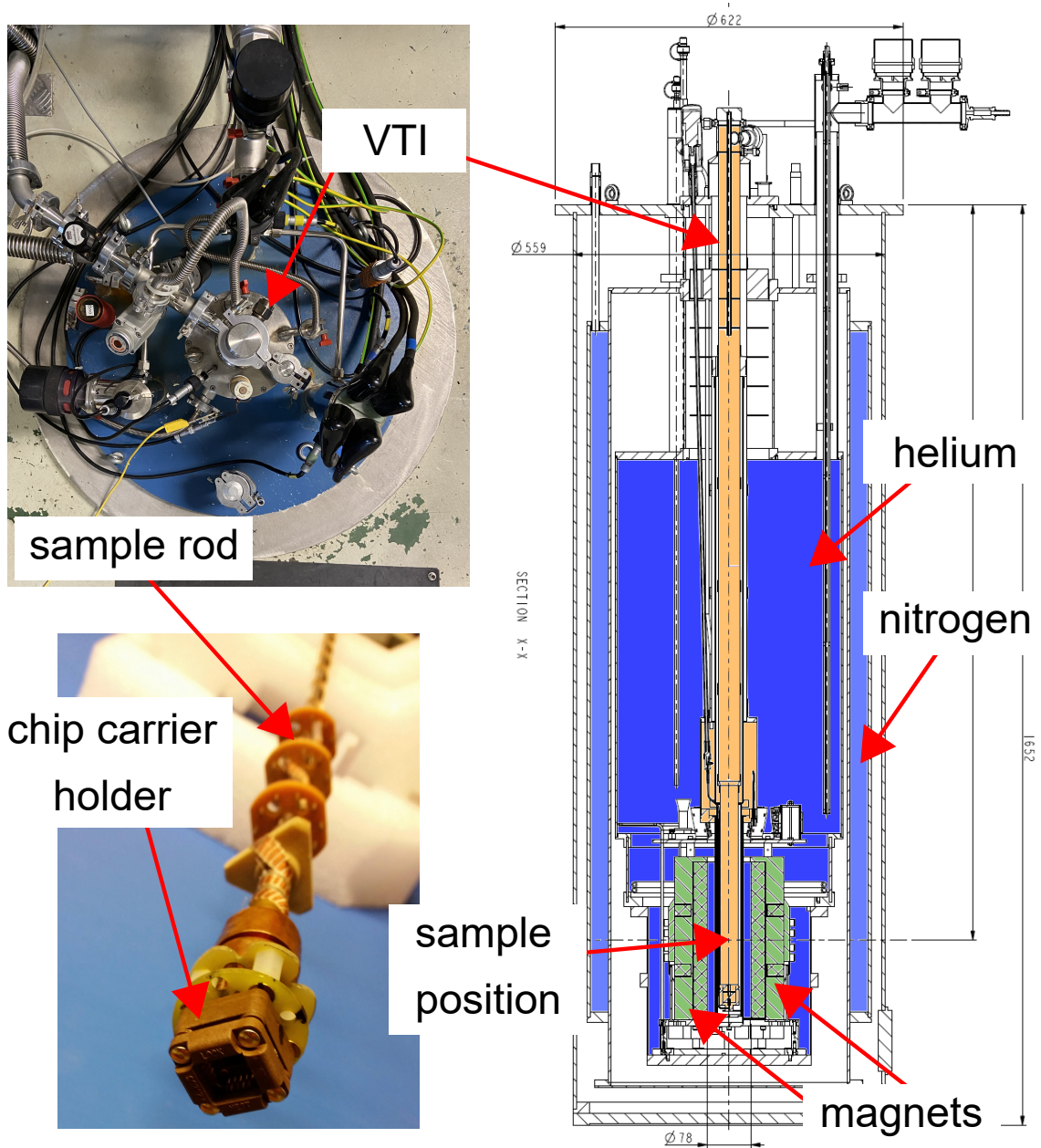
Figure 3.11. – Top view of the cryostat and the sample rod. In the technical layout of the cryostat the different relevant parts of the cryostat are marked.
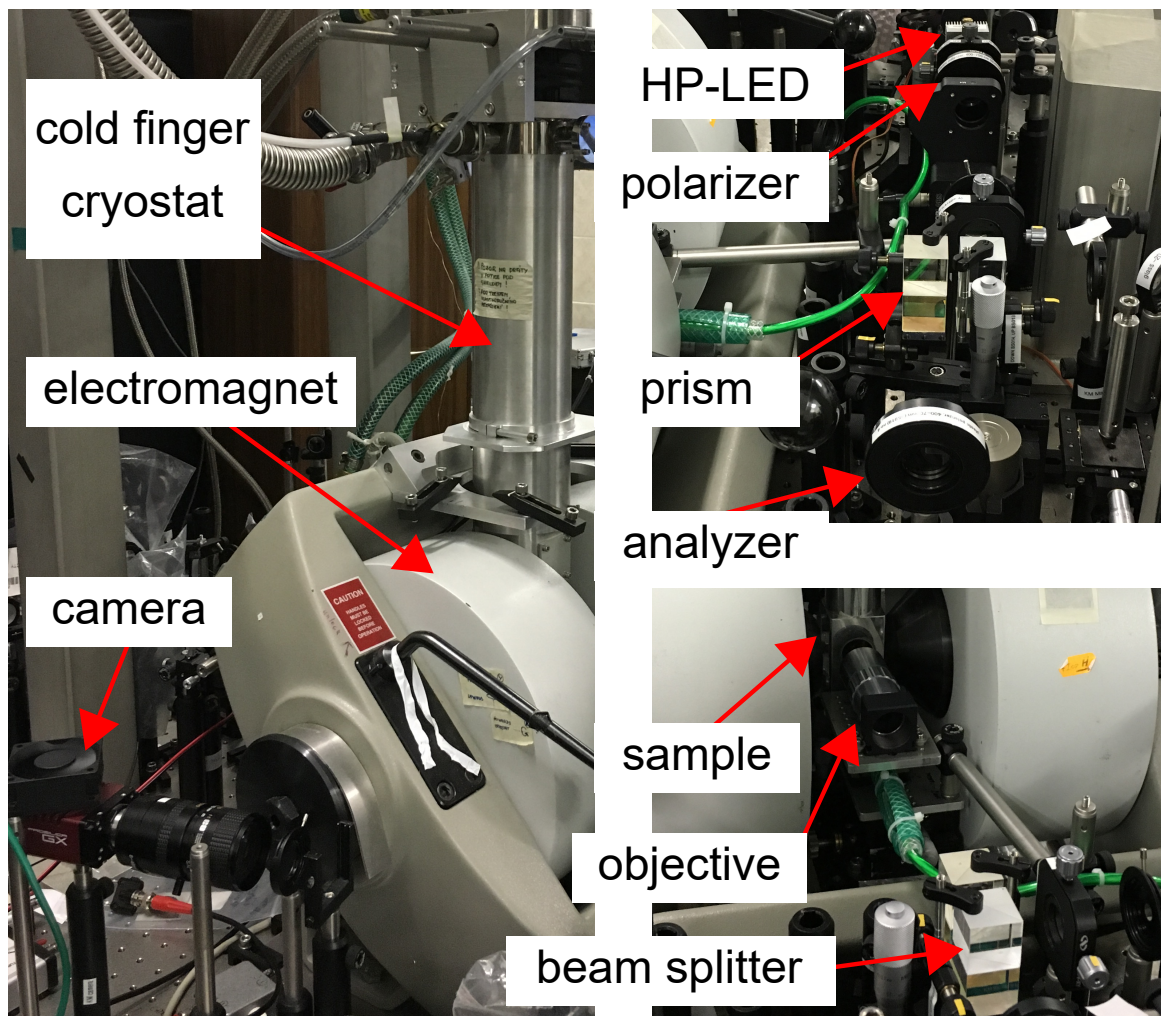
Figure 3.12. – MOKE setup and a cold finger cryostat. All the polarizing optics described in the scheme of figure 3.5a are depicted in the images. With this setup MOKE measurements could be performed at low temperatures.
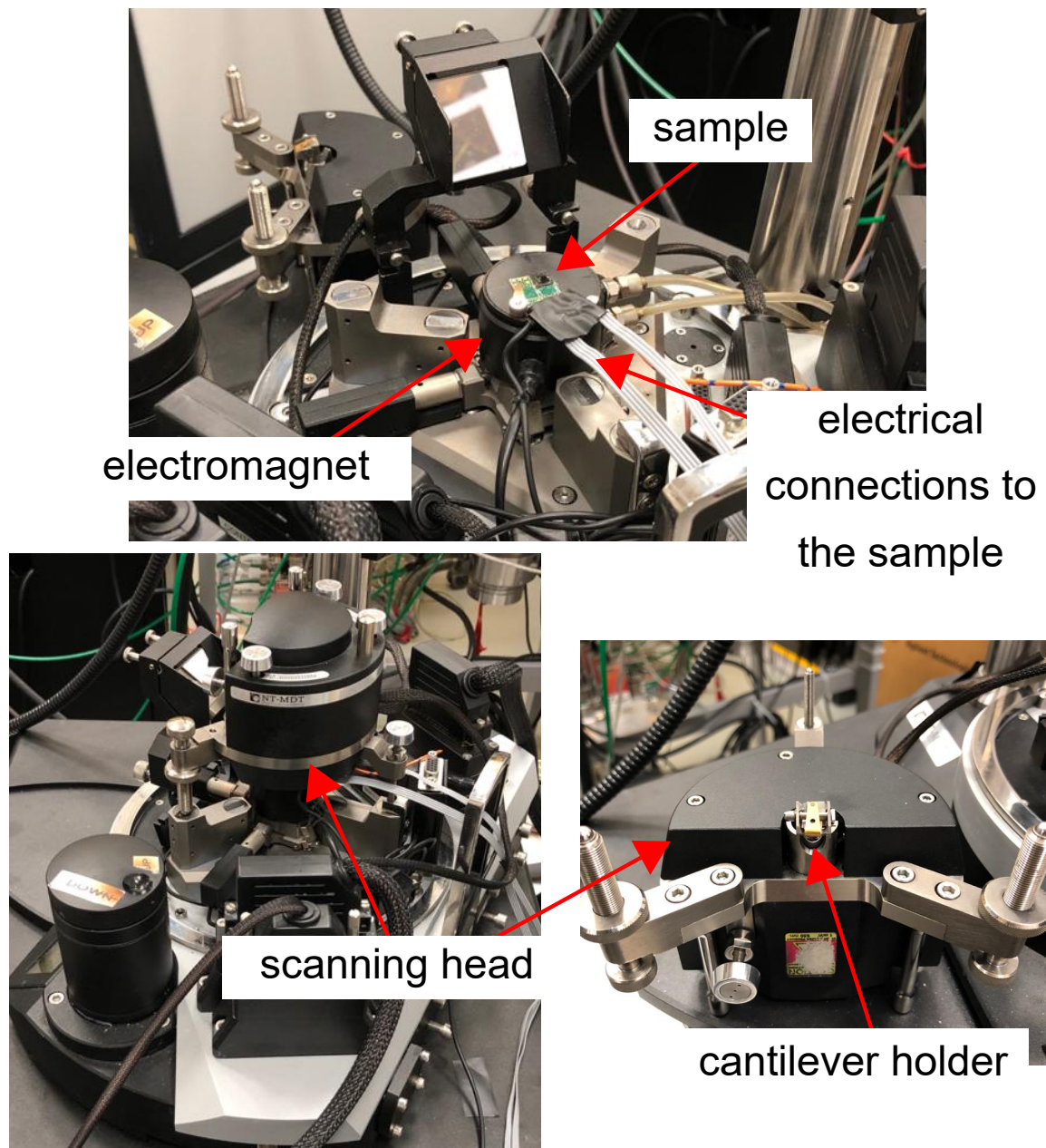
Figure 3.13. – NT-MDT Aura scanning probe microscope. The sample is bonded to a PCV chip carrier that is connected electrically to a connection box. The sample is on top of an electromagnet. The scanning head contains all the electronics necessary to perform MFM measurements. This setup allowed simultaneously perform MFM measurements in combination with ANE measurements.

4. Permalloy devices

In this chapter, a new measurement procedure is described. This procedure, named "two-heater procedure", allows to separate unwanted/parasitic thermal gradients that arise in thermoelectric measurements which contribute to the total measured voltage signal. It also allows to selectively separate from the total measured signal, the components of the signal, that are dependent on the different magnetization directions in the magnetic material. The procedure is based on the thermoelectric transport equations introduced in chapter 2 section 2.4.2. Experimentally the procedure was confirmed using a Permalloy (Py) device fabricated according to the fabrication steps introduced in chapter 3 section 3.1.

4.1. Unwanted thermal gradients

The generation of thermal gradients in micro devices is usually performed by means of Joule heating of a metallic stripe. This then generates a thermal gradient across the device parting from the metallic stripe. Suppose a thermal gradient purely along the x-direction needs to be generated in a device configuration showed in figure 4.1. Due to Joule heating of the heater a gradient along the x-direction is generated. Since the thermal conduction occurs through the substrate, and the substrate is at a higher temperature than the ambient temperature a gradient in the z-direction is also generated. The creation of an additional gradient along the z-direction is usually hard to avoid in devices that have the configuration of figure 4.1. Since the z-component of the thermal gradient is not created intentionally it is sometimes referred to as unwanted/parasitic. Additionally, its magnitude is less accessible experimentally since no thermometers can be fabricated along this direction making it difficult to estimate what contribution this unwanted thermal gradient has to the total measured signal.

Understanding unwanted thermal gradients is important in experiments that involve effects such as the spin Seebeck effect (SSE), where a thermally produced spin current

65
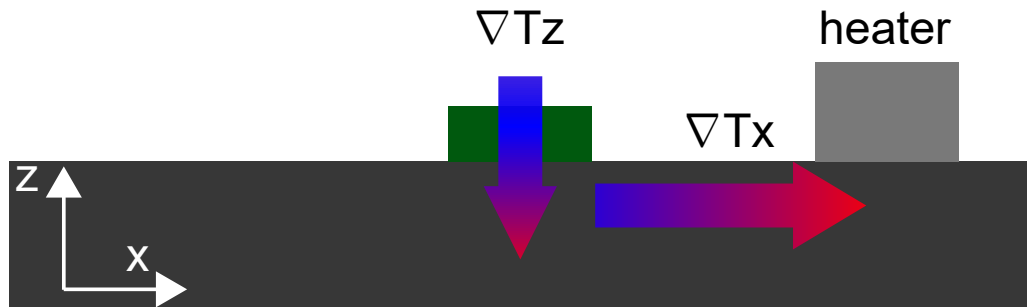
Figure 4.1. – Schematic side view of a usual device used to study thermoelectric effects. The magnetic material is depicted in green and is located next to a heater. Two possible thermal gradients are present in the device when a current is applied to the heater.

can be generated over a long distance in a magnet without electric currents [110, 111]. The existence of these effects was initially fundamentally doubted and then confirmed by angle dependent measurements of the magnetization, due to this the direction of the thermal gradient plays an important role. In general, the SSE has been observed in two distinct device configurations and materials, namely, longitudinal (LSSE) [11, 112, 113] and transverse (TSSE) [114–116]. In these configurations, unwanted thermal gradients can produce a mixture of effects that influence the measured signal [10, 12, 13, 117].

In this section the influence of unwanted thermal gradients in the measured voltage signal are discussed. In the device configuration depicted in figure 4.1, where the nanowire is next to the heater, two thermal gradients are present along the x-axis and z-axis. To simplify the nomenclature in this chapter, the thermal gradient along the x-axis and z-axis are going to be denoted by ∇T_x and ∇T_z respectively

If a DC current is applied to the heater in figure 4.1 and if the thermal gradient in the y-axis can be neglected (for the case that the heaters are longer than the micro/nanowire) the equation 2.44 in chapter 2 section 2.4.2 becomes:

$$
\begin{aligned}
E_y = \left(S_\parallel - S_\perp \right) & \left[\nabla T_x \sin^2\left(\mathrm{b}\right) \sin\left(\mathrm{a}\right) \cos\left(\mathrm{a}\right) + \nabla T_z \sin\left(\mathrm{b}\right) \cos\left(\mathrm{b}\right) \sin\left(\mathrm{a}\right) \right] \\
& - S_\mathrm{N} \left[\nabla T_x \cos\left(\mathrm{b}\right) - \nabla T_z \sin\left(\mathrm{b}\right) \cos\left(\mathrm{a}\right) \right]
\end{aligned}
\tag{4.1}
$$

In equation 4.1, ∇T_x and ∇T_z contribute to the y-direction of the total net electrical

field. The measurement is not sensitive to the other components of the $\boldsymbol{E}$ vector due to the orientation of the magnetic nanowire along the y-axis. To demonstrate the impact of ∇T_z one can simulate the total net electric field produced by the thermal gradients using literature values of the Seebeck and Nernst coefficients. To further simplify the discussion, it is assumed that the magnetization lies purely in the sample plane (x-axis and y-axis, $b = 90°$ see figure 2.10b for reference system). In this case the equation 4.1 reduces to:

$$E_{y;in-plane} = \left(S_\parallel - S_\perp \right) \nabla T_x \sin\left(a\right) \cos\left(a\right) + S_N \nabla T_z \cos\left(a\right) \qquad (4.2)$$

Note that even if the magnetization is forced to be in-plane the thermal gradients still can point in the x-direction and z-direction and contribute to the total net electric field. In figure 4.2 some examples of the net electrical field calculated from equation 4.2 are shown, where different ratios between ∇T_x and ∇T_z have been considered. For the calculation it was also assumed that the magnetization rotates and follows strictly the direction of the angle a (see figure 2.10b for reference system), which would be the case if an external magnetic field with an amplitude higher or same as the saturation magnetization is applied to the device. The values for the thermoelectric coefficients were taken from [5] for the Seebeck coefficients and [7] for the Nernst coefficient. In both references these coefficients are obtained by performing thermoelectric measurement as a function of the magnetic field at room temperature on a Py nanowire and a Py/Cu multiterminal lateral spin valve. For the case of Py the Nernst coefficient is higher $(-2.6 \ \mu V \, K^{-1})$ than the difference between the longitudinal and transverse Seebeck coefficient $(S_\parallel - S_\perp = 0.2 \ \mu V \, K^{-1})$. These two coefficients depend on the material and are temperature dependent. In particular the Nernst coefficient in Py is higher in comparison to other materials, one reason for this is that Py is less conductive than ordinary ferromagnetic materials [7]. The difference in value of the thermoelectric coefficients (Nernst and Seebeck) and the amplitude of the thermal gradients would affect the dependency of the net electric field expressed in equation 4.2. If the two thermal gradients have the same amplitude as shown in figure 4.2a, the electric field has a cosine shape dependency. If the amplitude of ∇T_z decreases the net electric field is a mixture of sine and cosine shapes as shown in figure 4.2b and 4.2c. Only when the amplitude of ∇T_z becomes 3 orders of magnitude smaller, the net electric field returns to a well-defined sinusoidal waveform as shown in figure 4.2d.

These calculations show that by performing angle dependent measurements of the magnetization the presence of unwanted thermal gradient ∇T_z can be detected in the
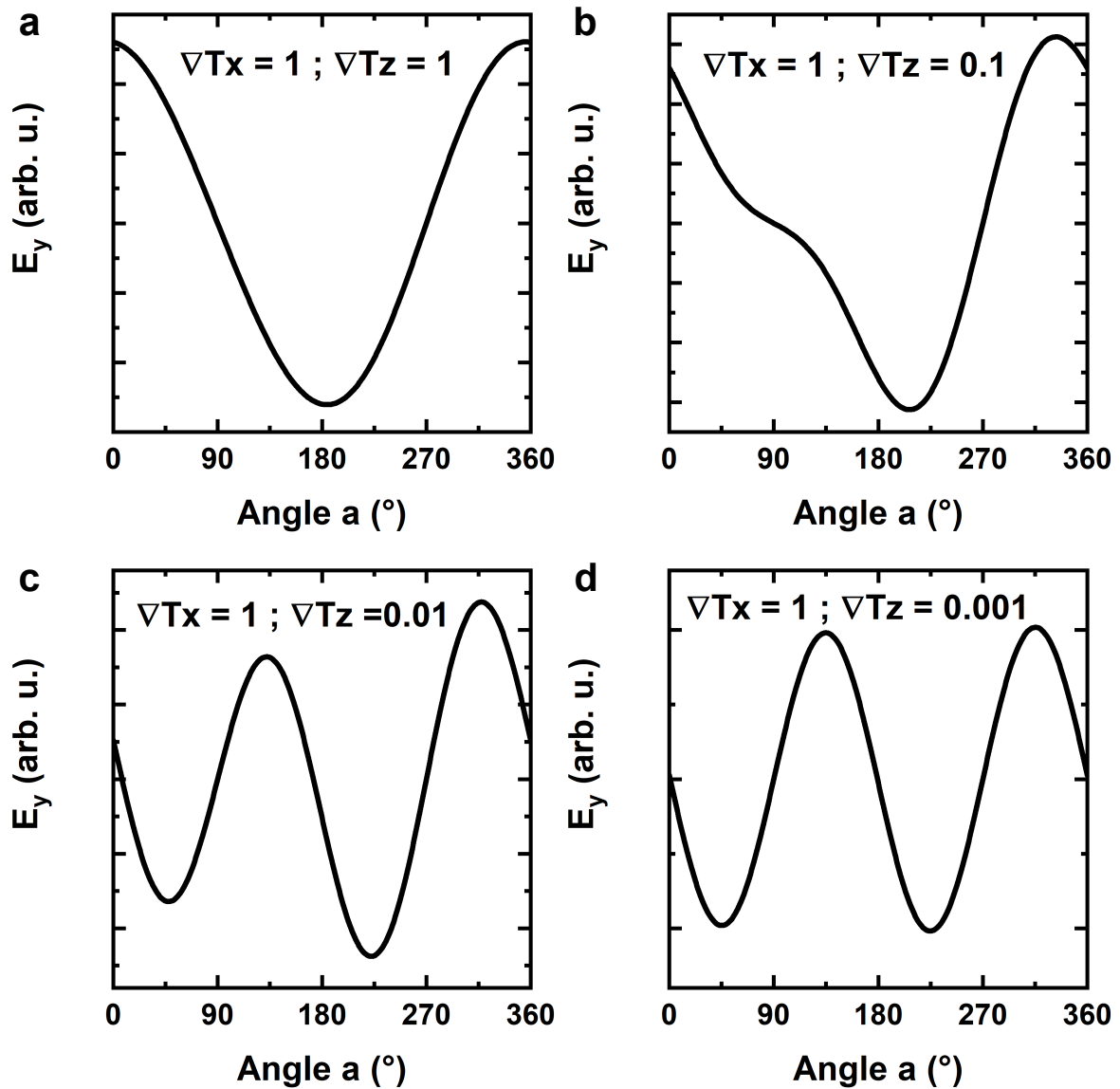
Figure 4.2. – Calculated output of the electric field using equation 4.2 for different thermal gradient amplitudes between ∇T_x and ∇T_z. The magnetization was assumed to rotate in the direction of the angle a. The values for the thermoelectric coefficients were assumed from the literature (see text). **a**, both thermal gradients have the same amplitude. **b**, ∇T_z is 10 times smaller. **c**, ∇T_z is 100 times smaller. **d**, ∇T_z is 1000 times smaller.

total signal. But still its magnitude cannot be inferred. This is a common feature when only a single heater is used in a device configuration as the one shown in figure 4.1. To overcome this artifact, in this work a new procedure is introduced in section 4.2, that uses a second heater to produce a different direction of the thermal gradient and allows to separate unwanted contributions to the total measured signal.

4.2. Two-heater procedure: general aspects

In this section the "two-heater" procedure is introduced. A second heater is added in in the device scheme in figure 4.1. This introduces a possibility to generate a thermal gradient with opposite direction in the x-axis whereas the thermal gradient in the z-axis has the same magnitude. The scheme of the new device configuration is shown in figure 4.3.
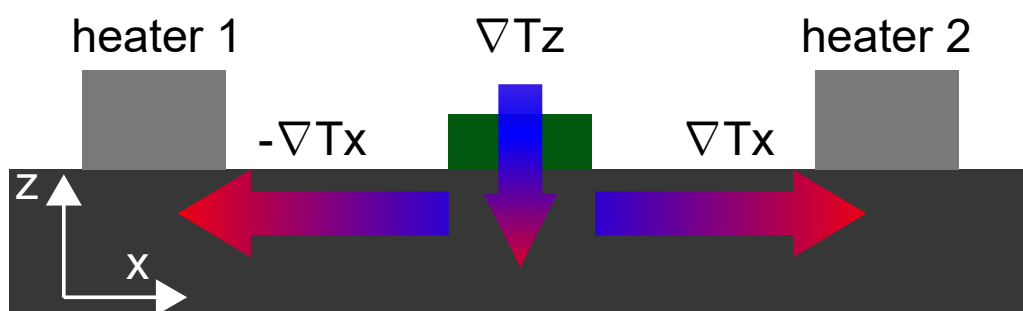
Figure 4.3. – Schematic side view of the device studied. The micro/nanowire in green is located between two identical heaters. If the two heaters produce the same heat and the thermal transport occurs through the substrate there are two possible thermal gradients present in the device when a current is applied to the heaters.

4.2.1. Balanced heaters

Equation 4.1 describes the electric field that is produced by only one heater, in this case heater 2 (H2) from figure 4.3. Here, a second heater is introduced (H1) that by means of Joule heating produces a thermal gradient along the x-axis and z-axis. If both heaters produce the same amplitude of the thermal gradient, the resulting net

electric field for both heaters can be se separately described by equation 4.1, but with opposite signs of ∇T_x:

$$
\begin{aligned}
E_{\text{H1}} = \left(S_\parallel - S_\perp \right) &\left[-\nabla T_x \sin^2\left(b \right) \sin\left(a \right) \cos\left(a \right) + \nabla T_z \sin\left(b \right) \cos\left(b \right) \sin\left(a \right) \right] \\
- S_{\text{N}} &\left[-\nabla T_x \cos\left(b \right) - \nabla T_z \sin\left(b \right) \cos\left(a \right) \right]
\end{aligned}
\tag{4.3}
$$

$$
\begin{aligned}
E_{\text{H2}} = \left(S_\parallel - S_\perp \right) &\left[\nabla T_x \sin^2\left(b \right) \sin\left(a \right) \cos\left(a \right) + \nabla T_z \sin\left(b \right) \cos\left(b \right) \sin\left(a \right) \right] \\
- S_{\text{N}} &\left[\nabla T_x \cos\left(b \right) - \nabla T_z \sin\left(b \right) \cos\left(a \right) \right]
\end{aligned}
\tag{4.4}
$$

where E_{H1} and E_{H2} are the resulting electric fields for H1 and H2 respectively. For the method described here it is essential to note that ∇T_z does not change upon sign reversal of ∇T_x, since independently from which side the thermal gradient is generated the amplitude/direction of ∇T_z is the same. This can be utilized by adding or subtracting measurements performed independently with each heater, which can be described by adding or subtracting equations 4.3 and 4.4, giving $E_{\text{H1,H2 ; sum}}$ and $E_{\text{H1,H2 ; diff}}$, respectively:

$$
\begin{aligned}
E_{\text{H1,H2 ; sum}} &= E_{\text{H1}} + E_{\text{H2}} \\
&= 2 \left(S_\parallel - S_\perp \right) \nabla T_z \sin\left(b \right) \cos\left(b \right) \sin\left(a \right) \\
&+ 2 S_{\text{N}} \nabla T_z \sin\left(b \right) \cos\left(a \right)
\end{aligned}
\tag{4.5}
$$

$$
\begin{aligned}
E_{\text{H1,H2 ; diff}} &= E_{\text{H1}} - E_{\text{H2}} \\
&= -2 \left(S_\parallel - S_\perp \right) \nabla T_x \sin^2\left(b \right) \sin\left(a \right) \cos\left(a \right) \\
&+ 2 S_{\text{N}} \nabla T_x \cos\left(b \right)
\end{aligned}
\tag{4.6}
$$

these two equations in a net electric field that depends either on ∇T_z or ∇T_x. The factor 2 that appears in the equations arises since the amplitudes of the thermal gradient in the same direction add up for both cases.

Equation 4.5 and equation 4.6 can be simplified by assuming that the magnetization can only rotate in-plane ($b = 90°$), obtaining:

$$E_{\text{H1,H2}\,;\,\text{sum}\,;\,\text{in}-\text{plane}} = 2S_{\text{N}}\nabla T_z \cos{(\text{a})} \tag{4.7}$$

$$E_{\text{H1,H2}\,;\,\text{diff}\,;\,\text{in}-\text{plane}} = -2\left(S_{\parallel} - S_{\perp}\right)\nabla T_x \sin{(\text{a})}\cos{(\text{a})} \tag{4.8}$$

Here again the net electric field depends either on ∇T_x or ∇T_z. Assuming a magnetization that is only oriented in the out-of-plane direction ($b = 0°$), on the other hand the equations 4.5 and 4.6 can be simplified to:

$$E_{\text{H1,H2}\,;\,\text{sum}\,;\,\text{out}-\text{of}-\text{plane}} = 0 \tag{4.9}$$

$$E_{\text{H1,H2}\,;\,\text{diff}\,;\,\text{out}-\text{of}-\text{plane}} = 2S_{\text{N}}\nabla T_x \tag{4.10}$$

In this case, ∇T_z is not present in both equations.

Using equations 4.7 and 4.10 a ratio between ∇T_x and ∇T_z can be inferred by following:

$$\Gamma = \frac{E_{\text{H1,H2}\,;\,\text{sum}\,;\,\text{in}-\text{plane}}}{E_{\text{H1,H2}\,;\,\text{diff}\,;\,\text{out}-\text{of}-\text{plane}}} = \frac{2S_{\text{N}}\nabla T_z \cos{(\text{a})}}{2S_{\text{N}}\nabla T_x} \tag{4.11}$$

For the magnetization pointing in the x-direction ($\cos{(\text{a})} = 1°$), Γ gives the strength of ∇T_z in units of ∇T_x.

The results presented in this section show that by introducing a second heater (H1 in figure 4.3) to the device configuration of figure 4.1 and obtaining the net electric field from the thermoelectric equations from chapter 2 section 2.4.2 for each heater separately, and then by adding or subtracting the equations of the net electric field afterwards, the total net electric field only depends on one of component of the thermal gradient ∇T_x or ∇T_z. This confronts directly the problem that was shown and discussed in section 4.1 where ∇T_z (the unwanted thermal gradient) affected the signal. Now with the "two-heater" procedure the measured signal can be separated in one signal that depends only on one component of the thermal gradient and not at combination of the contribution of ∇T_x and ∇T_z. Furthermore, the unwanted gradient can be

quantified since Γ gives the strength of ∇T_z that is unavoidably connected with any value of the desired gradient ∇T_x that is generated by the heater.

4.2.2. Unbalanced heaters

Up to now in equations 4.5 to 4.10 it was assumed that the amplitude of the thermal gradient produced by both heaters was the same, i.e. that the heaters are balanced. In practice however this is not the case a priori and calibrations of the heaters need to be performed. In this section the case is discussed when the two heaters produce a different amplitude of the thermal gradient, i.e. the heaters are unbalanced, and the consequences in the "two-heater" procedure.

For simplicity a magnetization that rotates in-plane ($b = 90°$) is assumed in further analysis. For unbalanced heaters, the equations 4.7 and 4.8 are not valid, instead the following equations apply:

$$E_{\text{H1,H2;sum;in-plane}} = \left(S_{\parallel} - S_{\perp}\right)\left(\nabla T_{x\,;\text{H2}} - \nabla T_{x\,;\text{H1}}\right)\sin\left(\text{a}\right)\cos\left(\text{a}\right)$$
$$S_{\text{N}}\left(\nabla T_{z\,;\text{H2}} + \nabla T_{z\,;\text{H1}}\right)\cos\left(\text{a}\right) \tag{4.12}$$

$$E_{\text{H1,H2;diff;in-plane}} = -\left(S_{\parallel} - S_{\perp}\right)\left(\nabla T_{x\,;\text{H2}} + \nabla T_{x\,;\text{H1}}\right)\sin\left(\text{a}\right)\cos\left(\text{a}\right)$$
$$+ S_{\text{N}}\left(\nabla T_{z\,;\text{H1}} - \nabla T_{z\,;\text{H2}}\right)\cos\left(\text{a}\right) \tag{4.13}$$

where $\nabla T_{x\,;\text{H1}}$, $\nabla T_{z\,;\text{H1}}$, $\nabla T_{x\,;\text{H2}}$ and $\nabla T_{z\,;\text{H2}}$ represent ∇T_x and ∇T_z produced by H1 and H2 respectively. To demonstrate the impact of unbalanced heaters, the angular dependency of the net electric field has been calculated for different heater power ratios according to equations 4.12 and 4.13. The results are shown in figure 4.4 and 4.5. In the calculations, the amplitude of the thermal gradient produced by H1 was fixed and the amplitude of H2 was reduced down to 50 % of H1 output. To keep the analysis simple, the ratio between ∇T_x and ∇T_z was set at 1, as it is the case for figure 4.2a.

First, $E_{\text{H1,H2;sum;in-plane}}$ is discussed according to equation 4.12 and the results are shown in figure 4.4. In all the curves the cosine shape is well preserved. But when the amplitude of H2 is reduced relatively to H1, the amplitude of the cosine shape is reduced (magenta line for a reduction of 50 %) in comparison when both heaters are
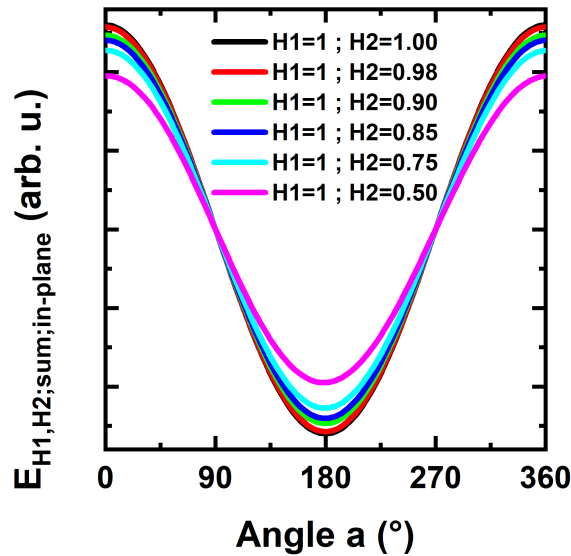
Figure 4.4. – Sum of the net electric field for two unbalanced heaters calculated using equation 4.12. The amplitude of H2 changes relative with respect to H1, whereas the amplitude of H1 stays constant. The ratio between ∇T_x and ∇T_z was set at 1 same as figure 4.2a

balanced (black line). This cosine shape dependency and reduction of amplitude can be explained by analyzing equation 4.12 and the input parameters. The same materials parameters as in section 4.1 for Py were assumed in the calculations ($S_{\mathrm{N}} = -2.6\,\mathrm{\mu V\,K^{-1}}$ and $S_{\parallel} - S_{\perp} = 0.2\,\mathrm{\mu V\,K^{-1}}$). Due to the material parameter values the second term in equation 4.12 is dominant which leads to a cosine shape and would be dominant even for unbalanced heaters. Also, when the heaters are unbalanced the first term in equation 4.12 increases, since $\nabla T_{x\,;\,\mathrm{H2}} - \nabla T_{x\,;\,\mathrm{H1}} \neq 0$. At the same time in the second term, $\nabla T_{z\,;\,\mathrm{H2}} + \nabla T_{z\,;\,\mathrm{H1}}$, becomes smaller since one heater produces less heat than the other. This explains the reduction of the amplitude in the curves, since the second term is dominant and for unbalanced heater this term is reduced.

Now $E_{\mathrm{H1,H2}\,;\,\mathrm{diff}\,;\,\mathrm{in-plane}}$ is discussed according to equation 4.13 and the results are shown in figure 4.5. When the two heaters are balanced the expected behavior of equation 4.8 is obtained (figure 4.4a). Notable deviations appear already if the H2 is reduced by 2 % compared to H1. Significant deviations from equation 4.8 can be observed (figure 4.4b if the difference between the two heaters increases further (figures 4.4c-f). The signal becomes more and more distorted until a point where a pseudo cosine shaped curve is obtained (figure 4.4f). Similar as the analysis made for $E_{\mathrm{H1,H2}\,;\,\mathrm{sum}\,;\,\mathrm{in-plane}}$, the results can be explained by analyzing equation 4.13. When the amplitude of H2 is reduced

73
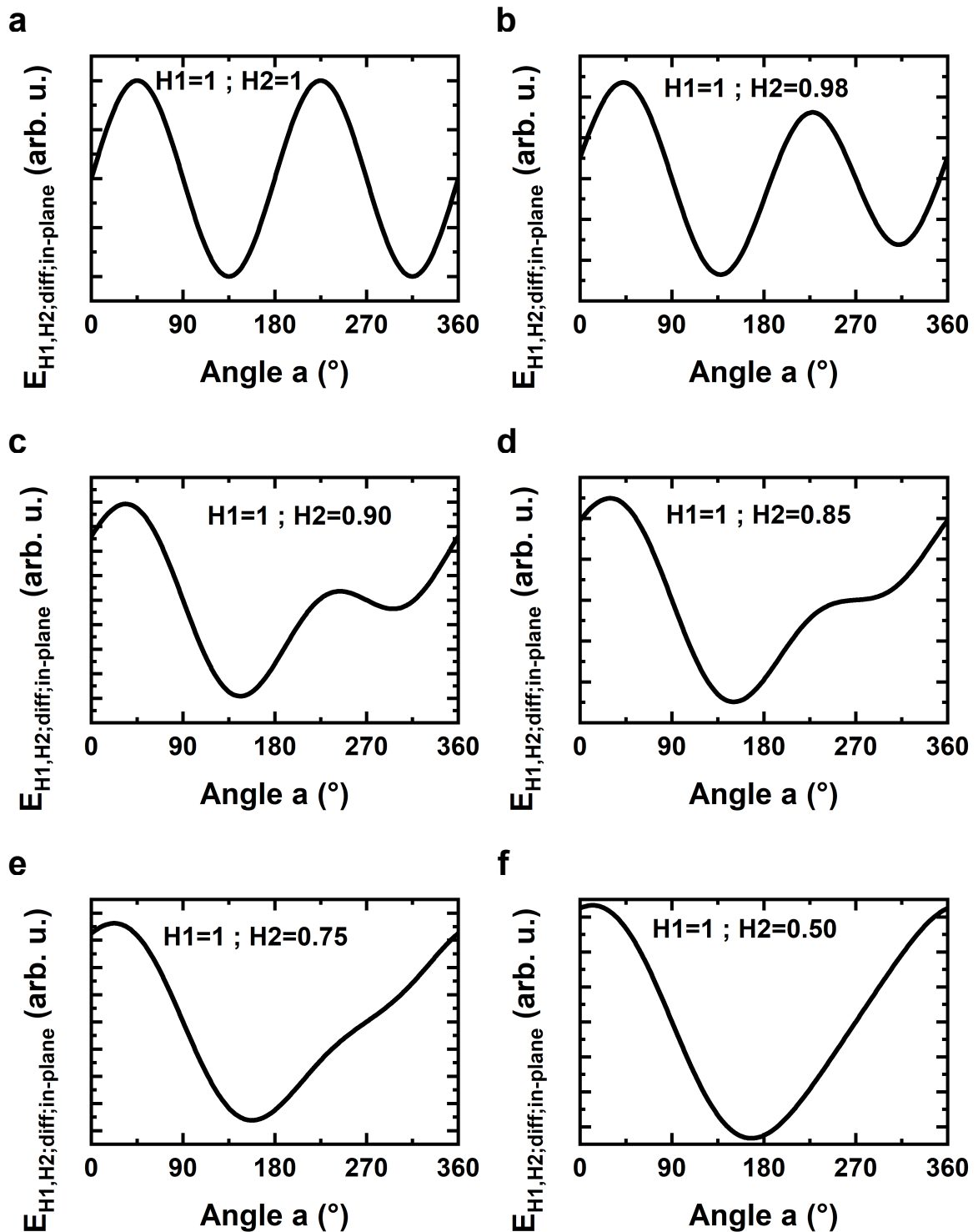
Figure 4.5. – Difference of the net electric field for two unbalanced heaters calculated using equation 4.13. **a** - **f**, the amplitude of H2 changes relatively with respect to H1, whereas the amplitude of H1 stays constant. The ratio between ∇T_x and ∇T_z was set at 1 same as figure 4.2a.

relatively to H1 the second term in equation 4.13 increases since $\nabla T_{z\,;\,\mathrm{H1}} - \nabla T_{z\,;\,\mathrm{H2}} \neq 0$ and this results compete between the two terms in equation 4.13. This explains the distortion of the signal when the two heaters are unbalanced and the tendency towards the cosine shape dependency since the second term in equation 4.13 is dominant as was already discussed above.

In this section it was pointed out that it is of crucial importance for the "two-heater" procedure to work properly that the two heaters are balanced, so that they produce the same thermal gradient in amplitude. Otherwise the net electric field that results by performing the procedure would acquire other artifacts that arise not from only from ∇T_x and ∇T_z, but a mixture from the thermal gradients and the imbalance from the heaters.

4.3. Using the "two-heater" procedure in Py devices

In section 4.2.1 the "two-heater" methodology was described in which the total net electric field only depends on one of component of the thermal gradient ∇T_x or ∇T_z using a two-heater device geometry. In this section this procedure is experimentally tested. In figure 4.6 the device under test with the same geometry described in figure 4.3 is shown. This device was fabricated according to the fabrication procedure described in chapter 3 section 3.1. The heater that is on the left side of the nanowire in the SEM picture was defined as heater 1 (H1) and the heater on the right as heater 2 (H2). The heaters are 30 µm long, 200 nm width and 100 nm thick and are separated from the center of the nanowire by 1 µm. The nanowire itself is 20 µm long, 500 nm wide and consist of a 25 nm thick Py layer with a 2 nm capping layer of platinum.

The device was initially characterized by performing magnetoresistance measurements of the nanowire to characterize the $M_{(H)}$ behavior. This is necessary, since the magnetization enters in the equations discussed in section 4.2, but the magnetic field H parameter can be controlled in the experiments. The resistance was measured in 2-wire geometry since in the device the nanowire has only two connections. Figure 4.7 shows the magnetoresistance measurements. In the measurements a current of 150 µA was applied to the nanowire and the ambient temperature was 21 K. Figure 4.7a shows the dependence of the resistance when an external magnetic field in the x-direction is applied to the nanowire (see figure 4.6b for the coordinate system). Around zero field the resistance shows a peak. Here the magnetization is oriented mainly along the current
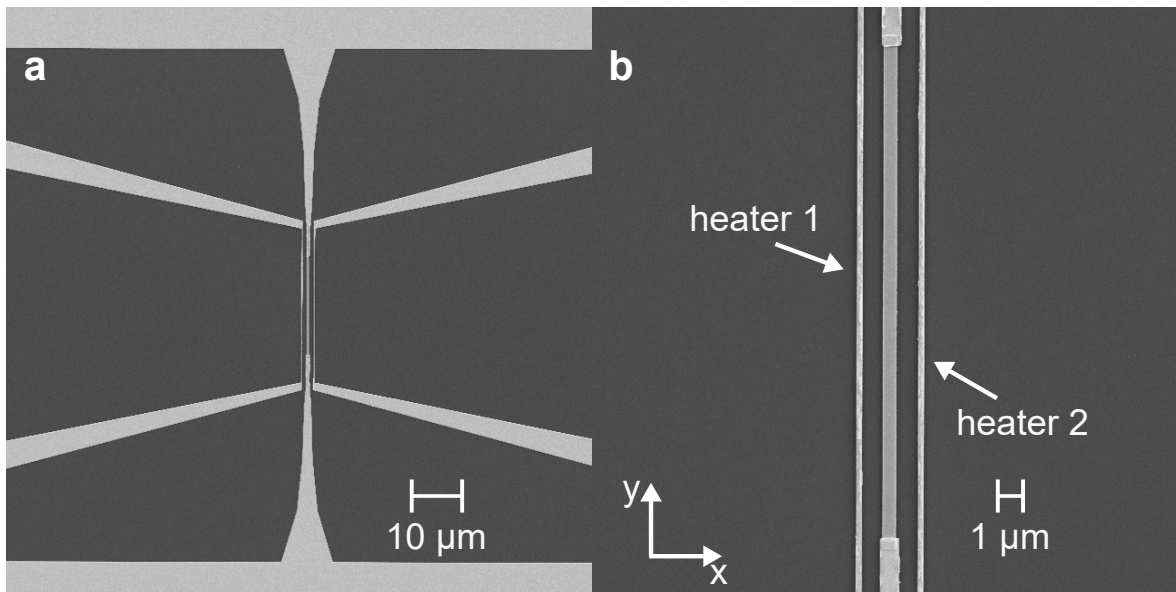
Figure 4.6. – SEM picture of the device under test. **a**, an overview of the complete device. The surface/pads that can be observed are used to connect the device by means of bonding to a chip carrier. **b**, a zoom in to the device. The nanowire is positioned in the middle and parallel to it are the two heater lines.

direction (wire length axis) due to shape anisotropy leading to a high AMR. In this measurement it was observed that above 200 mT the resistance is reduced and stays constant, meaning that the magnetization is saturated and pointing in the direction of the external applied magnetic field perpendicular to the current leading to a low AMR. With this knowledge the measurement of figure 4.7b was performed, where an external magnetic field with an amplitude of 600 mT was rotated in the x-y plane for different angles (this angle can be compared to angle a in section 4.2.1), with 0° the direction of the x-axis and 90° the direction of the y-axis. The measured curve shows the expected [118] angular dependency for anisotropic magnetoresistance as explained in chapter 2 section 2.4.1. In a second measurement, the magnetic field was applied out-of-plane (z axis) and the results are shown in figure 4.7c. Here the amplitude of the field, to reach the saturation of the magnetization, needs to exceed 1.2 T which is 6 times higher than the amplitude needed to saturate the magnetization in-plane.

The magnetoresistance measurements show that the magnetization in the device follows the external field, if sufficiently high magnetic fields are applied. Based on this knowledge, angle dependent thermoelectric measurements could be performed. The thermoelectric measurements were performed following the measurement procedure
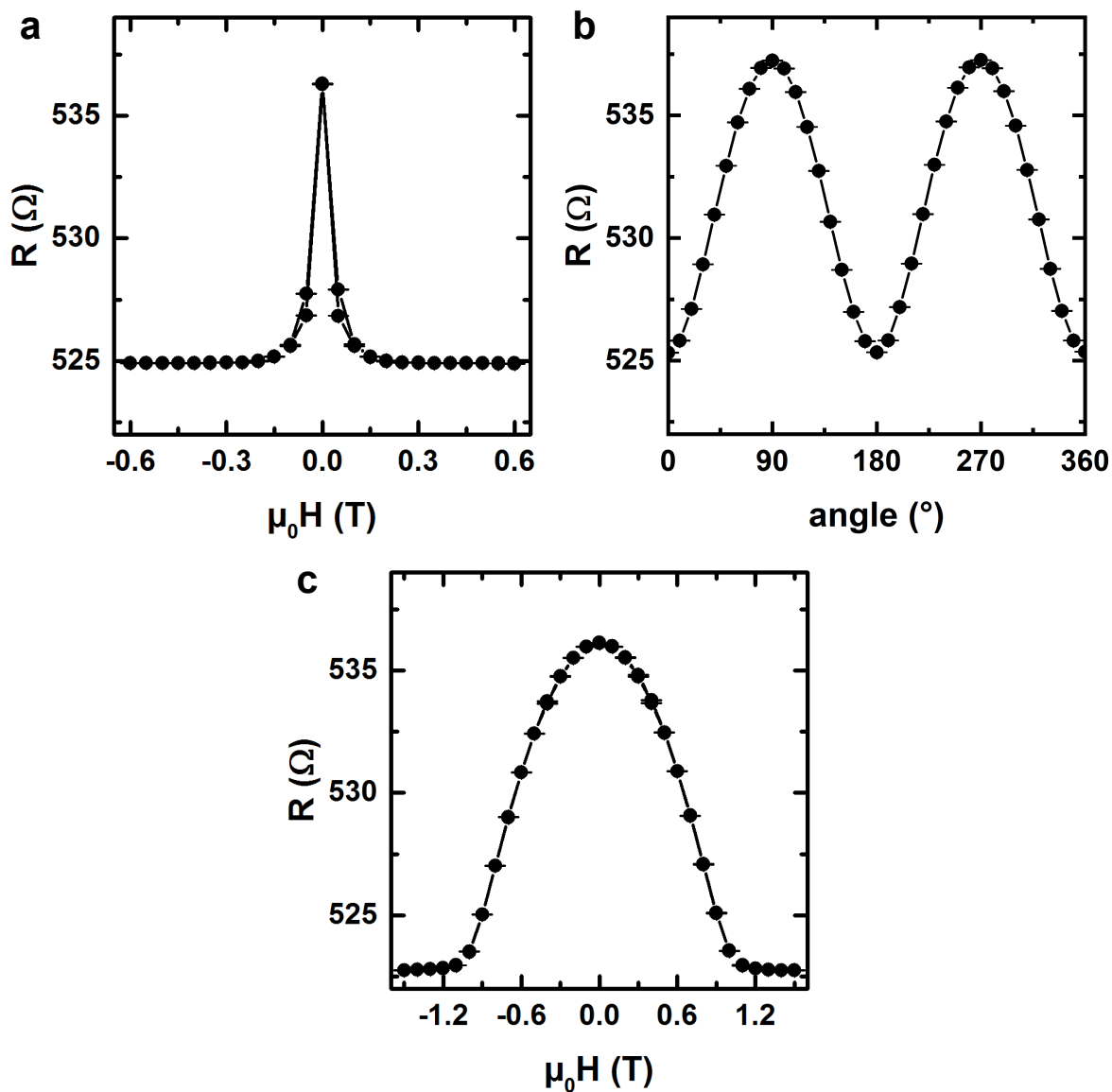
Figure 4.7. – Magnetoresistance measurements of the Py device at an ambient temperature of 21 K. **a**, in-plane magnetoresistance hysteresis loop when the magnetic field is applied along the x axis. **b**, magnetoresistance measurement when a magnetic field with an amplitude of 600 mT was rotated in the x-y plane. In this measurement 0° correspond to the direction along the x axis and 90° in the direction in the y axis. **c**, out-of-plane magnetoresistance hysteresis loop when the magnetic field is applied along the z axis.

that was described in chapter 3 section 3.2.1. In this set of measurements, the same current with a value of 3.2 mA was applied to both heaters. The results are shown in figure 4.8, displaying the thermovoltage response (V_{thermo}) when a magnetic field is applied out-of-plane (figure 4.8a) and when a magnetic field with an amplitude of 1 T was rotated in the x-y plane (figure 4.8b), respectively. It corresponds to the magnetoresistance measurements shown in figure 4.7c and figure 4.7b, respectively. If the magnetic field is applied out-of-plane, as shown in figure 4.8a, independently of which heater generates the thermal gradient, V_{thermo} becomes constant at a value above a magnetic field of approximately 1 T, which is in good agreement with the magnetic field obtained from the magnetoresistance measurements. Also, it can be observed that the two measurements (heater 1 and heater 2) are mirrored, which reflects the reversed direction of the x-gradient. However, the amplitude of V_{thermo} with the applied magnetic field differs depending on the heater that is generating the thermal gradient (H1: $V_{\text{max}} = 5.1$ µV, H2: $V_{\text{max}} = 4.1$ µV). The same behavior is also observed in the measurements shown in figure 4.8b, where the magnetic field is rotated in the x-y plane with a constant amplitude, here $V_{\text{max}} = 3.2$ µV for H1 and $V_{\text{max}} = 2.6$ µV for H2. Also, in figure 4.8b the measurements for the two heaters are mirrored. and the dependency on the angle of the applied field shows the expected behavior as described in the equation 4.2.

The different amplitudes of the thermoelectric effect measured with H1 or H2 can be explained by a difference in the heat produced by the two heaters even as the same current is applied. This difference in heat results in a difference of the nanowire temperature depending on the heater, and therefore a difference in the amplitude of the thermal gradients. The reason for this difference can have different origins such as slightly different shapes of the two heaters, the separation between the nanowire and the heaters being different on each side, or the difference in the resistance of the two heaters being in this case approximately 1 %. However, for the "two-heater" procedure, it is important that the heaters are balanced, because even small differences could lead to significant artifacts in the sum/difference-signals of this procedure as shown in figure 4.4 and figure 4.5. Therefore, the heaters need to be calibrated before the thermoelectric measurements are performed.

The calibration of the heaters can be performed according to two different procedures, calibrate the temperature of the nanowire or calibrate the amplitude of thermal gradient. By calibrating the temperature of the nanowire, it is assumed that the heat path is the same independent of the heater and thus the thermal gradients, which may be not
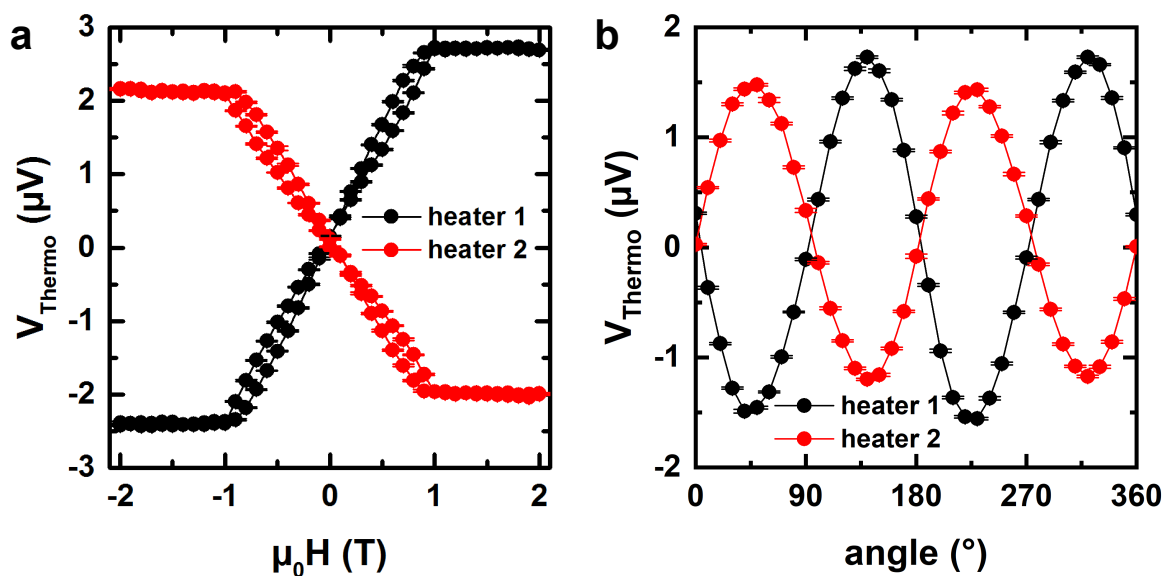
Figure 4.8. – Thermovoltage measurements of the Py device when the same current value is applied to the heaters. The current that was applied had a value of 3.2 mA and the ambient temperature was 4 K. Both measurements of heater 1 and heater 2 were performed independently. **a**, the magnetic field is applied out-of-plane. **b**, the magnetic field with an amplitude of 1 T was rotated in the x-y plane.

the case. In contrast, calibrating the amplitude of the thermal gradient directly is more reliable since structural effects (i.e. landscape of the substrate) would be taken in-to account. To calibrate the temperature of the nanowire, the resistance increase of the nanowire needs to be measured when the nanowire experiences the heat produced by one of the heaters. This procedure uses the fact that in metallic materials like Py the resistance increases as the temperature increases. Therefore, if both heaters produce the same temperature increase in the nanowire, then by measuring the resistance of the nanowire independently from which side the heat is produced the resistance value of the nanowire should match.

To quantify the thermal gradient the thermoelectric voltage measurements when the magnetization is pointing completely out-of-plane can be used. This is because equation 4.10 shows that when the magnetization is out-of-plane, the thermovoltage should only depend on two parameters, the Nernst coefficient and ∇T_x. Thus, if the amplitudes of the thermal gradients generated with both heaters are equal, the measured thermovoltages should coincide independently of the current value that is applied to the heater (I_{heater}). If the magnetic field is swept from the positive to the negative direc-

79
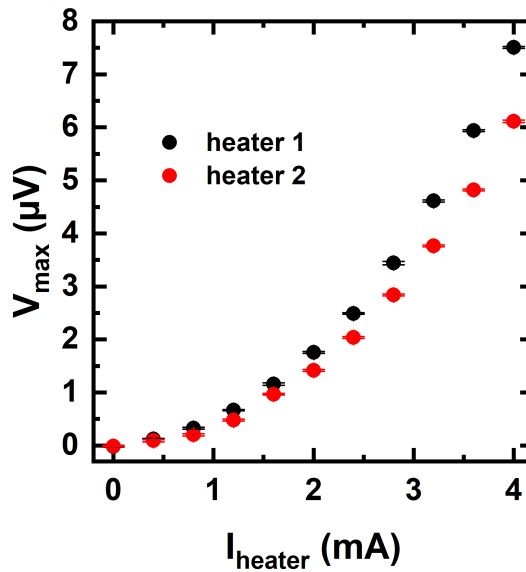
Figure 4.9. – Heater calibration. The amplitude value of the thermoelectric effect V_{max} as a function of the current applied to the heaters I_{heater} for an ambient temperature of 21 K. V_{max} is obtained by changing the magnetic field from +2 T to -2 T at a fixed I_{heater}. The measurements of the two heaters where performed independently of each other.

tion, the thermovoltage can be calculated as the addition of the amplitudes measured for both directions (V_{max}). Hereby magnetic field independent offsets, as generated e.g. by thermovoltages in the contacts and the wiring, are removed. If the such obtained V_{max} is the same when heating with either of the heaters, then the thermal gradient that both produce is equivalent.

In this work, for the heater calibration, the second procedure was followed, the direct calibration of the thermal gradients. Before starting the calibration one important annealing process of the heaters needed to be performed. The reason is that the current values that are applied correspond to a current density of in the order of $2x10^{11}\ \mathrm{A\,m^{-2}}$, and this results in modifications in the internal structure of the heaters (due to the temperature increase). Therefore, before the calibration process started, a current of $I_{heater} = 4.3$ mA was applied to the heaters for a period of 24 hours. The reason why $I_{heater} = 4.3$ mA was chosen, is that for the calibration process a maximal $I_{heater} = 4$ mA was applied. This ensures that no further modification to the heaters is expected since a lower I_{heater} value was used in the measurements as for the annealing process of the heaters.

In the calibration process, first one of the heaters was chosen to generate the temperature gradient for a given I_{heater} value, and the thermovoltage was measured at the nanowire for magnetic fields with magnitude of ± 2 T applied in the out-of-plane direction. For both fields the thermovoltage was recorded and the values were subtracted for offset correction. This process was then repeated for different I_{heater} values and for the other heater. The results are summarized in figure 4.9, where the ambient temperature was set to 21 K. V_{max} is found to scale quadratically with I_{heater}, i.e. with the amplitude of the thermal gradient, as expected for thermoelectric effects. Also, similar as in figure 4.8, it is observed that by applying the same value of I_{heater} H2 shows a lower V_{max} value in comparison to H1.

By performing this heater calibration, the expected V_{max} value is known for a specific I_{heater} current that is applied to either one of the heaters. With this knowledge, I_{heater} values that balance the heaters to generate he same thermal gradient and thus the same V_{max} can be calculated: For instance, for an amplitude of $V_{max} = 4$ µV a current of $I_{H1} = 2.97$ mA needs to be applied to H1 and for H2 a current of $I_{H2} = 3.28$ mA. This information can be used to reproduce the thermoelectric measurements presented in figure 4.8, but this time the resulting V_{max} produced from both heaters should coincide. The results for balanced heaters are shown in figure 4.10a for the measurements where the magnetic field is applied out-of-plane and in figure 4.11a where the magnetic field with an amplitude of 1 T was rotated in the x-y plane. It can be observed that for the two measurements V_{max} is equivalent when the thermal gradient is generated from H1 or H2. The expected amplitude value of in the out-of-plane measurements of figure 4.10a should be $V_{max} = 4$ µV, as was calculated form the calibration measurements. This value is in fact obtained from the measurements using the calculated I_{heater} currents that need to be applied to reach this value. In the measurements of figure 4.11a a value of $V_{max} \approx 2.6$ µV is obtained. Another important feature, which was already discussed, is that the measurements from figure 4.10a and 4.11a show that the shapes of the curves are independent of the used heater.

The measurement results for both heaters as shown in figure 4.10a and 4.11a show that both heaters are well balanced. Thus the "two-heater" procedure represented by equations 4.7 to 4.10 can be now be exploited to extract information on the magnetic structure of the experimental system. If the thermovoltage data for heater 1 and heater 2 in figure 4.10a are added then, according to equation 4.9 the result should be zero, but in this case is not. The result of this addition is showed in figure 4.10b. The thermovoltage does not show a dependency on the applied magnetic field, but rather a
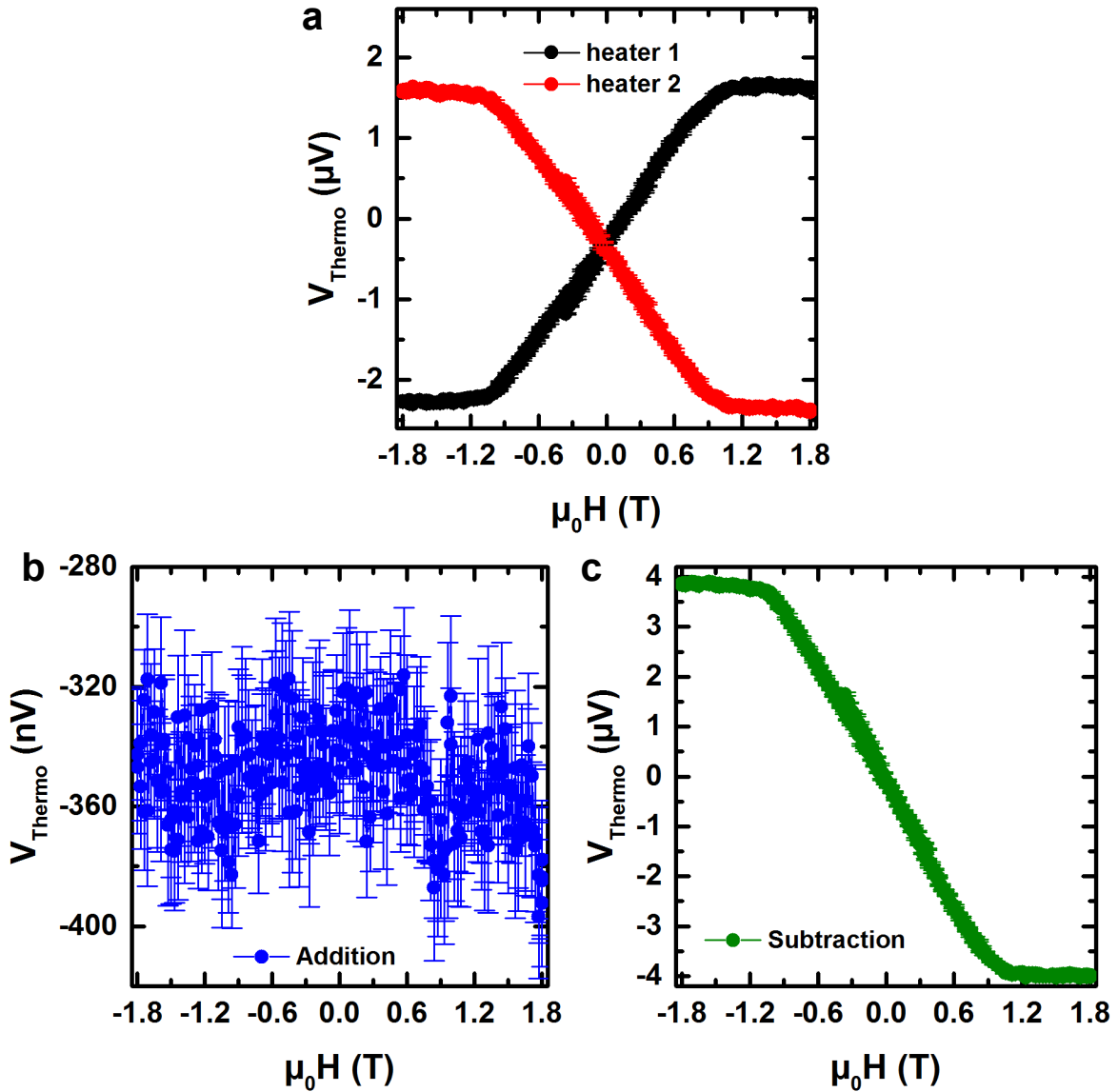
Figure 4.10. – Out-of-plane thermovoltage measurements and analysis when the amplitude of the thermal gradient produced from the two heaters is the same. The ambient temperature was set for 21 K for the measurements. **a**, out-of-plane thermovoltage measurements when $I_{H1} = 2.97$ mA and $I_{H2} = 3.28$ mA. **b**, the resulting data when the signal obtained from heater 1 and heater 2 in a is added. **c**, the resulting data when the signal obtained from heater 1 and heater 2 in a is subtracted.

noise like behavior. If an average is taken across the data points, a value of ≈ -350 nV is obtained. The absence of a field dependency shows that the origin of the sum signal is not a magnetization change in the nanowire but rather a thermovoltage contribution from the contacts or leads that are present in our experimental setup, as also detected in similar investigations [119, 120].

If the thermovoltage data from the two heaters is subtracted following equation 4.10, the resulted subtracted values should scale with the applied magnetic field in the same manner as the measurements performed without the subtraction. The only difference is that the amplitude of the thermoelectric signal should double. In fact, such a behavior is obtained as shown in figure 4.10c, where the same dependency of the signal with the magnetic field as in figure 4.10a is obtained but with double the amplitude of the thermoelectric signal, 8 µV instead of 4 µV. Also, it can be seen by comparing the measurements before and after the subtraction that the signal obtained after the subtraction is symmetric, this mean that for negative as for positive fields the same thermovoltage is obtained, which was not the case for the measurements of figure 4.10a. One reason for this could be that the subtraction of the two signals removes field independent offsets that arise from the contacts. The removal of field independent artifacts is a positive side effect of the difference signal analysis.

The same analysis can be also performed on the in-plane measurements of figure 4.11a where the magnetic field was rotated in the x-y plane with a fixed amplitude of 600 mT. If the two signals are added, following equation 4.7, the sum signal should have a cosine dependency and a dependency with ∇T_z. The experimental data after the addition shows exactly this cosine-like behavior as can be seen in figure 4.11b. Also, the amplitude of the sum signal is quite small in comparison to the measured thermovoltage data (figure 4.11a). Through this chapter it was already discussed that the Nernst coefficient in Py is higher than the difference of the Seebeck coefficients.

The sum signal also depends on the Nernst coefficient (equation 4.7) but nevertheless the signal has a lower amplitude compared to the measured thermovoltage in figure 4.11a. The only explanation that can be assumed is that ∇T_z needs to be at least one order of magnitude smaller than ∇T_x to obtain the measured values in figure 4.11a and in 4.11b. This confirms that for this device geometry ∇T_x has a higher amplitude than ∇T_z. An estimation of the ratio between ∇T_x and ∇T_z is explained below.

Notice that the sum signal also has an offset of approximately ≈ -700 nV compared to the expected cosine behavior. This offset is two times the offset obtained from the
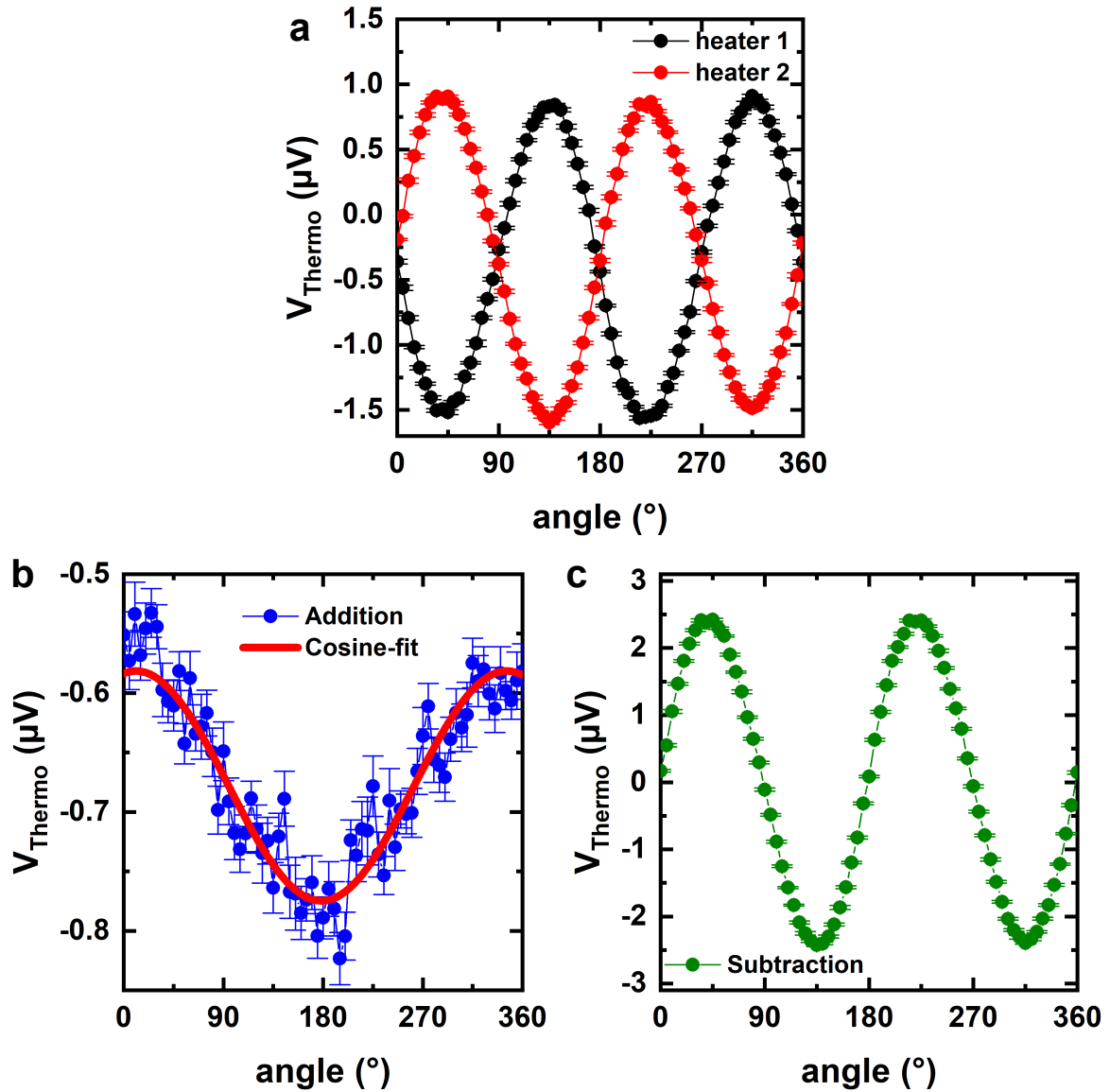
Figure 4.11. – Thermovoltage measurements and analysis by sweeping in the x-y plane the magnetic field with a fixed amplitude when the heaters are balanced. The amplitude of the magnetic field was 1 T and the ambient temperature was set to 21 K. **a**, thermovoltage measurements when $I_{H1} = 2.97$ mA and $I_{H2} = 3.28$ mA. **b**, the resulting data when the signal obtained from H1 and H2 in a is added. The red line represents a cosine fit through the data points. **c**, the resulting data when the signal obtained from H1 and H2 in a is subtracted.

measurements in figure 4.10b (≈ -350 nV). This factor can be explained since the two thermovoltage signals are added up, which again leads to an offset arising from contact related artifacts, as discussed above.

In equation 4.8, the thermovoltage depends on ∇T_x, the difference in the Seebeck coefficients and the signal should follow a sine-cosine behavior. The result of the subtraction of the in-plane thermovoltage signals for the two heaters from figure 4.11a is shown in figure 4.11c. The difference data follows the expected behavior as described in equation 4.8, it has a symmetrical sine-cosine dependency on the rotation angle of the magnetic field, thus showing the same thermovoltage for angles with a 90° periodicity. Same as when the magnetic field was applied out-of-plane the amplitude of the thermoelectric signal has doubled reaching a value of 5 µV.

An estimation of the ratio between ∇T_x and ∇T_z can be performed by taking the experimental values obtained in figures 4.10c and 4.11b and equation 4.11. Using $E_{\text{H1,H2;sum;in-plane;max}} \approx 0.1$ µV and $E_{\text{H1,H2;diff;out-of-plane;max}} \approx 4$ µV which are obtained from figures 4.11b and 4.10c respectively, a ratio of $\Gamma \approx 0.025$ is obtained. The obtained value indicates that ∇T_x has a higher amplitude than ∇T_z, which is an expected result due to the device geometry.

From the results and analysis presented in this section it can be concluded that the "two-heater" procedure, using a symmetric two-heater device as presented in figure 4.3 and a nanowire material with a known $M_{(H)}$ behavior as the soft magnetic Permalloy, allows to separate the thermovoltage contributions related to the thermal gradients ∇T_x and ∇T_z. The "two-heater" procedure can be only reliable when the heaters are balanced. The balancing of the heaters was accomplished by performing a calibration procedure introduced in this section, that allows to balance the heaters using the same two-heater device used for the measurements.

5. Thermoelectrical detection of domain wall propagation in (Ga,Mn)(As,P) microwires

In this chapter the measurements on a ferromagnetic semiconductor microwire with perpendicular magnetic anisotropy are discussed. The anomalous Nernst effect (ANE) is used as a tool for the detection of the magnetization reversal and of the propagation of a domain wall (DW) across the microwire. The results of this thermoelectric measuring method are compared to Magneto-optical Kerr effect microscopy. It is shown that using ANE, a DW can be detected which is moving by means of spin torque and magnetic fields and its position along the microwire can be precisely determined.

5.1. (Ga,Mn)(As,P) devices fabrication

The (Ga,Mn)(As,P) devices under investigation were grown by molecular beam epitaxy (MBE) in the group of Richard P. Campion at Nottingham University and were fabricated by standard clean room methods by Zbynek Soban in the group of Jörg Wunderlich at the Academy of Science of the Czech Republic.

The (Ga,Mn)(As,P) microwire, with dimensions of 2 μm wide and 50 μm long was patterned by e-beam lithography along the [110] crystal axis of the Ga0.94Mn0.06As0.91P0.09 epilayer, which was grown by low-temperature molecular beam epitaxy on GaAs substrate and buffer layers (see [121, 122] for more fabrication details). The Curie temperature of the annealed ferromagnetic semiconductor material was 115 K and the conductivity was 230 $\Omega^{-1}\,\mathrm{cm}^{-1}$. In the device, two 200 nm wide platinum (Pt) heater wires with a thickness of 50 nm were fabricated by e-beam lithography and a lift-off procedure at a distance of ± 3 μm to the central (Ga,Mn)(As,P) microwire. After struc-

turing the magnetic microwire and heaters, the structure was coated with a 180 nm PMMA layer on top and high-dose e-beam irradiation was used to define a mask for two 20 µm wide areas, each intersecting the microwire on one of its ends. Subsequently, a 300 nm Cr/Au strip-line was deposited by thermal evaporation on top of each of the mask-free PMMA areas. The strip-lines at both ends of the bar are electrically insulated from the magnetic microwire and were fabricated by lift-off procedure. A colored SEM picture of the fabricated device is shown in figure 5.1.
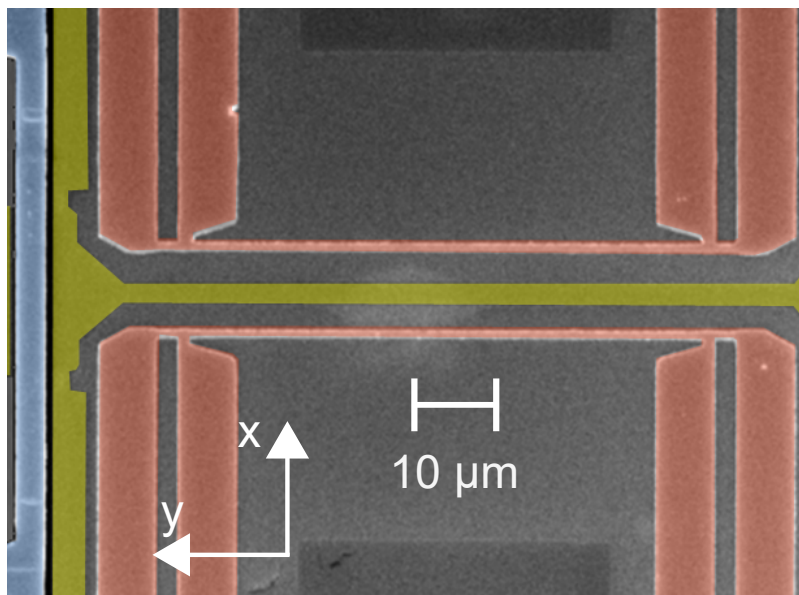
Figure 5.1. – Colored SEM picture of the device fabricated. The middle part (colored in yellow) is the microwire, next to the microwire are the two Pt heaters (in red) and the Cr/Au stripe-line on top of one end of the microwire can be observed (in blue).

5.2. Thermoelectric ANE voltage measurements

In chapter 3 section 3.2 the methodology of the ANE voltage measurements was introduced. For the device described in this chapter the basic methodology of the thermo-electric voltage measurements was slightly changed. This modified measuring procedure is explained next.

To generate the thermal gradient across the nanowire both Pt heaters were used. An alternating electrical current was applied so that the positive half-wave was flowing along one heater while no current was flowing in the other heater. The process was
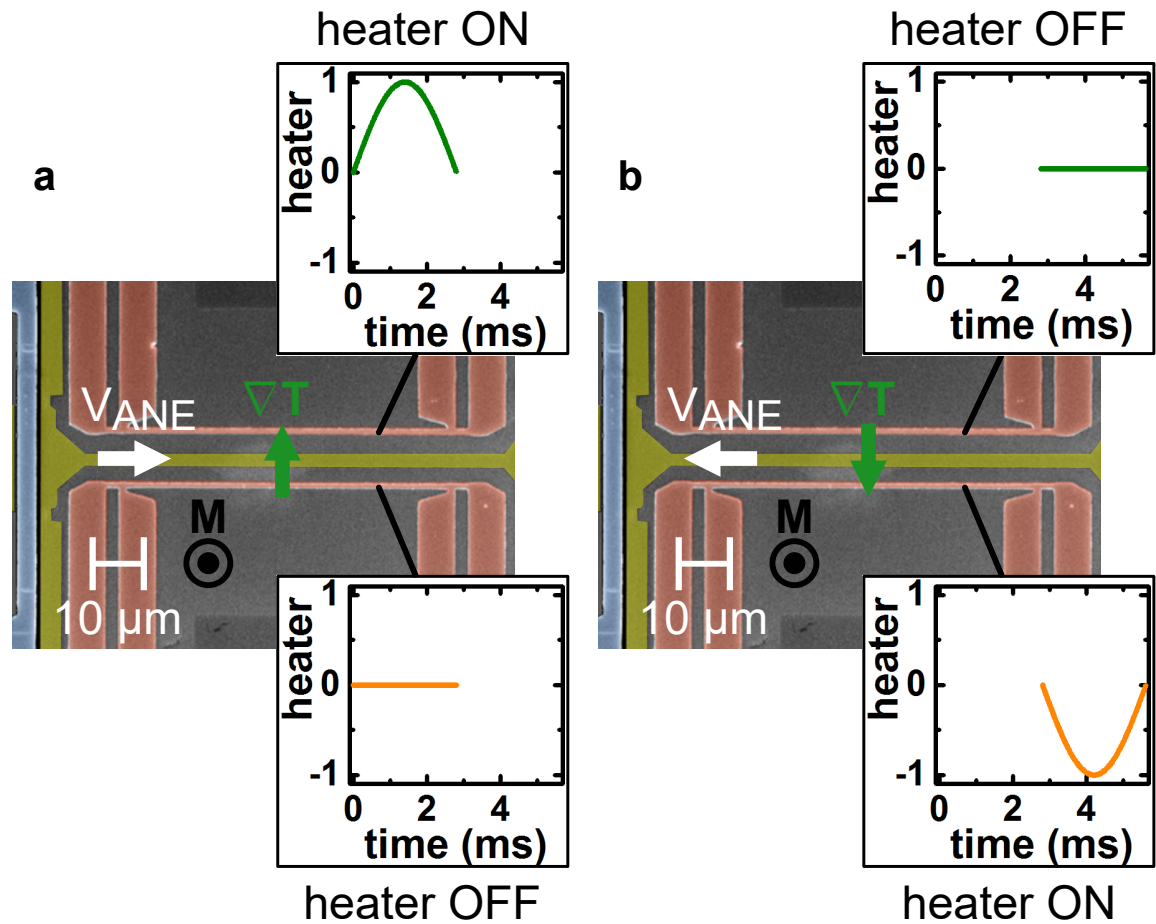
Figure 5.2. – Measurement methodology of the ANE voltage in the GaMnAsP device. **a**, upper heater is on and the bottom heater is off. **b**, bottom heater is on and the upper is off. Notice that depending on where the current is applied the direction of the gradient and the ANE voltage changes.

then reversed so that the negative half-wave of the AC current was applied to the other heater. The alternating process was performed at a certain frequency resulting in an oscillation of the sign of the thermal gradient with the AC frequency. This measuring methodology is described in figure 5.2. By performing such alternating heating, a time-varying temperature gradient across the microwire is generated. The temperature gradient in x-direction oscillates at the same frequency as the frequency of the current that is applied to the heaters (while y and z contributions oscillated at the double frequency). For the detection of the thermoelectric voltage a SR830 lock-in in combination with a SR560 preamplifier was used. The reference signal for the lock-in was supplied by the current source used for the generation of the temperature gradient. Since the generated temperature gradient oscillates with the same frequency as the

89

reference signal and the thermoelectric voltage is proportional to the temperature gradient, the thermoelectric voltage response should also oscillate with the same frequency as the reference signal. Because of this, the thermoelectric voltage detection could be performed at the first harmonic. In contrast, contributions from y and z-direction of the temperature gradient should only appear at the second harmonic, if the heaters are perfectly balanced for all measurements. The frequency of the alternating electrical current (the reference signal) was set to $f = 178$ Hz.

The thermoelectric voltage that is generated by the time-varying temperature gradient can be attributed to the ANE voltage, because the magnetic microwire has a perpendicular magnetic anisotropy [122] and due to the fact, that the measurement technique is only sensitive to thermal gradients in x-direction (see chapter 2 equation 2.46 for more information).

To study the ANE voltage response as a function of an out-of-plane magnetic field, magnetic field hysteresis loops were performed. The results are shown in figure 5.3. Different current amplitudes were tested and for each applied current the average temperature of the microwire was stabilized at 65.5 K. In the measurements the magnetic field was reversed with a step size of 125 µT, this step size is bigger in size in comparison to the measurements performed in section 5.3. The results show rectangular reversal loops with sharp, well defined reversal field H_c. This behavior is typical for a ferromagnetic thin film with strong perpendicular magnetic anisotropy were the nucleation of domains occurs statistically at well-located areas (nucleation sites) across the ferromagnetic film. Under these conditions, after the reversed domain nucleation, a domain wall quickly propagates across the microwire in a uniform manner leading to sharp hysteresis loops [123].

During the ANE voltage measurements depicted in figure 5.3 the average temperature of the microwire increased as the current applied to the heaters increased. To stabilize the temperature of the microwire at a fixed value for each measurement, the cooling power of the cryostat was regulated. The power of the cryostat was regulated by fixing the electrical resistance value of the microwire at a constant value. In the measurements, since the current increased the cooling power of the cryostat was increased.

In figure 5.3 the coercive field H_c changes as the heater current changes showing a higher H_c for higher currents and vice versa. In ferromagnetic materials the magnetization reversal process is governed by two processes, nucleation and propagation [124,125]. The hysteresis loops were performed with the same magnetic field step size for the differ-
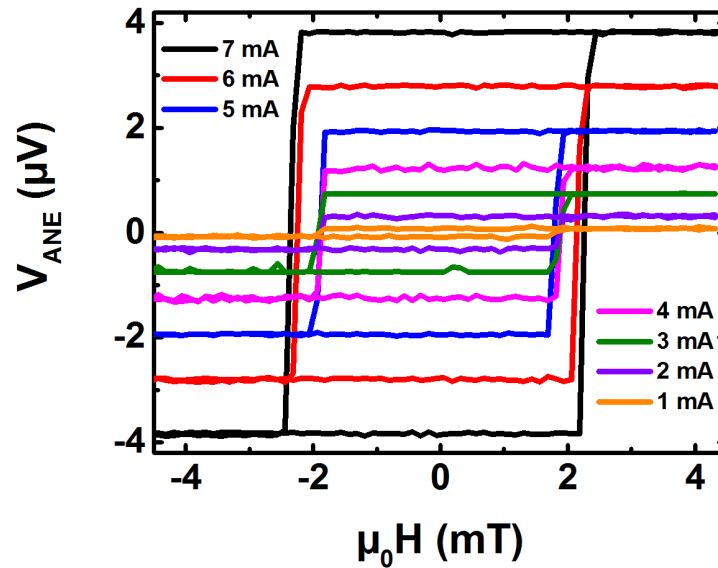
Figure 5.3. – ANE voltage as a function of the applied magnetic field for different heater currents. The resistance of the microwire was kept constant for all measurements.

ent currents applied to the heater, this means that the magnetization reversal process should behave the same in all measurements. Both processes (nucleation and propagation) depend on the temperature. Since the average temperature of the microwire increases as the applied current to the heaters increases, this would affect the magnetization reversal process. In the SEM picture (figure 5.1) the heaters (colored in red) only cover the center part of the microwire (colored in yellow) and the outer part of the microwire is not that affected by the heat produced from the heaters. This means that the outer part of the microwire is at lower temperature and cools down even further as the cooling power of the cryostat decreases. By this, the magnetization reversal process changes from measurement to measurement and with the applied current amplitude. The observed current dependency of the coercive field can be interpreted such that for higher applied currents (and thus lower temperatures of the (Ga,Mn)(As,P) material outside the wire) the nucleation field for nucleating a reversed domains is increased thus leading to an increased coercivity field H_c. In these types of materials (high crystalline quality, high perpendicular magnetic anisotropy), the number of nucleation sites for reversed domains is rather low. So that the process of nucleation of a reversed domain typically occurs inside larger unpatterned areas of the device and not in the relatively small areas such as a microwire [126, 127]. Thus, the magnetization reversal process starts by nucleation at the outer part of microwire which is at a lower temperature

than the center part of the microwire. The statement mentioned above reaffirms and explains the different coercivity magnetic field values at higher heater currents in the measurements performed.

To calibrate the temperature dependence of the microwire the resistance of the microwire was measured as a function of the temperature of the cryostat. Then, from the change of the resistance as a function of the temperature the Curie temperature (T_C) of the microwire was derived by plotting the derivative of the resistance as a function of the temperature [128]. By identifying the maximum value of the derivative the curie temperature is obtained. The microwire resistance as a function of the temperature and its derivative are shown in figure 5.4. From the measurements, a Curie temperature of ≈114 K was determined, which is in the range of the literature values [121].
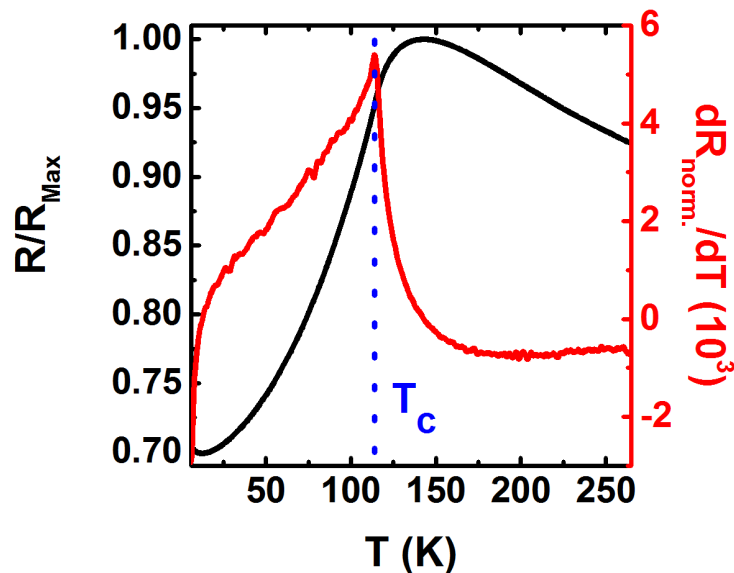
Figure 5.4. – Resistance dependence of the microwire as a function of the cryostat temperature (black line). The derivative is shown as the red line in the graph. The maximal value of the derivative shows the curie temperature of the microwire of T_C ≈114 K.

For the ANE voltage measurements the temperature was fixed at 65.5 K. The importance of fixing the temperature at a certain value was that its temperature would not increase during the heating above the Curie temperature. Also, since the resistance value of the microwire is used to keep track of the temperature and used as a reference when the cooling power of the cryostat was regulated. The temperature needed to be chosen in the range where the resistance had a significant change with the temperature. This is not the case for example for temperatures below 20 K. Another important

point is that the cooling power of the cryostat would be enough to compensate the temperature increase of the heaters. Therefore, the temperature that was chosen for the measurements was 65.5 K, which proved to be the best suitable temperature for the measurements performed in the experiments.

During the ANE voltage measurements the thermal gradient was generated by means of AC joule heating and the frequency used for the current was 178 Hz.

In a second set of experiments, the impact of the AC-current frequency was investigated. Additionally, to the 178 Hz used in the above described experiment, several frequencies ranging from 17 Hz to 262 Hz where tested with respect to their influence on the ANE voltage measurements. In the studied range no substantial difference in the observed ANE voltage was found.
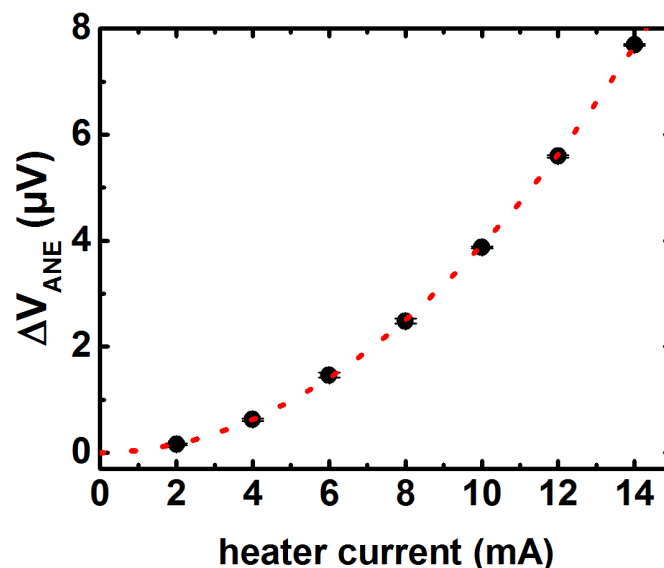
Figure 5.5. – ANE amplitude as a function of the current applied to the heaters. The amplitude of the ANE was calculated from the ANE voltage data showen in figure 5.3. The red dotted line represents a quadratic fit made to the data.

Furthermore, it can be shown that the measured ANE voltage is not a parasitic effect coming from the contacts or some frequency dependency of the measured signal, by studying the amplitude of the ANE as a function of the heater power. The expected dependence should be quadratic with the current applied to the heaters and linear with heater power. To this end, the ANE amplitude was calculated from the measurements shown in figure 5.3. It was calculated by taking the ANE voltage value when the

93

magnetization is saturated in one direction and subtracting it to the ANE voltage value when the magnetization points in the other direction. The difference of these two values, ΔV_{ANE}, gives the ANE amplitude. In figure 5.5 the ANE amplitude ΔV_{ANE} is shown as a function of the heater current. As expected, the ΔV_{ANE} scales quadratic with the current showing that the voltage measured is due to the ANE and no other parasitic effect contributions.

5.3. Magnetic field driven domain wall motion

It is known that a domain wall (DW) propagation can be driven by magnetic fields and depending on the amplitude of the magnetic field the velocity of the DW increases or decreases (see chapter 2 section 2.2.1). In the experiment realized in this thesis, a DW was nucleated in the microwire and propagated by applying a perpendicular magnetic field to the device. The DW was detected by measuring the ANE voltage and the presence of the DW was confirmed with MOKE.

To perform the experiment, a DW needed to be nucleated at a known position in the microwire. This was accomplished by producing a local Oersted field with opposite direction than the magnetization of the microwire. A pulse with an amplitude of 20 mA and a duration of 10 ms then was applied to the Cr/Au stripe-line (see blue stripe in figure 5.1). The result is that locally near of the Cr/Au stripe-line the magnetization in the microwire is locally reversed. This generates a DW at one end of the microwire and leaves the magnetization in other parts of the microwire same as before the pulse.

The ANE voltage measurements and the MOKE measurements were taken separately. For the ANE voltage measurements a current with an amplitude of 4 mA was applied to the heater and the temperature was kept at 65.5 K. The measurements are depicted in figure 5.6 and were performed in the following steps: first the magnetization of the microwire was saturated in the negative direction (out-of-plane) by applying a field of -20 mT, then the magnetic field was reversed in the opposite direction with a magnetic field step size of 0.5 µT until a magnetic field of $\approx$ +0.05 mT was reached. At this magnetic field value, a pulse through the Cr/Au stripe-line was applied with the parameters described above to nucleate a reversed domain. Then the magnetic field was swept until the magnetization reversal of the microwire was completed.

During the procedure mentioned above the ANE voltage was recorded continuously. In

figure 5.6a one typical measurement of the ANE voltage as a function of the magnetic field for this procedure is shown. The ANE voltage was normalized with the criteria that +1 corresponds to the magnetization of the complete wire pointing up and -1 that the magnetization is pointing down. In the measurement the ANE voltage starts at -1 and as the magnetic field is increased the signal shows sharp transitions or plateaus until the ANE voltage reaches +1. The behavior of the signal can be interpreted as a DW propagating through the microwire. The plateaus in the signal show the pinning sites that the domain wall encounters in its path (marked with numbers in figure 5.6a), and the sharp transition indicate the magnetic field necessary to move the DW from one pinning site to the other. The peak observed at the magnetic field value for the nucleation pulse is an artifact induced by the electrical cross-talk of the pulse (marked in figure 5.6a). The ANE measurements allow to calculate the DW position in the microwire from the ANE voltage. Knowing the length of the microwire ($l_{microwire}$) and the ANE voltage for both magnetization directions at saturation ($V_{ANE;saturation}$) a relationship between the measured voltage and the position of the nanowire can be expressed as:

$$DW_{position} = \frac{V_{ANE} \cdot l_{microwire}}{V_{ANE;saturation}} \tag{5.1}$$

with the equation 5.1 the position of the DW can be calculated. Applying this equation for the measurement in figure 5.6a, the position of the DW in the three pinning sites marked can be calculated, obtaining -19 µm, 4 µm and 15 µm respectively. This measuring procedure was repeated several times not showing any difference between the measurements of the pinning site positions.

Before the MOKE measurements are introduced, it is important to mention the difference between the measurements presented in figure 5.3 and the measurements in figure 5.6a. In figure 5.3 the magnetic field is sweep with bigger steps in comparison to the measurements in figure 5.6a (125 µT compared to 0.5 µT). When the magnetic field is above the pinning field the DW does not experiences the presence of the pinning sites, which is the case for the measurements in figure 5.3. As the magnetic field is reduced (the step size) the pinning sites start to influence the movement of the DW, which is the case for the measurements in figure 5.6a (see chapter 2 section 2.2.1 about this topic). This explains why the measurements in figure 5.6a show plateaus in the ANE voltage signal in comparison to the measurements in figure 5.3.

The MOKE measurements were realized with the setup described in chapter 3 section
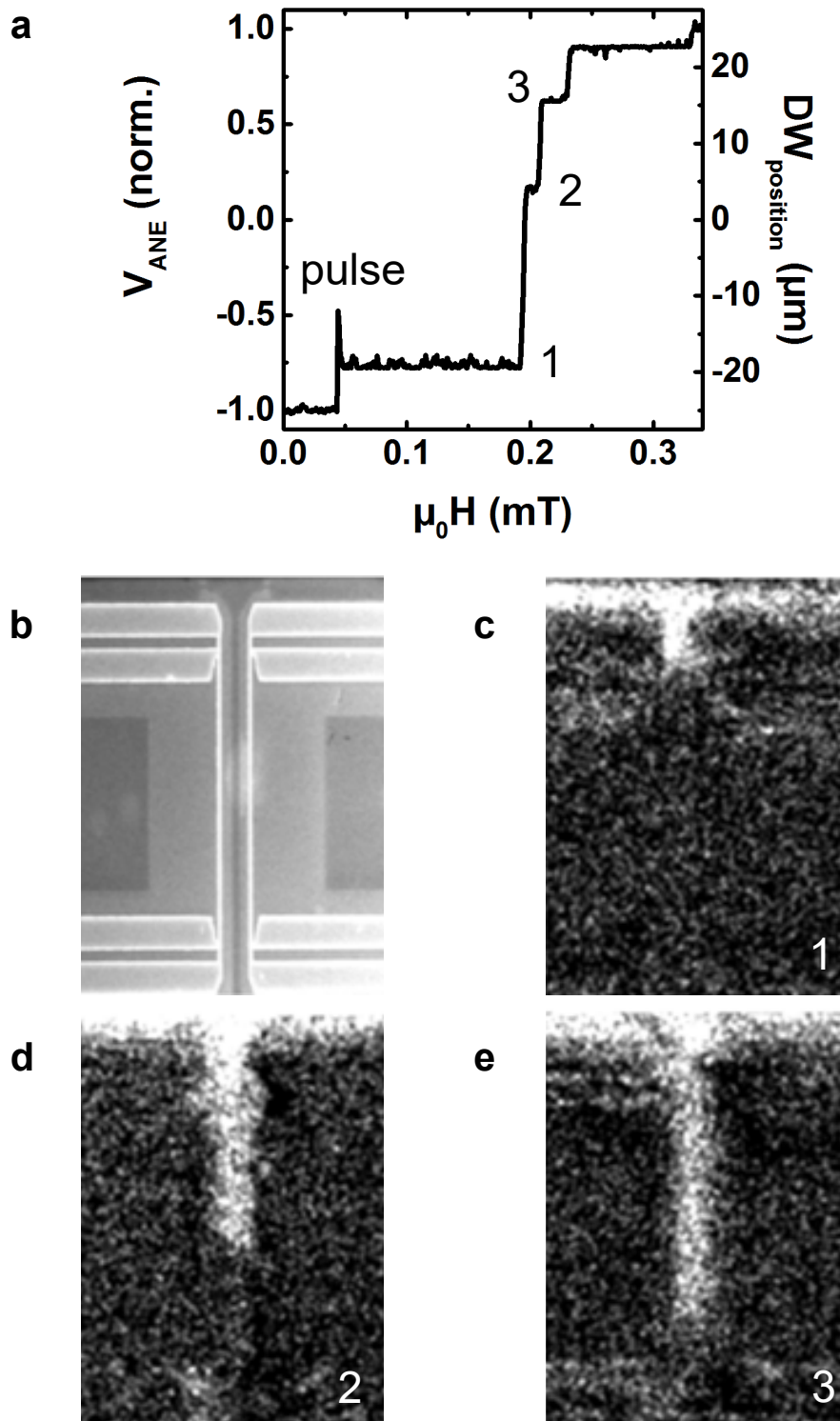
Figure 5.6. – Magnetic field driven domain wall motion. **a**, ANE voltage measurements and the DW position as a function of the magnetic in the presence of a DW in the microwire. **b**, Image of the device taken with MOKE setup. **c,d,e**, MOKE measurements of the microwire. The numbers correspond to the numbers marked in the ANE voltage measurement showing the position of the DW at the pinning sites.

3.3.1. Since the magnetization of the microwire is pointing out-of-plane and the polarization of the incident light from the was chosen close to be parallel to the out-of-plane axis of the sample, the geometry of the MOKE is the polar MOKE. The nucleation of the DW and sweep of the magnetic field were performed with the same parameters as during the ANE voltage measurements from figure 5.6a. This ensures that the nucleated DW in the MOKE measurements showed the same behavior as the ANE voltage measurements. Another important parameter was the temperature of the microwire. Since for the MOKE measurements no current needed to be applied to the heaters the cryostat temperature had to be corrected compared to temperature where the ANE voltage measurements were performed. For the MOKE measurements a microwire average temperature of 65.5 K was stabilized (same as the measurements in figure 5.3 and 5.6a).

A maximum contrast in the MOKE images was achieved using the following procedure: after the microwire was magnetized in the negative direction a reference image was taken, then the magnetic field was swept and the pulse was applied, but the magnetic field was only swept to a magnetic field value that corresponds to one of the pinning sites obtained from the ANE voltage measurements and then swept back to zero magnetic field. At this last point an image was taken. The final image is the obtained by subtracting the initial reference image from the obtained imaged after the DW driven procedure. This was then repeated for the three pinning sites showed in figure 5.6a. In figure 5.6c-e the different MOKE images for each pinning site are shown (the numbers in the right down corner refer to the pinning sites). In these images the white color corresponds to the magnetization pointing up and the black color to the down magnetization. The measurements have a certain amount of noise which is mainly due to the vibration of the cryostat that could not be stabilized completely. In general, obtaining high contrast MOKE images from microwires that are in the range of our microwire (2 µm) is not a trivial task due to the its lateral dimensions.

Comparing the position of the DW obtained by ANE voltage measurements and MOKE images, we obtain that the pinning sites of the DW in the microwire are at the same position within the measurement uncertainty as expected. This validates the ANE based method for the detection of the position and propagation of a single magnetic DW in a magnetic microwire.

5.4. Spin-torque driven DW motion

A torque on the magnetization of an ferromagnet can appear when the spin of an electron interacts with the magnetization of a magnetic material [129]. This phenomenon is known as spin-transfer torque (chapter 2 section 2.2.1). The understanding of this phenomenon has led to new electronic and magnetic functionalities in a wide variety of materials and devices. One of the most successful applications was the use of the spin-transfer torque in magnetic random access memories (MRAMs) [130]. Another possible application of this phenomena is the so called magnetic domain-wall racetrack memory [131]. In this concept, magnetic wires are used as tracks where DWs can move, be nucleated and modified by spin transfer torque representing the digital information as in random access memories (RAMs).

Similar as in the magnetic field driven motion experiments presented in section 5.3, the spin-transfer torque phenomenon was here used to move DWs from one position to another and record the ANE voltage during the motion of the DW. The position of the DW could be calculated from equation 5.1, using the measured ANE voltage. The experimental details are going to be explained next.

The DW nucleation in the microwire was performed with the same parameters as used in the magnetic field driven motion experiments presented in figure 5.6. With this procedure the position of the DW after nucleation is known, which is in the left side of the device as it is shown in figure 5.1. Different from the magnetic field driven motion experiment, however, the magnetic field was set to zero after the DW was nucleated and was kept constant during the measurement. The results of the measurements of the spin-torque driven DW motion are shown in figure 5.7. Before applying a pulse through the microwire the normalized ANE voltage signal starts with -1 (magnetization pointing down), after increasing the number of pulses and depending on the current density the ANE voltage signal shows some sharp transitions and plateaus until it reaches a value of +1 (magnetization pointing up). The applied pulses had a duration of 1 µs and the amplitudes of the pulses correspond to current densities (j) in the range from 6.3×10^9 A m^{-2} to 10.7×10^9 A m^{-2}. After each pulse was applied, 30 s waiting time was implemented before the next pulse was applied to avoid Joule heating of the microwire. The ANE voltage signal can be explained by the movement of a DW due to spin-transfer torque across the microwire.

In figure 5.7, depending on the current density of the pulse, the amount of pulses needed to be applied to the microwire to move the DW from its starting position to the other

end of the microwire changed. Also, the number of sharp transitions and plateaus depended on the current density. Similar as the measurements in figure 5.6 these sharp transitions and plateaus can be attributed to the pinning sites in the microwire. With equation 5.1 the position of the DW and so the pinning sites can be calculated using the ANE voltage measured. For the pulses with lower current density, the DW encounters more pinning sites in comparison to the pulses with higher current density. This means that the movement of the DW along the microwire is dominated by the pinning. Some of the pinning sites are so energetically favorable for the DW that they can be observed for different current densities, as is the case of the pinning site at a DW position of 20 µm. This pinning site was also observed in the field driven DW motion experiments (figure 5.6).
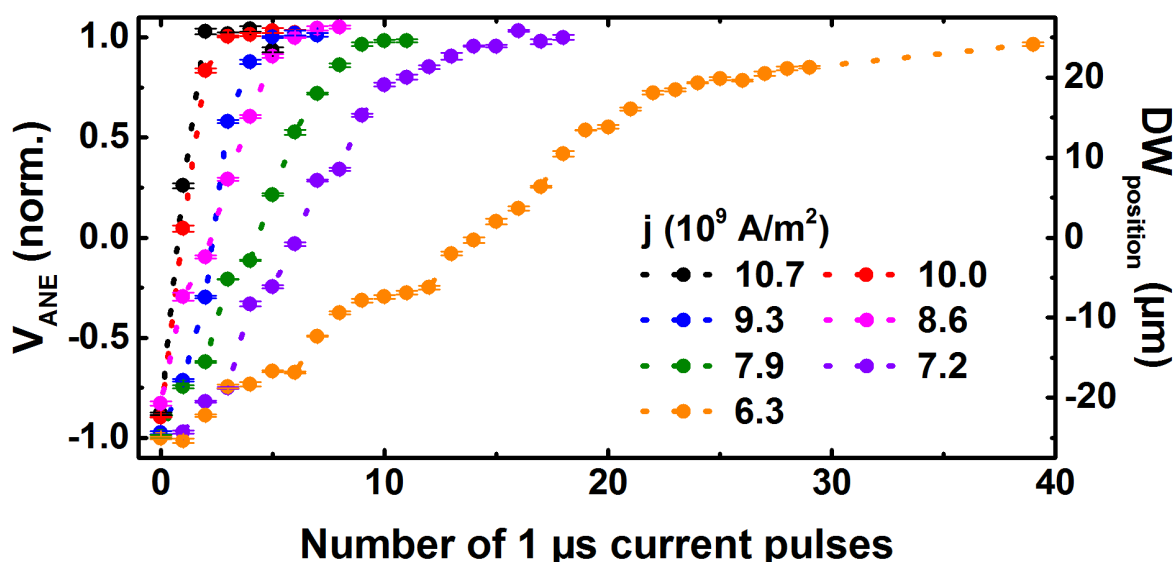
Figure 5.7. – Spin-torque driven DW motion. ANE voltage measurements as a function of the number of current pulses applied to the microwire. The amplitude of the pulse was changed and for each current density a measurement was performed. From the ANE voltage the position of the DW was calculated.

For the lowest pulse current density (orange points in figure 5.7) applied to the microwire, after 40 pulses the DW still has not reached the opposite side of the Cr/Au stripe-line. This measurement also shows plateaus in the ANE voltage, thus the ANE voltage does dot increase linearly with the number of pulses. This behavior can be explained by the fact that the extrinsic defects in the microwire are strong and the DW tends to be strongly pinned at these low current densities [52, 132, 133]. The region where this behavior happens is between the depinning and the flow regime of

movement of the DW. In contrast, at the highest current density (black points) the DW has moved across the microwire to the other end after two pulses. This would correspond to the flow regime (see chapter 2 section 2.2.1 for more information) of the DW movement. Since the DW position was calculated an approximate velocity of the DW can also be calculated, considering the measurement with the highest current density and the duration of the pulse. From these data, a velocity of $v \approx 30 \, \mathrm{m \, s^{-1}}$ was obtained.

One relevant aspect of these measurements is that by measuring the ANE, different pinning sites can be measured and located. In these types of devices, we assume that the pinning sites are due to defects that are intrinsic in the magnetic film or are induced by the lithographic patterning of the stripe. Only by using highly precise measuring methods/tools these local pinning defects can be observed and the detailed DW propagation can be understood. Hence ANE based measurements provide us a new tool for studying details of the DW propagation and pinning in microwires.
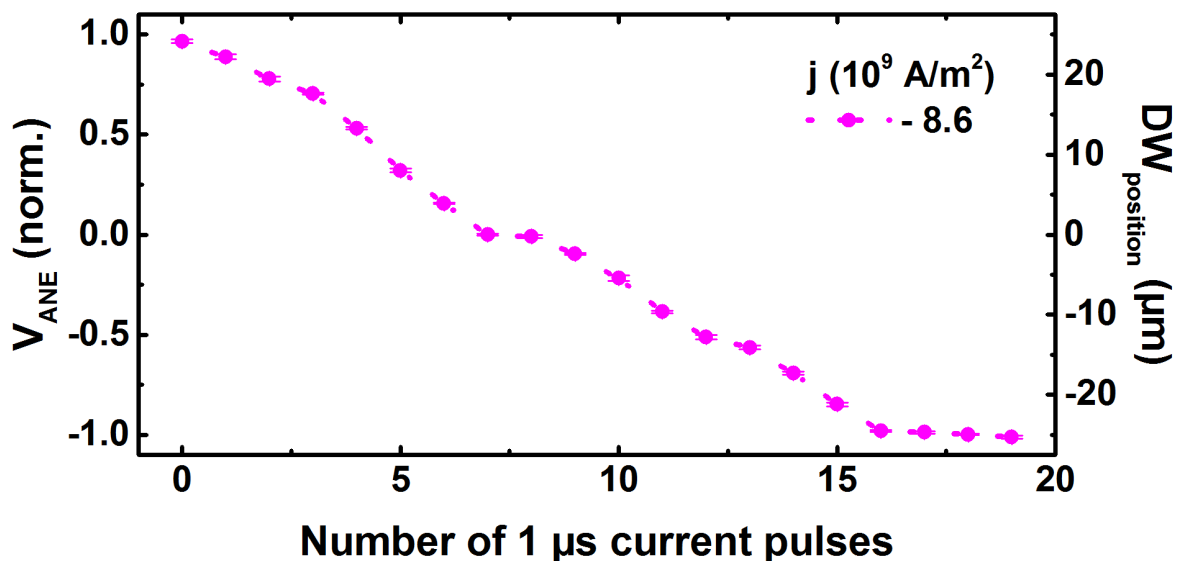
Figure 5.8. – ANE voltage as a function of the number of current pulses. The measurement was performed after the DW was moved to one end of the microwire (figure 5.7, orange dots) and then the polarity of the pulse was inverted.

In the measurements presented in figure 5.7, the DW was moved in one direction independently of the pulse amplitude. In the device studied the DW could only be nucleated at the same side of the microwire as described in section 5.3. This was due to that the Cr/Au stripe-line on the other side got damaged during the experiments

(not shown in the SEM picture of figure 5.1). Therefore, to study the propagation of the DW in the opposite direction (towards the working Cr/Au stripe-line), first a DW needed to be moved to the opposite end of the microwire. After the measurement of figure 5.7 with the lowest current density, the DW was left at this position and the polarity of the pulse was reversed. Since, at this position, the DW was strongly pinned, a higher current density was used to move the DW in the other direction (-8.6×10^9 $\mathrm{A\,m^{-2}}$). In figure 5.8 the ANE voltage as a function of the number of pulses for a pulse with an inverted polarity as the measurements in figure 5.7 is shown. From the ANE voltage and the calculated DW position the propagation in the opposite direction of the DW could be observed. By comparing this measurement with the measurement of figure 5.7 with the opposite polarity (8.6×10^9 $\mathrm{A\,m^{-2}}$) the movement in the opposite direction shows more pinning sites. One explanation for this could be that energy landscape of the pinning sites is asymmetric. Hence in this direction (from left to right) pinning is stronger than in the other direction (from right to left).

5.5. Temperature distribution with COMSOL

The temperature gradient distribution and amplitude, was estimated by finite element modeling of the heat flux in the device using COMSOL simulations with the joule heating package [134]. Details of the simulation parameters are found in the Annex B. The results from the COMSOL simulations are shown in figure 5.9. The temperature of the bottom GaAs substrate was set to ambient (cryostate) temperature for the simulations. The device geometry was taken from the experimental design. The lateral simulation size was set to 1 mm × 1 mm. For the simulation temperature dependent parameters such as the heat capacity and the thermal conductivity the values taken are for bulk GaAs from references [122, 135] respectively. Since the device consists of a thin film, the effective thermal conductivity might be lower due to additional interfaces and also due to some impurities in the device fabrication. The resistivity of the Pt heaters was taken experimentally from the device. The simulations performed provide an estimation of the lower boundaries of the temperature gradient.

Most of the measurements performed in the device, were performed for an AC current applied to the heaters with an amplitude of 4 mA. Thus, the simulations were performed using this parameter. In figure 5.9a and figure 5.9b the temperature distribution in the device is shown. The corresponding alternating current used for the generation of the temperature gradient is depicted in figure 5.9c. The frequency of

101
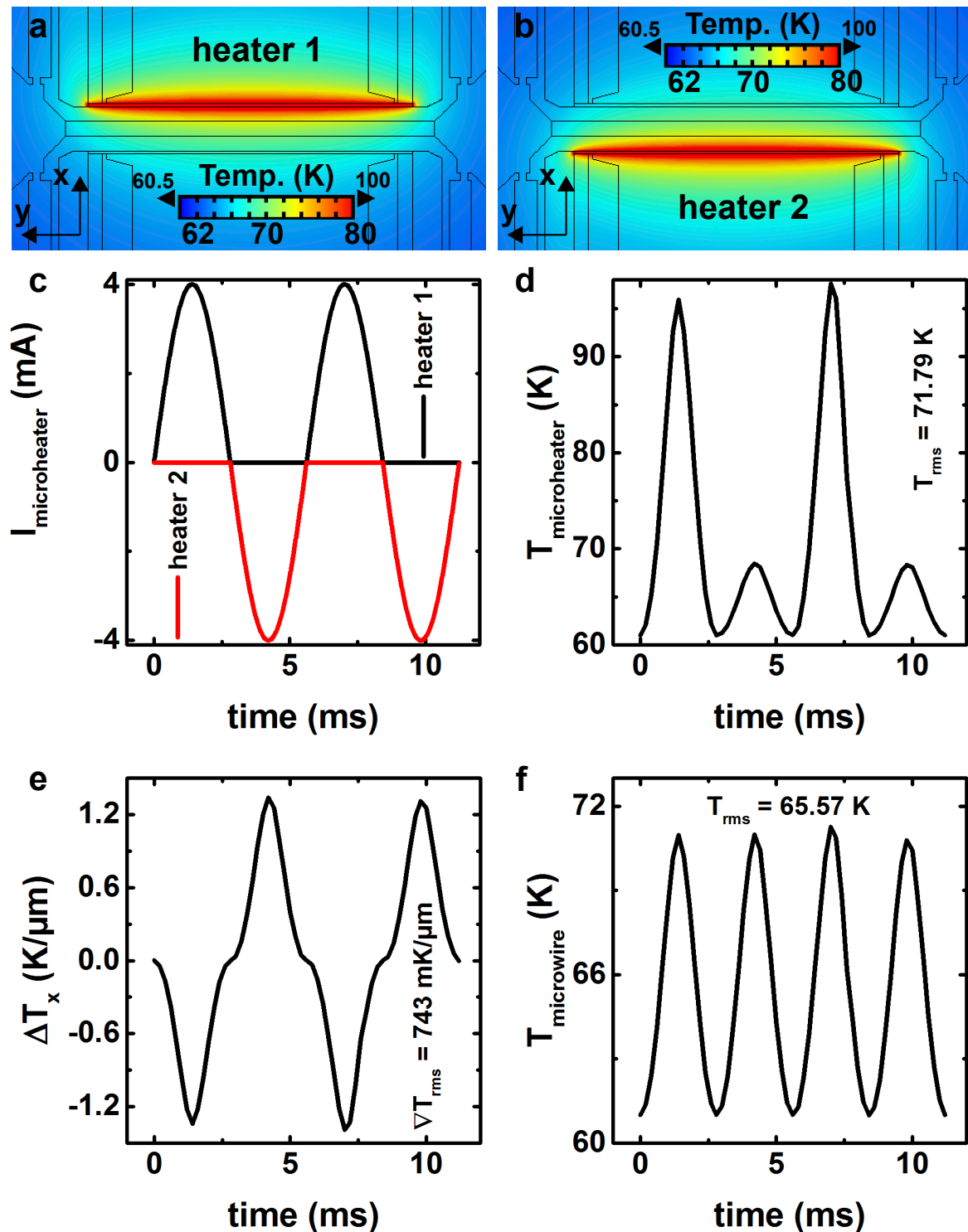
Figure 5.9. – COMSOL temperature distribution simulations. **a**, **b**, temperature distribution in the device for a amplitude of 4 mA applied to the heaters. **c**, the alternating current that is applied to the microheaters with and amplitude of 4 mA and a frequency of 178 Hz. **d**, temperature of the heater 1 as a function of time. **e**, the temperature of the microwire during the Joule heating process. **f**, average temperature gradient across the microwire.

this alternating current was set to 178 Hz for the simulations which corresponds to the experimental value. In figure 5.9d the resulting temperature of heater 1 (upper heater from figure 5.1) can be observed as a function of time, the temperature varies depending on the current through the heaters. As a result, a temperature of $T_{\text{rms}} = 71.79$ K for the heater 1 was obtained. For the nanowire the temperature obtained was $T_{\text{rms}} = 65.57$ K and the result from the simulation is shown in figure 5.9e. This value was expected since the ambient temperature for the simulations was set to 65.5 K, same as the temperature of the measurements. In figure 5.9f the average temperature gradient across the microwire is depicted. The temperature gradient shows a dominant oscillation at the same frequency as the current used for the heaters and not at double the frequency as the temperature of the microwire. If we average the temperature gradient over the whole length of the microwire we obtain a temperature gradient of $\overline{\nabla T_x} = 743$ mK µm^{-1}. Note that the temperature gradient does not show a perfect sinusoidal shape as the temperature of the microwire. This is because both heaters influence each other as can be seen in figure 5.9d, the small peaks show the increase of temperature of the heater 1 when the temperature of heater 2 is at its maximum.

Taking the average temperature gradient obtained from the simulations ($\overline{\nabla T_x} = 743$ mK µm^{-1}), the value of $V_{\text{ANE}}^{\max} = 1.24$ µV which is the ANE voltage value at saturation from the measurement for a current of 4 mA in amplitude is applied to the heater (figure 5.3) and taking $\mu_0 M_s = 22.90$ mT, where μ_0 is the magnetic permeability and M_s is the saturation magnetization, we can estimate the ANE coefficient of the microwire material from $V_{\text{ANE}}^{\max} = -N_{\text{ANE}}\mu_0 M_s l \overline{\nabla T_x}$, where l is the length of the wire (50 µm). Which results in a value of -1.52 µV K^{-1} T^{-1} for a temperature of 65.5 K.

6. Skyrmion devices

In this chapter the thermoelectric properties of individual skyrmions are analyzed. A similar device as presented in chapters 5 and chapter 4 is introduced which is suitable for measuring the anomalous Nernst effect (ANE). The thermal properties of the device were characterized by temperature/resistance measurements in combination with finite element simulations. The controllable nucleation of skyrmions in the device and the annihilation of single skyrmions using a magnetic force microscope (MFM) are explained. The MFM is also used to characterize the number, size, and spatial distribution of the skyrmions and in combination with the ANE measurements the thermoelectric signal of individual skyrmions is derived. Furthermore, an analysis technique is presented that allows to obtain the effective skyrmion area from the MFM measurements. This technique is employed to study the dependency of the effective skyrmion area as a function of the magnetic field. Also, possible topological contributions to the experimentally observed thermoelectrical signal are discussed.

6.1. Anomalous Nernst effect device

The device consists of a magnetic microstripe positioned in the center of the device and a platinum (Pt) heater next to the microstripe. In comparison to the geometries studied in chapter 5 and chapter 4, the device has only one heater. Two SEM pictures with different magnifications of the fabricated device are shown in figure 6.1. The composition of the microstripe was a multilayer stack of Ta 5/Pt 8/(Co 1.0/Ru 1.4/Pt 0.6)x10/Pt 2.4 (numbers are thickness in nm), which were deposited at room temperature by direct current sputtering under an argon pressure of 2.5 mbar on a thermally oxidized Si substrate. This device was fabricated according to the fabrication procedure described in chapter 3 section 3.1. The microstripe was electrically connected at 4 different points by Pt contacts. The contacts in the middle of the microstripe were separated by 8 µm. The microstripe had a width of 2 µm and the heater had

105
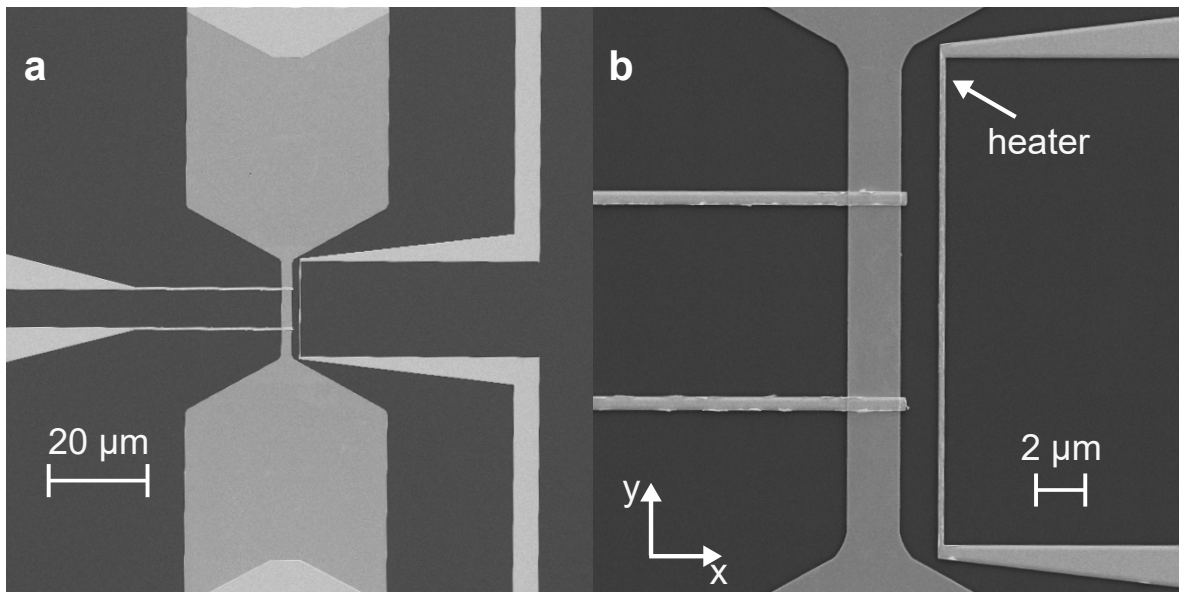
Figure 6.1. – SEM picture of the ANE device. **a**, overview of the complete device showing the microstripe and the heater. **b**, a zoom in to device.

a distance of 1.5 µm to the edge of the microstripe. The heater length surpassed the distance between the middle contacts of the microstripe to achieve a uniform heating in the relevant area. The thickness of the heater and of the contacts was 100 nm.

The multilayers (Pt/Co/Ru) from which the microstripe was fabricated show perpendicular magnetic anisotropy (PMA) and interfacial Dzyaloshinskii–Moriya interaction (DMI) [136–138]. Due to the PMA, the magnetization points in the out-of-plane direction without applying an external magnetic field. The combination of the PMA and the interfacial DMI allows to stabilize skyrmions at room temperature in multilayers systems as was introduced in chapter 2 section 2.3. The interfacial DMI in this case arises due to a structural inversion symmetry that exist since the magnetic layer (Co) is alternated between two different heavy metals (Pt and Ru) that have large spin orbit coupling.

6.2. Device characterization and properties

The first characterization step was to measure the temperature increase of the microstripe when a current was applied to heater. Therefore, the microstripe and the heater were used as temperature sensors by measuring their resistance change, induced

by the Joule heating of the heater. The ANE device presented in figure 6.1 does only allow 2-wire resistance measurements of the heater. Because of this, in the same fabrication process as for the "normal" ANE device a separate device with the same geometry was fabricated but with additional contacts allowing a 4-wire resistance measurement. The first set of measurements consisted of calibrating the temperature resistance coefficient of the heater and microstripe. For this, during the resistance measurements, both devices, were put in a temperature-controlled air bath unit, where temperatures could be stabilized in the range from 288 K to 314 K. To avoid resistance changes in the form of heating due to the sensing current, this was set to 100 µA, which showed no sign of self-heating in the resistance measurements. In the temperature range where the measurements were performed, the resistance of the microstripe and the heater shows a linear dependency as can be seen in figure 6.2a. From these measurements the resulting temperature coefficients of resistance α, were determined as 8.7×10^{-4} for the microstripe and the heater 1.5×10^{-3}, respectively. The knowledge of these two coefficients allows to backward calculate the temperature from a given resistance value of the microstripe or the heater.

The temperature increase of the microstripe and the heater were then determined by measuring their resistance separately for different currents applied to the heater. After the current was increased a waiting time of 15 min was set. This was performed to ensure that the device was in thermal equilibrium. The results are shown in figure 6.2b for an ambient temperature of 295 K. The temperature dependence of the microstripe and the heater show a quadratic dependency on the heater current as expected for Joule heating. For a heater current value of 4.3 mA, an average increase of the temperature of 8.06 K (ΔT_{res}) and 165.1 K are found for the microstripe and the heater, respectively.

From the resistance measurements the average temperature increase of the microstripe and the heater can be calculated, However, it is not possible to calculate the thermal gradient along the different spatial directions. Measuring a thermal gradient requires a differential temperature measurement at two different distances. This was not possible in the device that was fabricated. To estimate the gradient at the microstripe, thermal finite element modeling of the device was performed by using the COMSOL software [134]. For the simulations the Joule heating package of the Heat Transfer Module was used. The geometry and dimensions of the modeled sample were taken from the layout of the ANE device showed in figure 6.1. Temperature dependent bulk material parameters, e.g. thermal conductivity κ and heat capacity C_p, were taken from references [139–143], and are summarized in the Annex B.

107
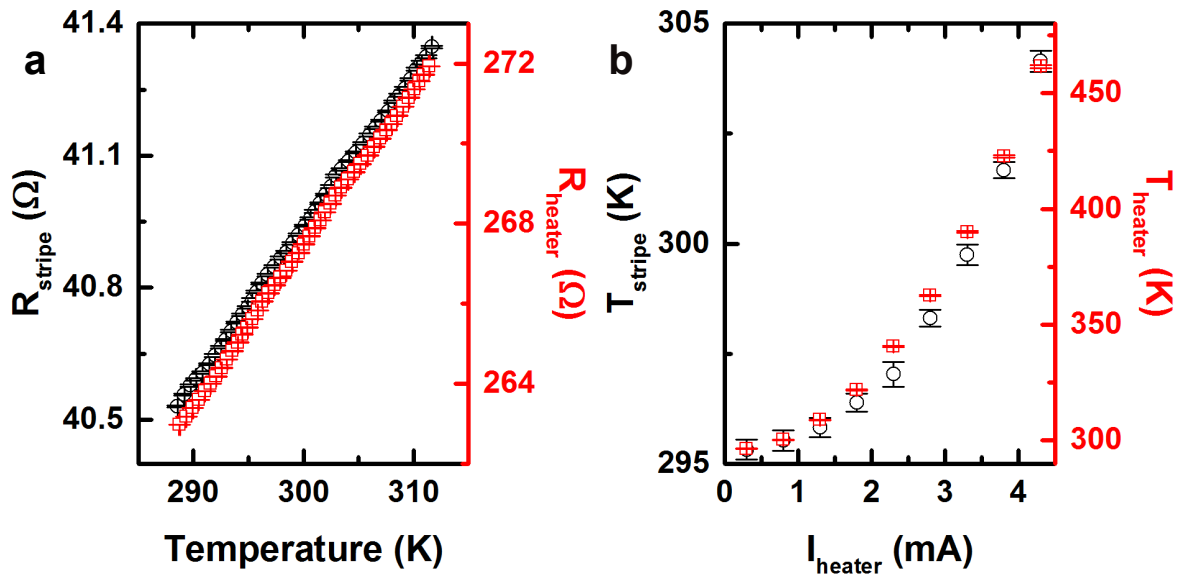
Figure 6.2. – Temperature change generated by the heater. **a**, 4-wire resistance measurements of the microstripe (black circles) and heater (red squares) as a function of temperature. **b**, Temperature of the microstripe (black circles) and heater (red squares) as a function of the current applied to the heater. The ambient temperature for this measurement was set to 295 K.

In figure 6.3 the results from the thermal finite element simulations for a heater current value of 4.3 mA are shown. In the examples the heater current was fixed at 4.3 mA. The temperature distribution in the device is shown in figure 6.3a, where the temperature at the heater is much higher than in the microstripe, as was expected. Also, the temperature distribution in the middle of the microstripe in between the two contacts, which is the area of interest for the measurements, shows no significant variation along the y-direction.. This mainly results from the heater being longer than this section of the microstripe. By taking a line profile across the temperature distribution in figure 6.3a (white dashed line) temperature values as a function of the distance can be obtained, the results are shown in figure 6.3b. The temperature of the device increases to about 478 K in the heater and then drops abruptly to 305 K in the center of the microstripe. The inset in figure 6.3b shows the temperature drop across the microstripe. It shows an almost linear behavior. From this data an average temperature increase of $\Delta T_{\mathrm{sim}} = 8.6$ K is obtained which is near to the value obtained in the resistance measurements (ΔT_{res}) explained above.

The distribution of the thermal gradient in the x, y, z axes can be directly obtained from

the same simulations. The results are shown in the figures 6.3c-e. The figures show that the thermal gradient along the x-axis is significantly higher than along the y and z axes. The thermal gradients along the y and z axes, show more pronounced contributions near the contact areas, as can be seen more clearly in figure 6.3e. However, the thermal gradient along the z-axis which is much smaller in magnitude than the thermal gradient along the x-axis. For the average thermal gradients along the different orientations values of $\overline{\nabla T_x} = 4.2$ K µm^{-1}, $\overline{\nabla T_y} = 0.2$ mK µm^{-1} and $\overline{\nabla T_z} = 2.9$ mK µm^{-1}, are obtained respectively.

The thermal finite element modeling showed that the thermal gradient along the x-axis contributes the largest share to the total gradient. Additionally, the magnetization in the microstripe is out-of-plane. Therefore, the thermovoltage measured at the contact position shown in figure 6.1 can be predominantly attributed to the anomalous Nernst effect (ANE), as can be seen from the equations obtained in chapter 2 section 2.4.2. Hence, the other thermoelectrical contributions will be neglected in the upcoming analysis. In the following, the ANE voltage measurements that were performed with a Lock-In amplifier following the methodology presented in chapter 3 section 3.2 are discussed.

In a first step, the ANE device and its switching behavior were analyzed. To this end the ANE voltage (V_{ANE}) response of the device to an applied magnetic field ($\mu_0 H_z$) in the out-of-plane direction, was measured and is shown in figure 6.4a when a current of 4.3 mA with a frequency of 2024 HzHz was applied to the heater. The field dependence of V_{ANE} shows the characteristic switching behavior of materials with out-of-plane anisotropy and the V_{ANE} response is similar to the one presented in chapter 5 section 5.2. However, this time the ANE voltage changes slowly with the applied magnetic field and not abruptly. This indicates, that the magnetization inside the microstripe switches via a multidomain state unlike in (Ga,Mn)(As,P) where single domain wall passed through the microwire. This type of hysteresis loop measurement was also performed for other heater currents maintaining the same frequency. The amplitude of the ANE ($V_{\mathrm{ANE}}^{\mathrm{max}}$) was calculated from the difference of the of the saturated V_{ANE} values for positive and negative fields, to eliminate offsets. The results are shown as the red dots in figure 6.4b. By comparing the $V_{\mathrm{ANE}}^{\mathrm{max}}$ with the temperature increase in the microstripe (T_{stripe}) depicted in the black dots the thermoelectrical origin of the measured V_{ANE} signal is confirmed, since it is proportional to T_{stripe} and hence $\overline{\nabla T_x}$ and scales quadratically with the heater current.

The Nernst coefficient for the microstripe can be calculated using the measured $V_{\mathrm{ANE}}^{\mathrm{max}}$
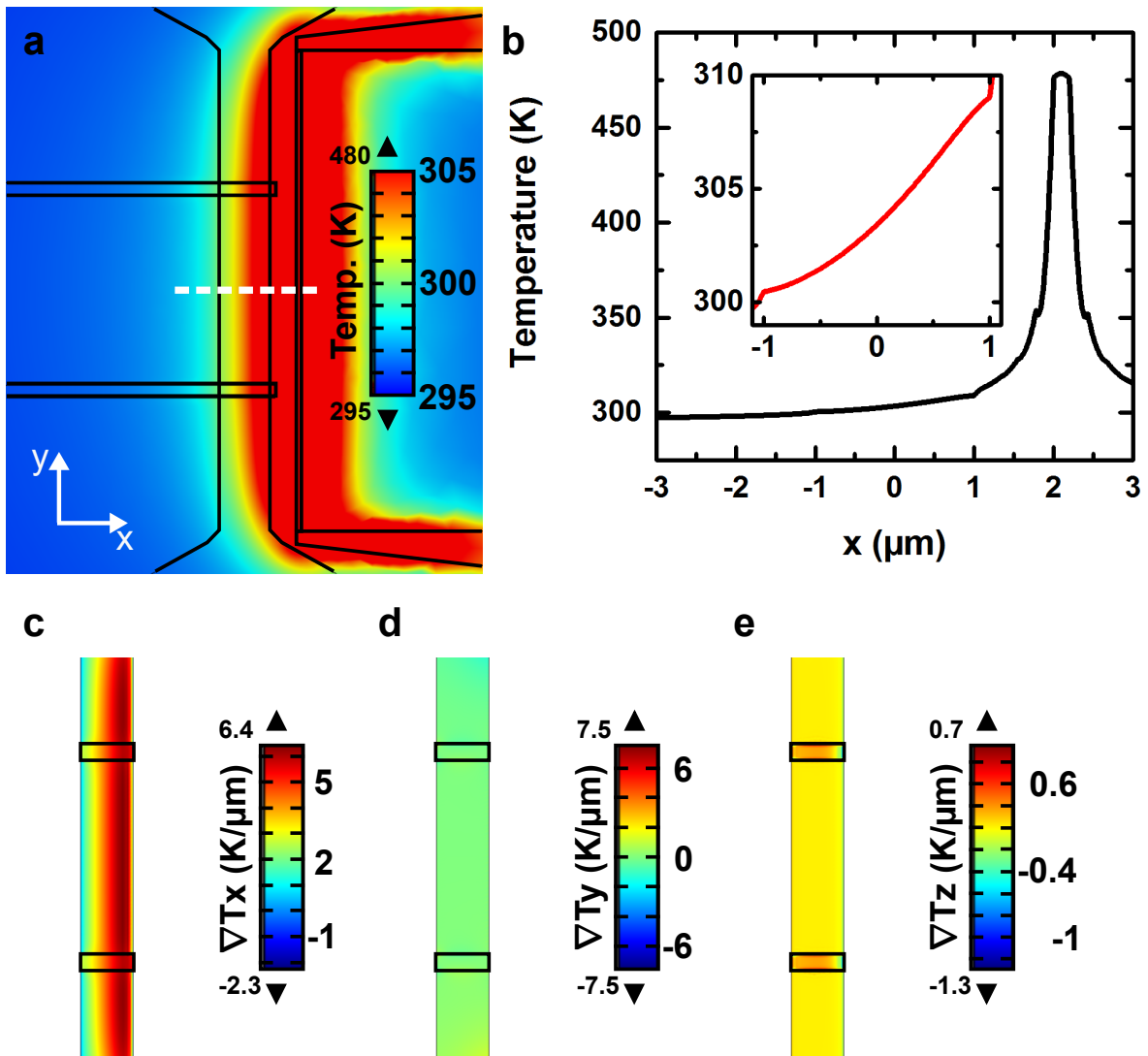
Figure 6.3. – Thermal finite element modeling using COMSOL. The heater current for the simulations was set to 4.3 mA. **a**, the temperature distribution in the device. **b**, line profile in the temperature distribution in the device across the microstripe and heater showed in **a**. The temperature drops from 478 K at the microheater to about 305 K at the microstripe center (inset picture). **c** - **e**, the distribution of the thermal gradient along the x, y, z axes. The simulations show values of the average thermal gradient of $\overline{\nabla T_x} = 4.2$ K μm^{-1}, $\overline{\nabla T_y} = 0.2$ mK μm^{-1} and $\overline{\nabla T_z} = 2.9$ mK μm^{-1}.

data. The ANE equation presented in chapter 2 section 2.4.1 can be rewritten for our particular geometry according to [144] as:

$$V_{\mathrm{ANE}} = -N_{\mathrm{ANE}}\mu_0 l \overline{\nabla T_x} M_{\mathrm{z}} \tag{6.1}$$

where N_{ANE} is the ANE coefficient per magnetic moment, μ_0 is the vacuum permeability, l is the wire length, $\overline{\nabla T_x}$ is the averaged ∇T_x and M_{z} is the averaged z-component of the magnetization between the contacts. The condition for saturation is denoted by $M_{\mathrm{z}} = M_{\mathrm{s}}$, the saturation magnetization. By taking values of $V_{\mathrm{ANE}}^{\max}$ for a heater current of 4.3 mA, the average thermal gradient $\overline{\nabla T_x}$ obtained from the simulations, the length of the wire between the contacts ($l = 8$ µm) and $\mu_0 M_{\mathrm{s}} = 1.4$ T from magnetometry data, a Nernst coefficient of $N_{\mathrm{ANE}} = 8.1$ nV K^{-1} T^{-1} is derived.

Additionally, the impact of the heater frequency was tested, to analyze if independent of the heater frequency, the ANE signal obtained would also scale quadratically with the heater current as another proof that the measured signal is due a thermoelectrical effect. The results of these measurements are shown in figure 6.4c and they confirm that the frequency does not have an influence on the measured signal.

For this study it was important to understand which types of domains were present in the microstripe. From the observed V_{ANE} dependency on the applied magnetic field (figure 6.4a), it can be inferred that multiple domains are nucleated in the microstripe. They shrink as the amplitude of the magnetic field increases. To validate this assumption the magnetic domains in the microstripe can be observed by performing magnetic force microscopy (MFM) measurements and ANE measurements simultaneously. The measurement setup allowed simultaneously to perform both measurements without moving the sample from its position, see chapter 3 section 3.4.3 from the description of the setup. The MFM and ANE measurements are shown in figure 6.5. As was described in chapter 3 section 3.3 this type of measurements allows to detect the magnetic forces acting on the MFM tip, which in this case are evoked by the magnetic stray field of the microstripe. In the experiments a commercial low magnetic moment MFM tip (NT-MDT MFM LM) was used. Before starting the MFM measurements the sample was first magnetized in the positive out-of-plane direction to ensure that all domains were erased, then the magnetic field was swept from ≈ 70 mT to 0 mT at the same rate as used for the ANE measurements (figure 6.4a). Then to observe the magnetization reversal process, the magnetic field was further stepwise reduced in the negative direction until the saturation was reached. At each field step, an MFM image
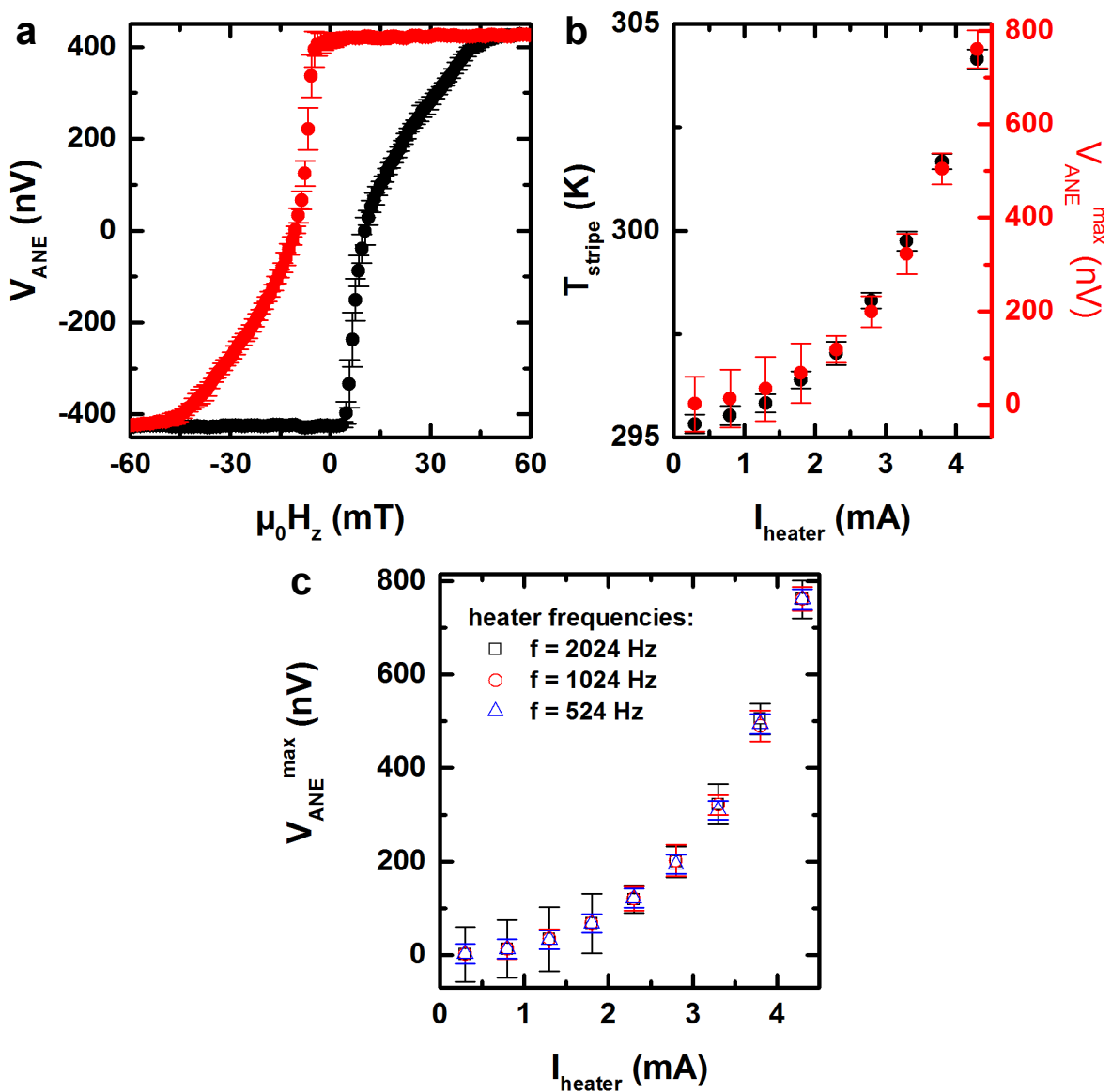
Figure 6.4. – ANE hysteresis loop measurements. **a**, ANE voltage as a function of the applied magnetic field. The black and red data points represent the direction of the applied magnetic field, being first applied from negative to positive and then reversed. The ambient temperature was 295 K and the heater current was 4.3 mA with a frequency of 2024 Hz. **b**, the temperature increase of the microstripe compared to the amplitude of the ANE signal as a function of the heater current. Both measurements have a starting ambient temperature of 295 K. **c**, the amplitude of the ANE signal as a function of the heater current for different heater frequencies.
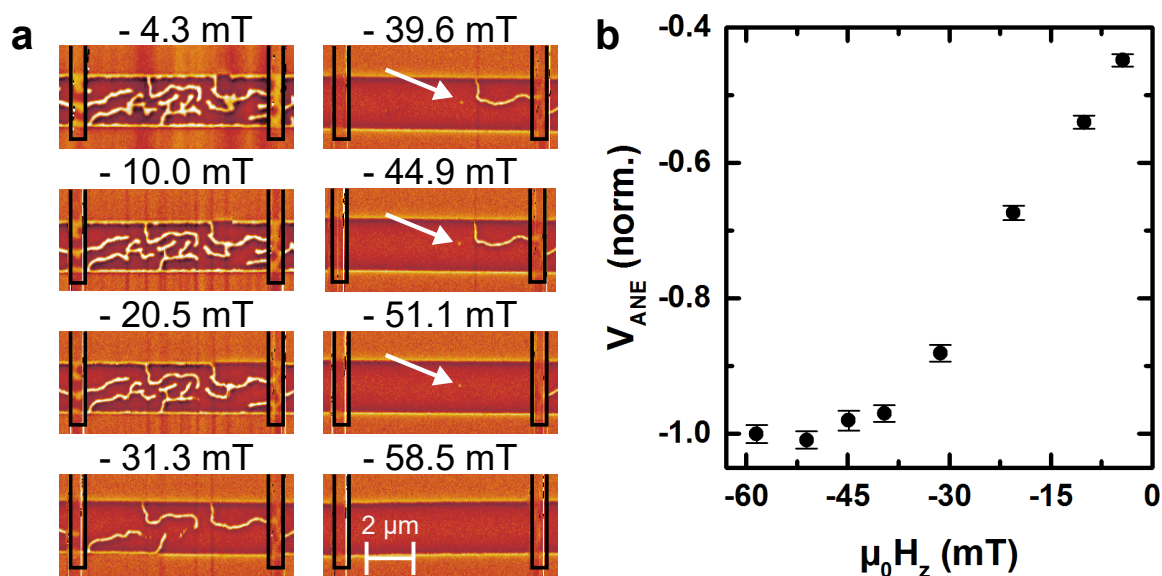
Figure 6.5. – MFM measurements in combination with ANE voltage measurements. **a**, MFM measurements of the microstripe for increasingly negative values of the out-of-plane magnetic field. The white arrow indicates the presence of one skyrmion inside the microstripe. **b**, the corresponding ANE voltage measurements of the MFM images shown in **a**.

was taken. Since the filed sweep procedure reproduces the sweep process chosen for the ANE measurements. It can be assumed, that for all field values the MFM images depict a similar situation as present during the ANE measurements in figure 6.4a. The MFM measurements are shown in figure 6.5a. In these measurements the MFM tip was magnetized in the negative direction which was the same as the applied magnetic field during the measurements. The bright areas correspond to the positive and dark areas to the negative out-of-plane magnetization respectively. A maze or worm domain pattern can be seen with a field dependent size of the mazes. As the magnetic field increases in amplitude the maze domains reduce in width and tend to decrease in quantity. This behavior explains the observed response in the ANE voltage as was assumed before. In three of the MFM images (marked with an arrow) it can be seen that a skyrmion is stabilized inside the microstripe; this magnetic field induced skyrmion nucleation is a stochastic process since the in a second try of these measurements this skyrmion was not observed. But from this observation it can be concluded that in these films also occasionally skyrmions can be nucleated by performing magnetic field hysteresis loops.

Additionally, to the MFM measurements of figure 6.5a, ANE voltage measurements

were performed directly after the MFM images were taken. The results are shown in figure 6.5b. Here the ANE voltage was normalized with the ANE voltage value when the magnetization was saturated in the negative direction. A similar magnetic field dependency as the measurements of figure 6.4a is found. Small field offsets between ANE measurements of 6.4a and 6.5b can be explained by the additional magnetic field of the magnetic tip, that interacts with the microstripe during the scanning process in the MFM. For instance, at a magnetic field of -4.3 mT in the measurements of figure 6.5b the are almost 25% more domains pointing in the negative direction than in the positive direction, which, in the case of the figure 6.4a, would correspond to a magnetic field of approximately of -35 mT. It can be concluded that even with a low moment MFM tip, the scanning process contributes significantly to the magnetization reversal process.

6.3. Skyrmion nucleation and single skyrmion annihilation in the microstripe

6.3.1. Skyrmion nucleation

In this study, a controllable nucleation process for skyrmions inside the microstripe was an important prerequisite. The measurements of figure 6.5a show that by performing magnetic field hysteresis loops skyrmions can be nucleated. But this nucleation process was rather stochastic and not reproduceable. Therefore, an alternate and more reproducible skyrmion nucleation process was implemented by means of DC currents through the skyrmion hosting material [27,145,146]. Experimentally, there are different approaches how to nucleate skyrmions by means of DC currents, using constrictions which are patterned in the skyrmion material [24, 27], or lithography patterned contacts on top of the skyrmion material [62, 147] or by applying single/bipolar pulses in the magnetic material [26, 28–30].

The nucleation of skyrmions in this study was performed by applying single current pulses. By this approach skyrmions can be nucleated along the complete microstripe as was shown in [26]. This is important since the detection of the ANE in the device fabricated can only detect the magnetic structure in the microstripe between the contacts (see figure 6.1 for the ANE device) and magnetic structures outside do not contribute to the ANE. In comparison to other experiments, here in this study just

114
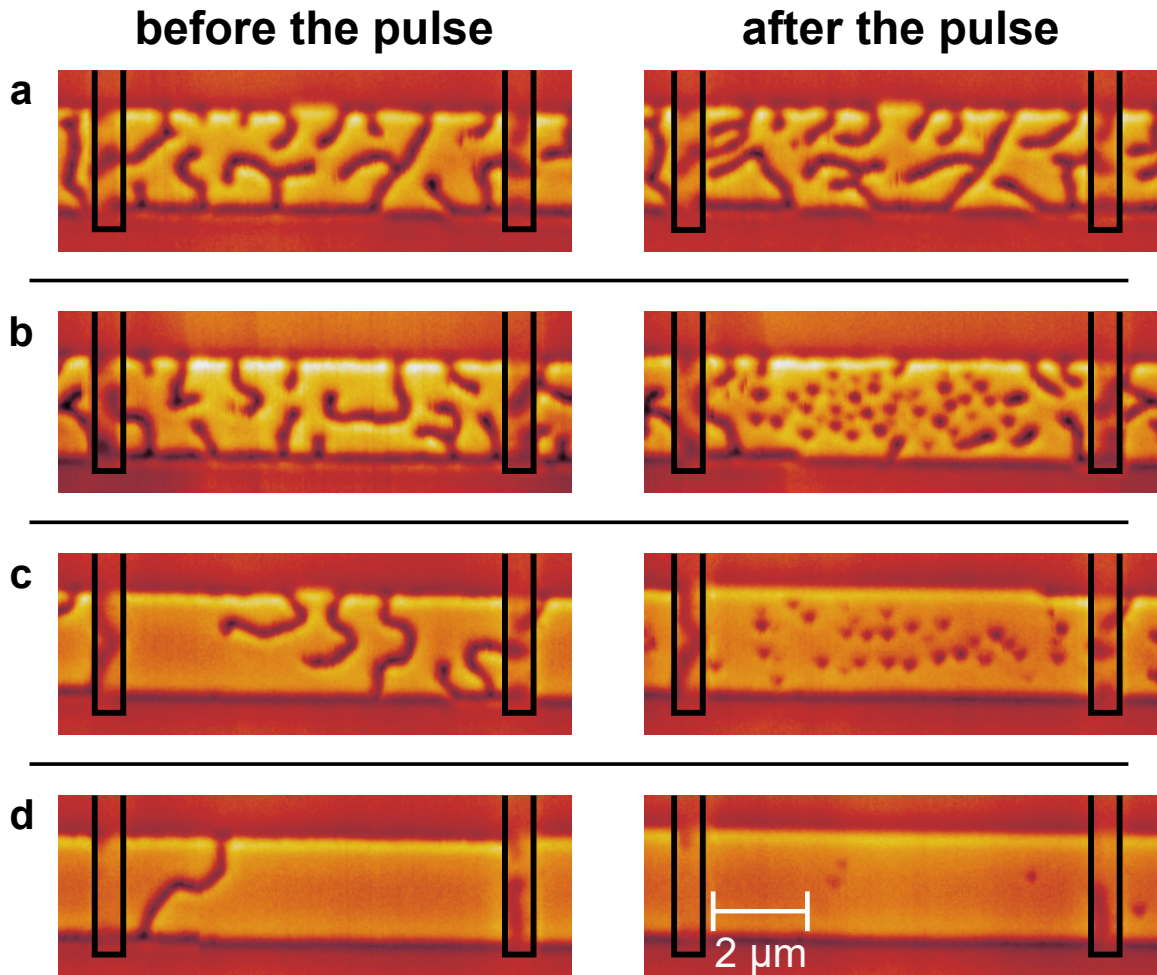
Figure 6.6. – Examples of skyrmion nucleation in the microstripe. **a** - **d**, MFM measurements before applying a single squared current pulse to the microstripe for different parameters of the current density j and the magnetic field $\mu_0 H_z$. **a**, j $= 3.55 \times 10^{11}$ A m^{-2}, $\mu_0 H_z = 11.28$ mT no skyrmion is created and only perturbation of maze domains is observed. **b**, j $= 3.76 \times 10^{11}$ A m^{-2}, $\mu_0 H_z = 11.28$ mT observation of the coexistence skyrmions and maze domains. **c**, j $= 3.86 \times 10^{11}$ A m^{-2}, $\mu_0 H_z = 17.16$ mT only skyrmions are observed (high density). **d**, j $= 3.97 \times 10^{11}$ A m^{-2}, $\mu_0 H_z = 23.05$ mT only skyrmions (low density) are observed.

one single square current pulse with a nominal duration of 200 ns was applied between the two large contacts that connect the microstrip. The pulses were always applied in the presence of a magnetic field which helps to stabilize skyrmions in these types of multilayer systems [23].

Examples of the outcome of this nucleation mechanism can be observed in figure 6.6, where MFM measurements were performed before and after the pulse was applied. In the experiments the current densities j of the pulse ranged from 3.34×10^{11} A m^{-2} to 3.97×10^{11} A m^{-2} and the magnetic fields were in the range of $\mu_0 H_z = 0.49$ mT to $\mu_0 H_z = 40.7$ mT. Before the pulse was applied, the magnetization was saturated out-of-plane in the negative direction of the device by sweeping the magnetic field and then the magnetic field was reversed to the desired value where the pulse was applied. In all the cases before the pulses a maze domain domain pattern was present. After the pulses three different magnetization patterns can be observed: the so-called worm or maze domains (figure 6.6a), coexistence of skyrmions and maze domains (figure 6.6b), or only insolated skyrmions (figure 6.6c and figure 6.6d). Depending on the parameters chosen (j and $\mu_0 H_z$) also the density of skyrmions can be tuned as can be seen in the MFM images of figure 6.6c and figure 6.6d. Also, it can be observed that the skyrmions nucleate above a certain current density which is shown for the case of the figures 6.6a and figure 6.6b where, starting from similar domain patterns, the same magnetic field is applied. After slightly increasing the current density from 3.55×10^{11} A m^{-2} to 3.76×10^{11} A m^{-2}, skyrmion nucleation sets in.

These results motivated further measurements where the parameters for j and $\mu_0 H_z$ were systematically varied. The results of the MFM measurements are shown in figure 6.7. To shorten the measurement time, MFM measurements were only performed after the pulse was applied and not before. The tip sample interaction at higher fields was avoided by reducing the magnetic field to a value of ≈ 11 mT after the pulse was applied. This was done only in the measurements where the magnetic field for the nucleation exceeded 11 mT. This tip sample interaction leads to the annihilation of skyrmions, as will be discussed in section 6.3.2. The stochastic distribution of skyrmions in the MFM measurements indicates that there are no preferential nucleation sites. These measurements can be summarized in a phase diagram where the final magnetization state is displayed as a function of j and $\mu_0 H_z$, this phase diagram is shown in figure 6.8. In the phase diagram, the dotted line marks the region where only skyrmions are nucleated by the current pulse (blue triangles).

a -0.5 mT   37.7 mT
40.7 mT
$j = 3.34 \times 10^{11}$ A/m^2

b -0.5 mT   34.8 mT
11.2 mT   37.7 mT
23.1 mT   40.7 mT
$j = 3.55 \times 10^{11}$ A/m^2

c 17.1 mT   28.9 mT
$j = 3.65 \times 10^{11}$ A/m^2

scale: ⊢⊣ 2 µm

d -0.5 mT   34.8 mT
11.2 mT   37.7 mT
23.1 mT   40.7 mT
$j = 3.76 \times 10^{11}$ A/m^2

e 17.1 mT   28.9 mT
$j = 3.86 \times 10^{11}$ A/m^2

f -0.5 mT   34.8 mT
11.2 mT   37.7 mT
23.1 mT   40.7 mT
$j = 3.97 \times 10^{11}$ A/m^2
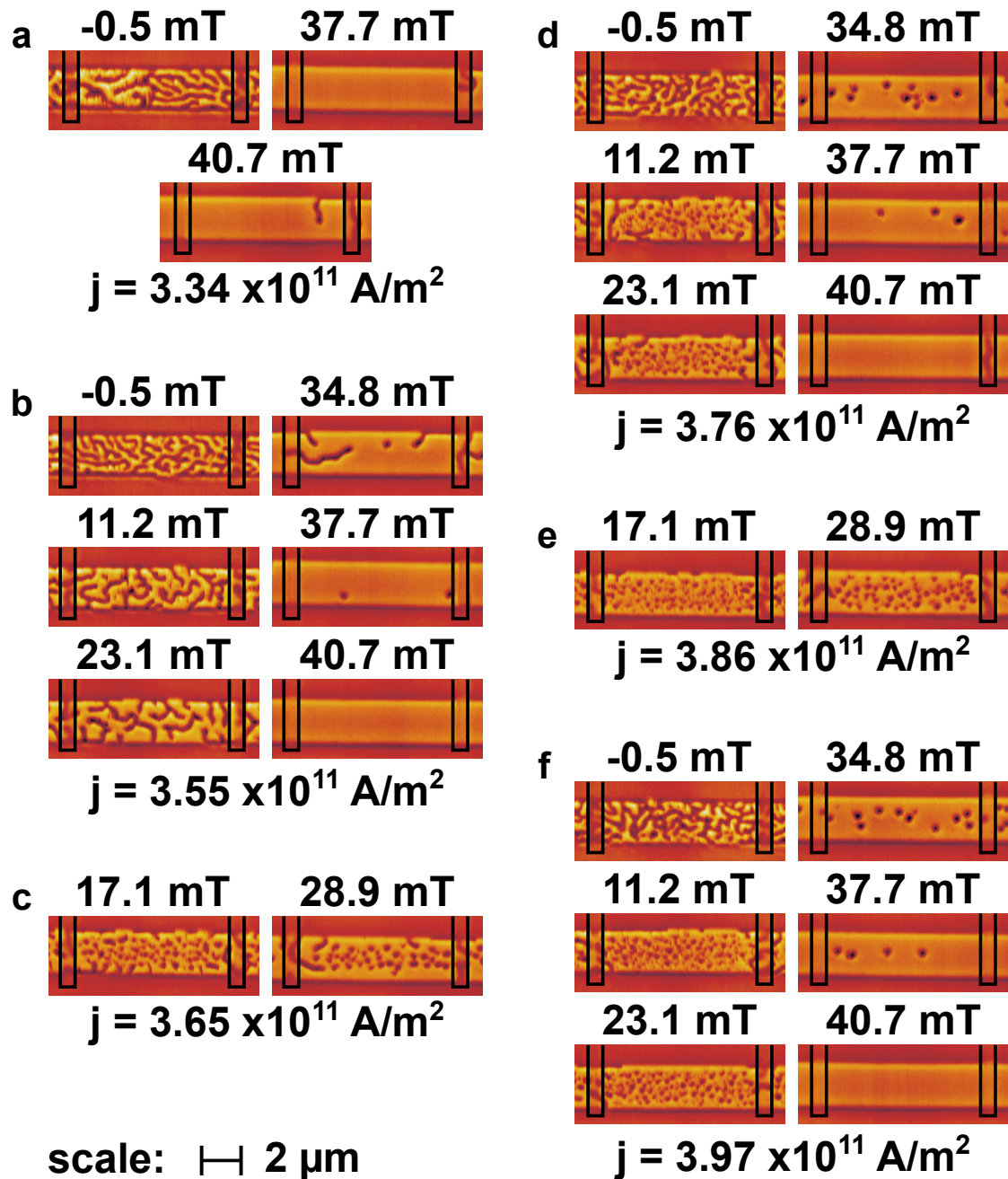
Figure 6.7. – **a** - **f**, MFM images after the current pulse was applied for different parameters of j and $\mu_0 H_z$. The magnetic field value which is displayed indicates the magnetic field at the moment the pulse was applied. After the pulse was applied the magnetic field was reduced to ≈ 11 mT this was the case for the measurements where the magnetic field during the pulse was higher than ≈ 11 mT.
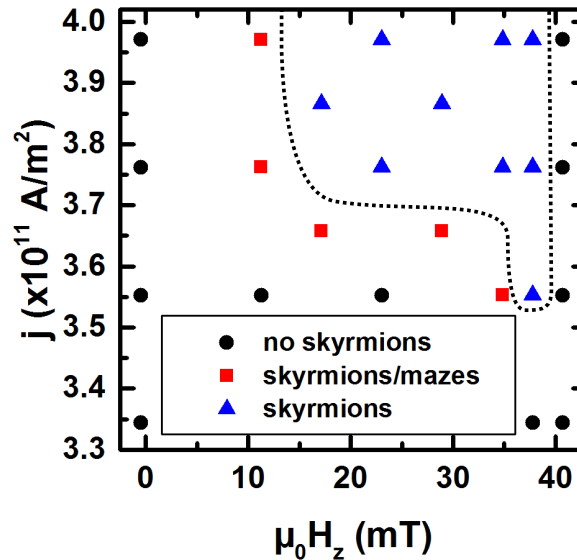
Figure 6.8. – Phase diagram for skyrmion generation determined from the measurements presented in figure 6.7. The dotted line represents a guide indicating the parameter range suitable for skyrmion nucleation.

6.3.2. Skyrmion annihilation

While the measurements of figure 6.6 and 6.7 were performed, it was noticed that above a certain magnetic field the maze domains and skyrmions were erased as the MFM tip scans across them. Therefore, after the pulse was applied for the skyrmion nucleation the magnetic field was reduced. The explanation for this is the confined stray magnetic field around the tip apex which adds to the applied magnetic field (both are in the same direction in the experiments) resulting in a total field (applied field + stray field of the tip, see figure 6.9a) that exceeds the annihilation magnetic field for the maze domains and the skyrmions. This mechanism can be exploited as an annihilation procedure for single skyrmions [148,149] by controllably scanning the MFM tip across this skyrmion. This allows to controllably reduce the number of skyrmions inside the microstripe.

An example of this annihilation mechanism is presented in figure 6.9. Initially skyrmions were nucleated using the nucleation parameters j = 3.97×10^{11} A m^{-2} and $\mu_0 H_z = 23.05$ mT. After the nucleation pulse the magnetic field was reduced to 11.2 mT. In the overview MFM measurement shown in figure 6.9b 11 nucleated skyrmions can be seen in the microstripe. To annihilate single skyrmions the scanning area was reduced, so that the MFM tip scanned over a reduced area with just one skyrmion (the skyrmion marked with the white arrow in figure 6.9b). The first reduced area scan was per-
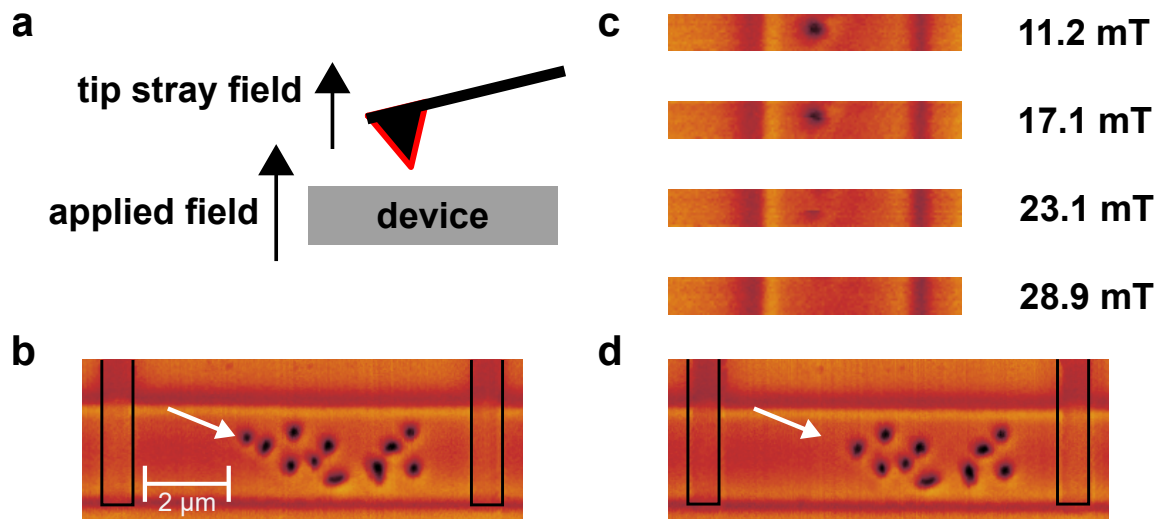
Figure 6.9. – Controllably skyrmion annihilation in the microstripe. **a**, schematic representation of the magnetic fields from the tip and the applied magnetic field to the device. **b**, MFM measurement of skyrmion nucleation of 11 skyrmions in the microstripe with the nucleation parameters j $= 3.97 \times 10^{11}$ A m^{-2}, $\mu_0 H_z = 23.05$ mT. The white arrow marks the skyrmion that is going to be deleted. **c**, MFM measurements during the deletion process for different applied magnetic fields. **d**, MFM measurement after the single skyrmion was deleted.

formed for a magnetic field of 11.2 mT. Before the next reduced area scan the applied magnetic field was increased (see figure 6.9c). When the magnetic field reached a value of ≈ 23 mT the MFM contrast of the skyrmion was strongly reduced. When exceeding this magnetic field the skyrmion was eventually annihilated from the microstripe (scan for a magnetic field of ≈ 28 mT). This means that when the applied magnetic field exceeds 23 mT, the total local field under the MFM tip is greater than the annihilation field, which can be estimated to be between 50 mT and 60 mT according to the measurements from figure 6.4a. After the skyrmion is annihilated, the applied magnetic field can be reduced again to its initial value (11.2 mT) and the scan size can be increased again. The overview MFM measurement after the annihilation process is shown in figure 6.9d, it can be seen that in the reduced scanning area the skyrmion is not present anymore in the microstripe while the other skyrmions were not influenced by this annihilation process. This methodology represents a reliable procedure to define the number of skyrmions inside the microstripe, a prerequisite for the following study of the ANE of small numbers of skyrmions.

6.4. ANE as a function of number of skyrmions in the microstripe

The experimental setup described in chapter 3 section 3.4.3 allowed to simultaneous measure the thermoelectrical voltage due to the ANE and perform in-situ MFM measurements. This allowed to measure the ANE voltage response as a function of the number of skyrmions inside the microstripe but could be also used to study other type of magnetic domains and together with their ANE voltage response. In the experiments, the ANE voltage was recorded after the current pulse for the skyrmion nucleation was applied. Additionally, the device was allowed to regain thermal equilibrium after activating he joule heating of the heater. This was performed to avoid a cross talk signal coming from the pulse in-to the ANE voltage signal, and to avoid drifts in the acquired signal due to heating. Similar studies were performed by [144] were the thermoelectrical signal of a single domain wall in a nanowire was recorded and the position of the domain wall precisely measured with an MFM, and also [28] were by means of the anomalous Hall effect single skyrmions were detected in a microstripe.

In the experiments three independent skyrmion nucleation sequences were performed. For each sequence the single and multiple skyrmions were annihilated using the MFM tip until no skyrmion was left in the microstripe. The MFM measurements are shown in figure 6.10 for each nucleation and annihilation sequence. The nucleation parameters were: j $= 3.97 \times 10^{11}$ A m^{-2} at $\mu_0 H_z = 34.845$ mT, j $= 3.97 \times 10^{11}$ A m^{-2} at $\mu_0 H_z = 34.845$ mT and j $= 3.86 \times 10^{11}$ A m^{-2} at $\mu_0 H_z = 34.845$ mT in the measurements of figure6.10a,b and c respectively. For each sequence the first image from the left shows the MFM measurement performed directly after the skyrmion nucleation process, and the images following to the right show subsequent MFM measurements of consecutive annihilation steps. In the particular case of sequence 2 the applied magnetic field in the deletion process was increased to more than 30 mT which caused a multiple annihilation process as shown in the first and second MFM measurement from figure 6.10b. In the other sequences the maximum number of skyrmions erased in one annihilation step was two.

The ANE signal form the skyrmion configurations shown in figure 6.10 is plotted in figure 6.11. The red dots, black squares and blue triangles correspond to the sequences 1 to 3, respectively. Here, ANE voltage data were acquired over a period of 300 s and a integration time of 30 ms for each point, so that every data point presented in the graph represents the average of more than 10000 measurements and the error

sequence 1
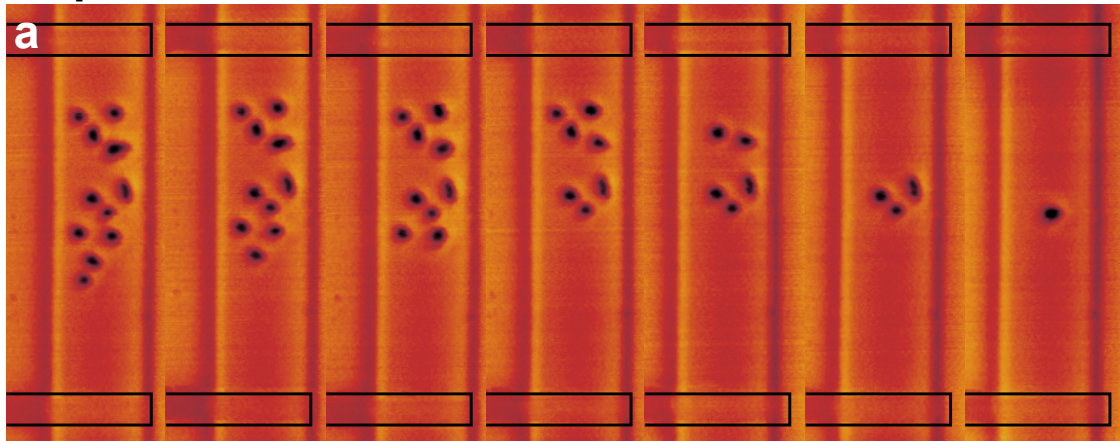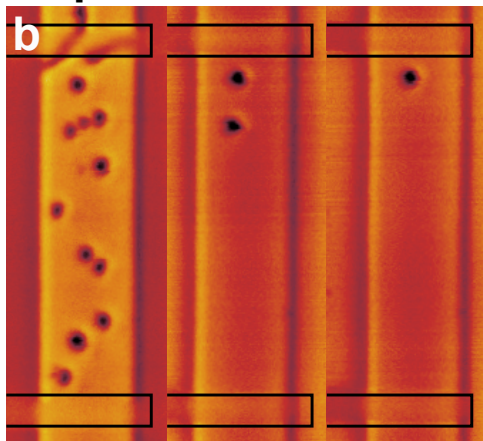
sequence 2   **sequence 3**
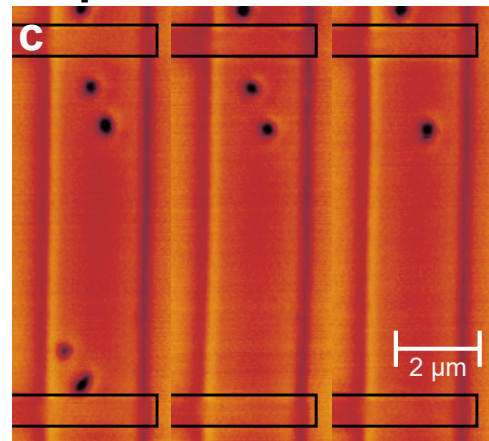
Figure 6.10. – MFM measurements of three independent skyrmion nucleation and annihilation sequences. From left to right the skyrmion number inside the contact area in the microstripe is reduced. a-c, nucleation parameters: $j = 3.97 \times 10^{11}$ A m^{-2} at $\mu_0 H_z = 34.845$ mT, $j = 3.97 \times 10^{11}$ A m^{-2} at $\mu_0 H_z = 34.845$ mT and $j = 3.86 \times 10^{11}$ A m^{-2} at $\mu_0 H_z = 34.845$ mT, respectively.
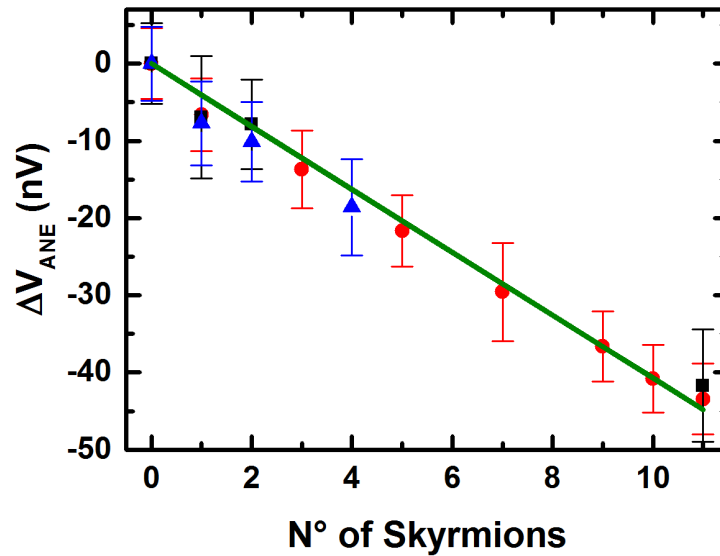
Figure 6.11. – ANE signature of individual skyrmions between the contacts in the microstripe. The red dots, black squares and blue triangles correspond to the sequences 1 to 3 respectively from figure 6.10. The green line is a linear fit through the data, yielding an average ANE signature of 4.07 ± 0.07 nV per skyrmion.

bars display the standard deviation. In the graph, ΔV_{ANE} represents the difference of the measured ANE voltage signal for a given number N of skyrmions $\Delta V_{\mathrm{ANE}}(N)$ and the ANE voltage value when the magnetization is saturated $V_{\mathrm{ANE}}^{\mathrm{sat}}$ ($\Delta V_{\mathrm{ANE}}(N) = V_{\mathrm{ANE}}(N) - V_{\mathrm{ANE}}^{\mathrm{sat}}$). For zero skyrmions in the device, the difference signal vanishes, $\Delta V_{\mathrm{ANE}}(0) = V_{\mathrm{ANE}}(0) - V_{\mathrm{ANE}}^{\mathring{s}at} = 0$ by definition. The data points obtained show a good linear behavior but to emphasize their linear dependence the data points were fitted by linear regression with zero interception (green line in figure 6.11). By performing this linear fit, it is supposed that all the skyrmions contribute equally to the ANE, i.e., that they have the same net magnetization. The linear fit leads to an ANE voltage signature per skyrmion of $V_{\mathrm{ANE}}^{s\mathring{k}y} = 4.07 \pm 0.07$ nV.

6.5. Skyrmion magnetization area

Equation 6.1 shows that the ANE voltage is proportional to the average out-of-plane magnetization (M_{z}) of the area between the two measurement contacts. The magnetic structure outside the contacts does not contribute. From the measurements shown

in figure 6.10 and figure 6.11 it can be seen, that each skyrmion contributes to the measured ANE voltage. Each skyrmion comprises an area of reversed magnetization (magnetization area) and thus reduces the total magnetization in equation 6.1 and therefore the ANE voltage. However, the MFM images show, that the skyrmions have different sizes and thus different effective reversed magnetization area. Therefore, each skyrmion may contribute differently to the net ANE voltage signal. For this reason, it is necessary to develop an analysis approach technique that allows to estimate the skyrmion magnetization profile. Here, an approach is discussed that allows to calculate the spatially resolved M_z profile of the skyrmions from calibrated MFM measurements and thus to calculate the out-of-plane effective reversed magnetization area that contributes to the ANE signal. In the following, the term effective perpendicularly magnetized skyrmion area, A_{sky}, refers to the purely out-of-plane magnetized equivalent area that would have the same net out of plane magnetic areal moment as the skyrmion $A_{sky} \cdot M_s = \int_{\text{stripe area}} M_{z,sky(x,y)} da$.

The MFM measurements depict the cantilever phase shift $\Delta\phi$ when scanning the stray field of the skyrmions and device at a distance of z = 220 nm (lift height + cantilever oscillation amplitude) from the device surface. If a cross-section along one axis of one skyrmion is taken, the phase shift as a function of the lateral distance is obtained as is shown in figure 6.12. These data can be fitted with a Gaussian function (red line in figure 6.12) and the fit reveals a good agreement with the data. Such good agreement was also found in the other cross sections obtained from different MFM measurements of skyrmions. For full analysis all skyrmion phase shift images where fitted with a 2D gaussian. The fitting smoothes the noisy phase shift data and reduces the skyrmion measurement data to a set of 6 parameters that are later used for the determination of the effective out-of-plane area. The Gaussian function used was the following:

$$
\begin{aligned}
G\left(x,y\right) = B \times exp\bigg\{ &- \bigg[\frac{\left[\left(x - x_c\right)\cos\theta - \left(y - y_c\right)\sin\theta\right]^2}{2\sigma_x^2} \\
&+ \frac{\left[\left(x - x_c\right)\sin\theta + \left(y - y_c\right)\cos\theta\right]^2}{2\sigma_x^2} \bigg]\bigg\}
\end{aligned}
\tag{6.2}
$$

where x_c and y_c are the center position of the Gaussian, σ_x and σ_y control the width of the Gaussian bell, B is the amplitude of the Gaussian bell and θ is an in-plane rotation angle. The fit model allows for elliptical skyrmions with an in-plane rotated long axis. This is an advantage since in the MFM measurements it is observed that the skyrmions

are not perfectly round, which is a common feature in similar material systems and experiments [28, 149–151].
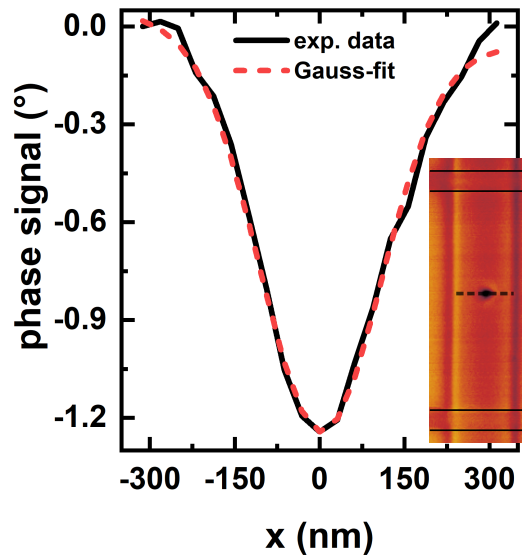
Figure 6.12. – Gaussian fit of the MFM phase signal. MFM measurement and its correspondent x cross-section (black line). The Gaussian fit data is showed in the red line.

To relate the Gaussian fit parameters to the A_{sky} of the skyrmion, the MFM imaging process was analyzed and the skyrmion magnetization was modelled with micromagnetic simulations.

MFM does not measure the skyrmion magnetization but rather the emerging stray magnetic field. Additionally, the finite tip volume leads to a broadening of the MFM signal. To take this into account, a simulated MFM phase signal of the stray field distribution of a typical skyrmion in these types of multilayers used in the device was simulated. The simulated MFM phase signal can then be fitted with the same Gaussian function as used for the experimental data. Furthermore, the effective magnetization area of the skyrmion and the result of the Gaussian fit of the simulated MFM phase signal can be compared so that a criterium for the skyrmion size as a function of sigma can be deduced. The procedure to obtain the simulated MFM signal and the cut-off criterium is explained in detail, next for one typical cross-section of the skyrmion.

Micromagnetic simulations of a typical skyrmion were performed in a collaboration by William Legrand from CNRS/Thales. The simulations were performed according to [61]. The following experimental parameters used in the device were included in the

124

simulations: exchange constant $A = 10$ pJ m^{-1} obtained from domain wall profile as imaged by Lorentz TEM, Dzyaloshinskii-Moriya interaction (DMI) constant $D = 1.19$ mJ m^{-2} determined with Brillouin light scattering spectroscopy, saturation magnetization $M_s = 1100$ kA m^{-1} and perpendicular anisotropy constant $K_u = 1109$ kJ m^{-3} determined by SQUID measurements. The magnetization components of the simulated skyrmion are depicted in figure 6.13 as a function of the skyrmion radius (r). The figures show only half of the skyrmion since in the simulation the skyrmion is symmetric and round. In the simulations, the individual layers (marked in figures 6.13a and 6.13b) in the multilayer stack are modeled and the role of the internal dipolar field is considered. The model is also able to determine the layer-by-layer chirality of the skyrmions and the stray field produced by each layer. This change in chirality is shown in figure 6.13b, were the radial magnetization component of the skyrmion (m_r) inverts its signs from layer 1 (black line) to layer 9 (green olive line). The influence of the inversion of the sign in m_r is shown in more detail in figure 6.13c (for layer 1 and layer 9) were the arrows represent the local magnetization direction along the x-axis. For layer 1, the magnetization vector in the x-z plane rotates as a Néel wall [152]. For layer 9, the magnetization vector rotates mostly in the y-z plane as a Bloch wall [152]. This change in chirality is taken into account in the calculation of net stray field distribution of the skyrmion.

The net stray field distribution of the skyrmions was calculated using the magnetization componenets of the simulated skyrmion (figures 6.13a and figure 6.13b) and the equation 3.11 introduced in chapter 3. To this end, the stray field contributions of all layers were summed up, considering their different z-positions in the multilayer. The procedure to obtain a simulated MFM signal of the simulated skyrmion was based on the tip transfer function approach (TTF) described in chapter 3 section 3.3.2. As discussed above, the net stray field of the skyrmion was calculated from the magnetization distribution resulting from the micromagnetic simulations. In particular, the stray field at the measurement distance z = 220 nm can be calculated. The such obtained stray field H_z (z = 220 nm) from the magnetization shown in figures 6.13a and 6.13b is depicted as the red line in figure 6.14a. Then, to obtain the simulated MFM image, the stray field information of the skyrmion needs to be convoluted with the tip transfer function (TTF) that describes the experimental MFM tip properties (equation 3.24 chapter 3). This TTF was then obtained by measuring a well characterized Co/Pt reference sample with a similar MFM tip as used in the experiments described above (same production badge). Since the MFM tip was not the same as the one from the measurements, the analysis that was performed aimed at obtaining the shape of the
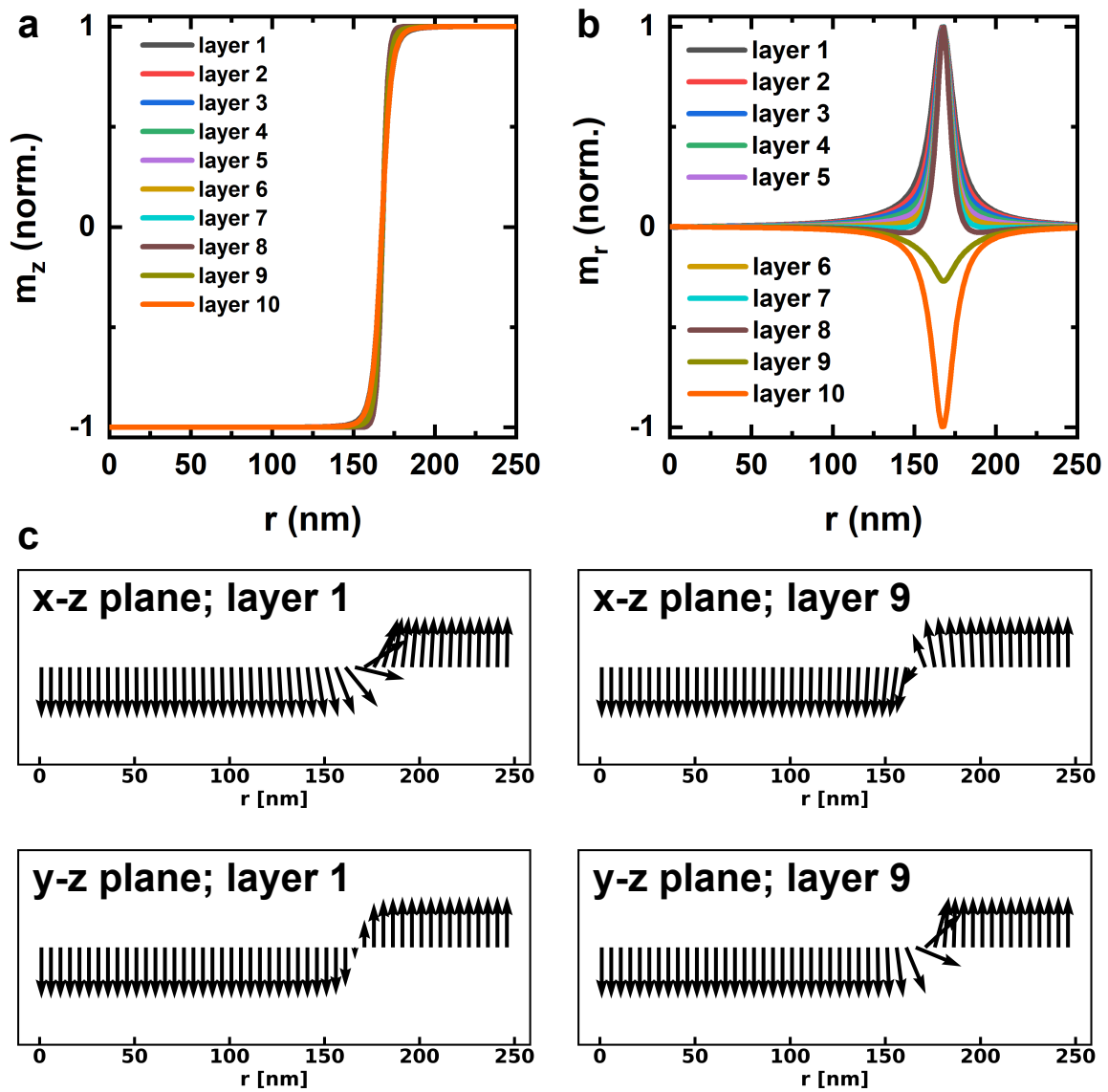
Figure 6.13. – Magnetization components of the simulated skyrmion. **a**, the z component of the magnetization for all the layer of the simulated skyrmion as a function of its radius. **b**, the radial component of the magnetization for all the layer of the simulated skyrmion as a function of its radius. **c**, magnetization vector (represented by arrows) along the x-axis for the x-z plane and y-z plane from layer 1 and layer 9.

126

TTF rather than the amplitude, to analyze its broadening effect on the stray field distribution, thus the TTF units are arbitrary. The used TTF after removing noise contributions is shown in figure 6.14a as the black line. Notice that the TTF is not symmetric (since the tip is not symmetric and canted), therefore the cross-section along two perpendicular directions also for the simulated skyrmion would be different.
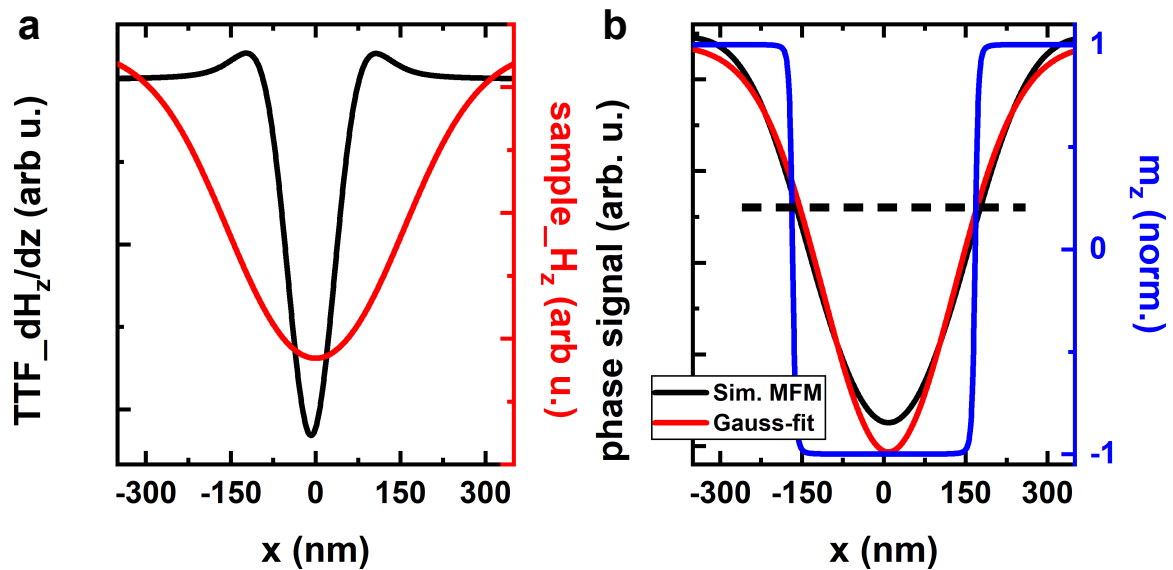
Figure 6.14. – Effective skyrmion magnetization area. **a**, stray field of the skyrmion (red line) and the stray field gradient of the TTF (black line). **b**, x cross-section through the simulated MFM phase data (black line) from a micromagnetic simulated skyrmion, Gaussian-fit data (red line) and the m_z component of layer 1 of the skyrmion used in the simulations (blue line). Dashed black line indicates the cut off criterium used to calculate the skyrmion area representing $\sqrt{2}\sigma$.

By convoluting the stray field of the skyrmion with the TTF a simulated MFM phase signal in arbitrary units is obtained, which is shown as the black line in figure 6.14b. This signal is then also fitted by the Gaussian function of equation 6.2, and the result is depicted in figure 6.14b as the red line. The Gaussian fit reflects the simulated MFM signal quite well, as it is the case for the experimentally obtained data.

The next step is to find a functional relation between the simulated MFM signal, represented by its Gaussian fit, and A_{sky}. This is done by defining a cut-off criterium from a comparison of their spatial distributions. Since the skyrmion magnetization in the z-direction is plateau-like and shows sharp transitions between the skyrmion and outer area (blue line in figure 6.14b), A_{sky} is well described by the plateau area and

its border lies within the sharp transition zone at a distance r_{sky} (skyrmion radius) from the skyrmion center. It can be seen in figure 6.14b that at r_{sky} the Gaussian fit describing the effective magnetic field of the skyrmion has decayed to $\approx 46\ \%$ of the maximal amplitude of the Gaussian. The resulting relationship of the r_{sky} in terms of the sigma of the Gaussian fit obtained is $r_{\mathrm{sky}} \approx \sqrt{2}\sigma$, as illustrated by the dashed line in figure 6.14b. The same analysis was also performed along another cross-section obtaining similar results. The effective area of the skyrmion can be then calculated using the relationship $A_{\mathrm{sky}} \approx 2\pi\sigma_{\mathrm{x}}\sigma_{\mathrm{y}}$.
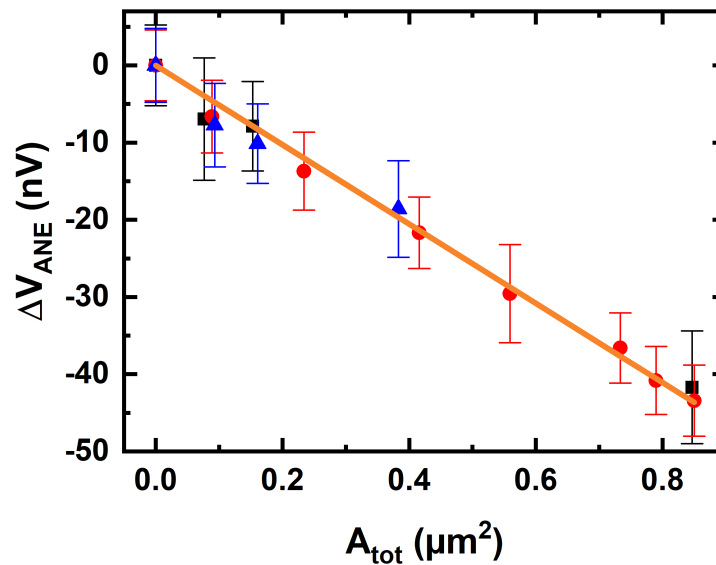
Figure 6.15. – ANE voltage as a function of the total magnetization area A_{tot}. The different symbols correspond to three nucleation/annihilation sequences of figure 6.10. The orange line represents the expected ANE voltage calculated for the given total magnetization area.

The cut-off criterium can then be applied to the experimental MFM data of all skyrmions. As an example, the measurement shown in figure 6.12 of the single skyrmion in the microstripe, results in a skyrmion radius of ≈ 167 nm which translates to a magnetization area of approximately $\approx 0.09\,\mathrm{\mu m}^2$. The three nucleation and annihilation sequences can be analyzed and the total reversed magnetization of the skyrmions $A_{\mathrm{tot,n}} = \sum_{i=0\,1}^{n} A_{\mathrm{sky},i}$ summed over all n skyrmions inside the microstripe can be calculated. Now the x scale of figure 6.11 can be changed from the number of skyrmion to the sum of the effective perpendicularly magnetized skyrmion areas, A_{tot} and the resulting dependency of the measured ANE voltage is shown in figure 6.15. The expected linear behavior of the ANE equation 6.1 is confirmed. The expected ANE voltage signal can be calculated,

128

considering the heating parameters, using the estimated N_{ANE} and the total reversed skyrmion area A_{tot}. The expected ANE voltage signal is shown as the orange line in figure 6.15 an it demonstrates the very good description of the signal by the ANE response of the reversed magnetization area of the skyrmions.

6.6. Skyrmion area as a function of the magnetic field

The size of the skyrmions can be influenced by many factors ranging from the parameters of the material that hosts the skyrmions to the applied magnetic field [153]. For the particular case of the magnetic field which serves to stabilize the skyrmions, theoretical and experimental studies have shown that the radius of the skyrmion (or its area) reduces as the applied magnetic field increases [29,59,61,154–157]. The skyrmion shrinks until a certain magnetic field is reached and then it collapses. At the critical magnetic field the energy barrier which stabilizes the skyrmion breaks resulting in a collapse of the skyrmion [59,154].

This size-magnetic field dependence of the skyrmions can be confirmed from the measurements performed in this study. In the last MFM measurement of each nucleation/annihilation sequence shown in figure 6.10, there is just one skyrmion left in the microstripe.

In similar manner as described in section 6.3.2 the last skyrmion from each nucleation sequence was annihilated from the microstripe only that in this case the complete microstripe area was scanned and not just locally over the skyrmion. The MFM measurements of this procedure are shown in figure 6.16a-c, where a-c corresponds to the nucleation/annihilation sequences of figure 6.10 respectively. In the measurements as the magnetic field increases the size of the skyrmion is reduced until the skyrmion is annihilated. The skyrmion annihilation field was above $\approx$ 23 mT reproducing the same result as for the skyrmion annihilation shown in section 6.3.2. However, even at magnetic fields of 17.16 mT the MFM tip starts to interact with the skyrmions, as can be seen across the measurements, where the MFM phase signal starts to become blurred.

Following the skyrmion magnetization area calculation approach explained in section 6.5, the skyrmion magnetization area A_{sky} for the different magnetic fields can be obtained from of the MFM measurements of figure 6.16. The results are depicted in
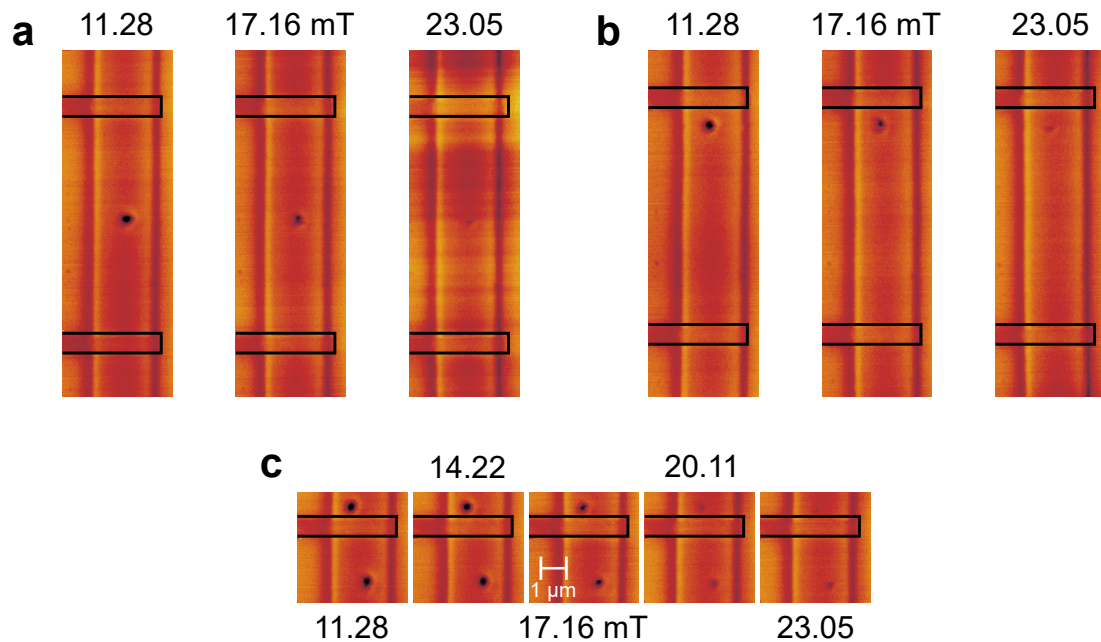
Figure 6.16. – MFM measurements of one single skyrmion as a function of the applied magnetic field. **a** - **c**, the single skyrmion in the measurements is obtained after the nucleation and annihilation procedure of the sequences in figure 6.10 respectively. From left to right the magnetic field is increased until a magnetic field value of ≈ 28 mT is reached which causes the skyrmion annihilation with the MFM tip.

figure 6.17a where A_{sky} of each skyrmion for the different sequences is depicted as a function of the applied magnetic field. Before increasing the magnetic field, the skyrmions of each sequence have different magnetization areas. As the magnetic field increases the area decreases as expected. Overall an almost linear decrease of the skyrmion area with field is found albeit in the presence of a significant stray of the data.

The ANE voltage was measured between each MFM scan for all sequences and magnetic fields. The ANE voltage measurements are depicted in figure 6.17b as a function of the magnetization area. They confirm the expected behavior, as the magnetization area of the single skyrmion is reduced so does the ANE voltage. The orange line shows the calculated ANE signal and describes well the single skyrmion data within the experimental measurement uncertainty. This shows that the ANE is not only sensitive to detect single skyrmions but also to their size change which in this case is caused by the applied magnetic field.
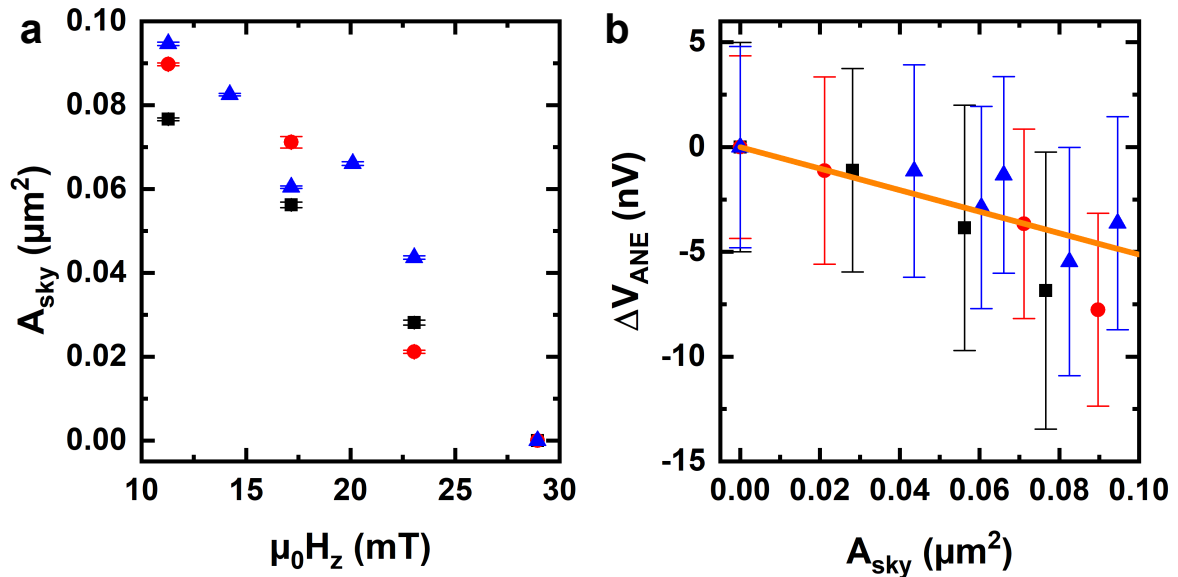
Figure 6.17. – Magnetization area of one single skyrmion as a function of the applied magnetic field. Here the red dots, black squares and blue triangles correspond to the MFM measurements showed in figure 6.16a-c respectively. **a**, skyrmion magnetization area calculated from the MFM measurements as a function of the applied magnetic field. **b**, the ANE voltage measured for each skyrmion state in a, as a function of the skyrmion magnetization area. The orange line represents the expected ANE voltage calculated for the given total magnetization area.

6.7. Influence of non-uniform thermal gradient and skyrmion position on the ANE signal

In section 6.2 the thermal gradient distribution was shown according to the results obtained from the COMSOL simulations. It was concluded that the gradient along the x-direction is higher in amplitude compared to the other directions and therefore has the biggest contribution to the measured ANE voltage. Also, in section 6.2 for the calculation of the Nernst coefficient, the thermal gradient used in the calculation was obtained from the COMSOL simulations by taking an average thermal gradient along the x direction. In the ANE voltage measurements as a function of the magnetization area of the skyrmions it was assumed that every skyrmion senses the amplitude of the average thermal gradient obtained from the simulations which explains in good agreement the experimental data obtained in the ANE measurements (orange line in figure 6.15). However, the COMSOL simulations indicate that the thermal gradient changes

its amplitude along the x direction, as shown in detail in figure 6.18a. According to the simulations the thermal gradient changes inside the microstripe in a range from 6 $K \, \mu m^{-1}$ to 0.5 $K \, \mu m^{-1}$. This would lead, according to equation 6.1, to an ANE voltage that depends on the x-position of the skyrmions. A skyrmion positioned on the side of the microstripe nearby the heater would contribute to the total voltage three times more than another skyrmion that is positioned further apart, even if they have the same size. In this section this issue is addressed by calculating the voltage contributions of single skyrmions taking in to account the local thermal gradient according to their position in the microstripe using the COMSOL simulations and compare the result to the measured ANE voltage.

With the use of the thermal gradient from the COMSOL simulations an estimate of the upper limits of the uncertainty of the simulated data, complemented with possible error contributions from the calculated skyrmion area were used to obtain the calculated voltage, taking in to account the following: For each skyrmion an effective local thermal gradient was obtained by averaging over its area using the spatially resolved data from COMSOL simulations with an assumed error of 10% due to position and shape inaccuracies. Additionally, an error is allowed in the calculation of the skyrmion area.

To this end, we assumed an error in the relationship between the σ of the fitted Gaussian and the effective skyrmion radius ($r_{sky} \approx \sqrt{2}\sigma$) of more than 12% ($r_{sky} \approx \sqrt{2 \pm 0.25}\sigma$). In figure 6.18b it is shown how the effective skyrmion radius is affected by changing the cut-off criterium obtained in section 6.5. The ANE voltage for every single skyrmion in this specific approach can be calculated using the following equation:

$$V_{ANE} = -N_{ANE}\mu_0 M_z \overline{\nabla T_{x;local}} A_{tot}/w \tag{6.3}$$

where $\overline{\nabla T_{x;local}}$ represents the local average thermal gradient and $w = 2 \, \mu m$ the width of the microstripe. The other parameters were already described in section 6.2 and section 6.5. In figure 6.18c is shown the comparison between the measured ANE voltage from the sequence shown in figure 6.10a depicted as the red dots and the simulated ANE voltage. Taking into account the above discussed error margins leads to a range of possible simulated ANE values that is shown here as a gray shadowed area. We attribute the fact that the gray area it mostly found at higher negative ANE values than the experimental data to an overestimation of the thermal gradient in the COMSOL simulations due to effects like the idealized square shape of the microstripe in the simulation. Examples of this overestimation are visible in the figure 6.18a, where near
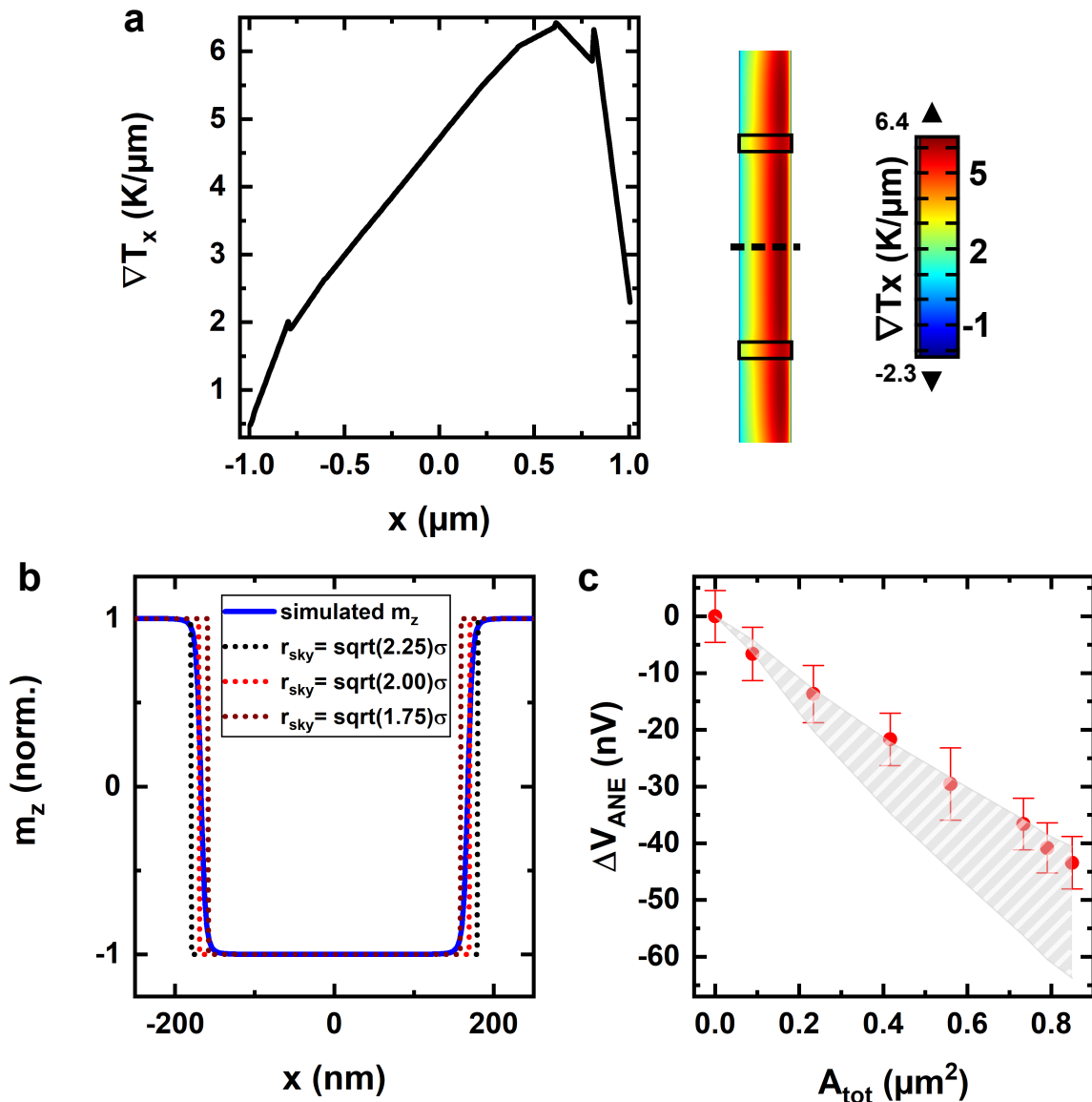
Figure 6.18. – **a**, cross-section of the temperature gradient along the x direction. The colormap represents the temperature gradient distribution along the x axis of the mircostripe. **b**, the m_z component of the skyrmion used in the simulations (blue line), the different dotted lines represent the radius calculated by $r_{sky} \approx \sqrt{x}\sigma$ where x is the relation that is obtained by comparing the simulated MFM image with the m_z component of the skyrmion. **c**, measured ANE voltage as a function of the total effective reversed area (red dots) obtained from the nucleation and annihilation sequence depicted in figure 6.10a. The gray area depicts the calculated ANE voltage taking in to account the different positions of the skyrmions and its correspondent temperature gradient according to the COMSOL simulations including an error and the influence of the calculated magnetization area.

133

the edges of the microstripe the value of the thermal gradient increases or decreases drastically making the thermal gradient highly inhomogeneous. Also, two spikes appear ≈ 200 nm away from the edges of the microstripe which could appear due to a cell mismatch in the simulations due to the steep edges of the assumed perfectly square shape microstripe.

6.8. Topological Nernst effect in Pt/Co/Ru multilayers

When spin polarized electrons transverse a topological non-trivial spin texture, such as a magnetic skyrmion, they can accumulate a Berry phase [158]. This Berry phase can be viewed analogous to a Aharonov-Bohm phase resulting from a fictious magnetic field antiparallel to the uniform magnetization [159]. In other words, this can be understood as an emergent magnetic field which acts on the electrons crossing the skyrmion. This causes the electrons to deflect in direction perpendicular to their motion and the emergent magnetic field, similar as the Lorentz force. Experimentally this accumulated Berry phase can result in a topological Hall effect (THE) as was demonstrated for Bulk MnSi [16]. In the case of multilayer systems hosting skyrmions at room temperature it is still under discussion if the Hall signature obtained from single skyrmions shows a THE related contribution [31, 160]. Previous Investigations show that the Hall signature of one single skyrmion can be well explained by its anomalous Hall effect signature and that in these multilayers systems the topological contribution is much smaller than the anomalous Hall effect contribution [28, 29].

There have been studies concerning the topological Nernst effect (TNE), which include observations in bulk MnGe where a value of the TNE was reported [34]. In contrast for bulk MnSi due to the measurement uncertainty the TNE could not be observed [35]. More recently a TNE contribution was found in Mn1.8PtSn micropatterned thin films [36] and the presence of an TNE in bulk MnSi [34]. But the presence of an TNE in multilayer thin films at room temperature has not been addressed. In the following an analysis is presented to extract a possible topological contribution from the measurement data in the sections above.

In the measurements shown in sections 6.5 and 6.6 the ANE voltage data scale with the magnetization area as can be expected from the ANE assuming no TNE contribution. When a contribution due to the TNE is assumed, the total measured voltage ($V_{\text{total}} = V_{\text{ANE}} + V_{\text{TNE}}$) should consist of a summation of two effects: the ANE that scales with

134

the magnetization area as explained in equation 6.1 and the TNE that should scale with the total topological charge of the skyrmions [31, 71]. In the multilayer system studied, in principle, each skyrmion should carry the same topological charge ξ_{top} independent of the exact surface area. Therefore, the voltage due to the TNE should scale with the number n of skyrmions between the contacts in the microstripe, like $V_{\text{TNE}} = \text{n}\xi_{\text{top}}$ and not with their net area $A_{\text{tot,n}}$. Thus, in the presence of significant V_{TNE} the total measured thermovoltage signal $V_{\text{total,n}} = V_{\text{ANE}}(A_{\text{tot,n}}) + \text{n}\xi_{\text{top}}$, should not be proportional to $A_{\text{tot,n}}$. Under this assumption if this contribution has a significant impact in the measurements, directly in the measurements of figure 6.15 and figure 6.17b the values obtained for ΔV_{ANE} should show a tendency towards a non-zero value (since V_{TNE} contributes to the total voltage) resulting in an offset. This offset should correspond to the topological contribution of one single skyrmion to the measured voltage. However, such offset is not be observed within the measurement noise level.

If the Nernst effect and Hall effect behave similarly in these type of multilayer systems the ANE should be the mayor contributor to the measured voltage, same as the anomalous hall effect in other investigations [28, 29]. Then, the contribution due to TNE is obscured due to the ANE.
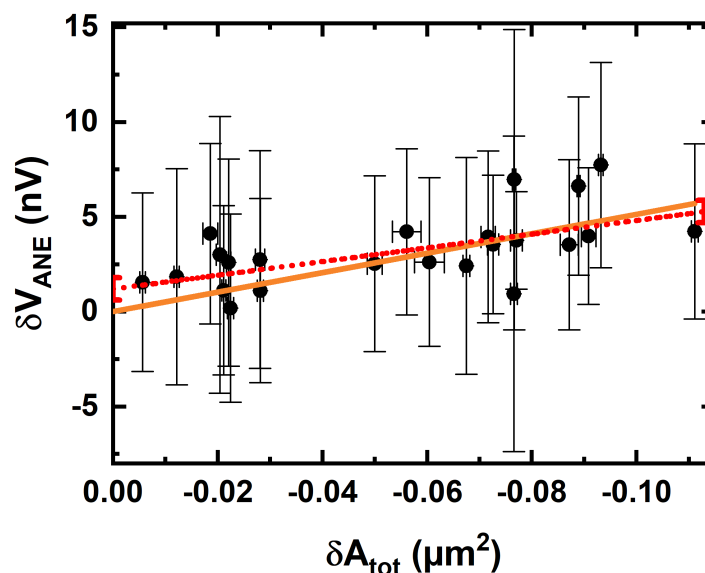
Figure 6.19. – Change of the ANE voltage due to the change of the skyrmion number by one. δV_{ANE} is plotted as function of the reversed area difference. Orange line is the predicted ANE signal considering the reversed area of A_{tot}. The red dotted line is linear fit of the data allowing for a non-zero intersection.

A possible voltage contribution due to the TNE (V_{TNE}) from the measurements could be obtained by fitting the obtained data with a linear fit and obtaining the offset value. In the combined measurements of ANE and MFM the changes due to one or two skymrions are precisely known in our system. For this reason, from the measured data it is possible to extract the voltage change due to the change of the number of skyrmions (topological charge). First, the voltage change is calculated $\delta V_{\mathrm{ANE,n}} = \Delta V_{\mathrm{ANE,n+1}} - \Delta V_{\mathrm{ANE,n}}$ being the change of $\Delta V_{\mathrm{ANE,i}}$ when changing the number of skyrmions (and thus the topological charge of the system) by one. Second the magnetization area changes for each change in the skyrmion number $\delta A_{\mathrm{tot,n}} = -A_{\mathrm{tot,n}} - A_{\mathrm{tot,n-1}}$ are calculated. This allows to separate V_{ANE} and V_{TNE} contributions since:

$$\delta V_{\mathrm{ANE,n}} = -N_{\mathrm{ANE}}\mu_0 \overline{\nabla T_x} 2 M_{\mathrm{s}} \delta A_{\mathrm{tot}}/w + 1 \cdot \xi_{\mathrm{top}} \tag{6.4}$$

and thus ξ_{top} can be separated as an offset. The width of the microstripe is represented here with w. Figure 6.19 shows $\delta V_{\mathrm{ANE,n}}$ as a function of $\delta A_{\mathrm{tot,n}}$ for all datasets in the study performed. In the absence of δA_{tot}, δV_{ANE} should be zero when no TNE is considered, this is described by the orange line in figure 6.19 showing no offset. If a free linear fit is considered in the data (red dotted line in figure 6.19) a small nonzero intercept at zero δA_{tot} is observed (an offset). The presence of a nonzero intercept could indicate a potential topological contribution V_{TNE} to the skyrmion Nernst signature independent of A_{tot}. The derived interception of 1.2 ± 0.6 nV is approximately 4 times smaller than the ANE contribution per skyrmion, but different from zero value within 2σ confidence. Based on this analysis, the topological contribution cannot be ruled out. But, considering the statistical uncertainty of the data presented, further studies are required to unambiguously conclude on the nature of the topological Nernst signature of individual skyrmions.

One possible explanation why the topological contribution of the skyrmions has a small value in the multilayer systems could be the small electron mean free path and the spin diffusion length with respect to the skyrmion´s size in multilayers [28, 29]. These two parameters and the large charge-carrier density of the metallic systems should result in a drastic reduction of the topological contribution term of skyrmions due to scattering. In the metallic multilayers studied here the same case appears, both the electron's mean free path and the spin diffusion length are of the order of few nanometers [161, 162] and thus significantly smaller than the average skyrmion diameter (≈ 160 nm). Also, the skyrmions have a disordered configuration in the multilayers and thus experience an inhomogeneous emergent field, in contrast to bulk

systems which show an ordered arrangement of the skyrmions (skyrmion lattices) [31]. These hypotheses could provide an explanation why in the material system studied no strong topological Nernst contribution is found.

7. Summary and Conclusions

Thermoelectric effects, in particular the anomalous Nernst effect (ANE), were used in this work as a tools to measure and detect individual nano magnetic textures such as domain walls and skyrmions in magnetic micro and nanowires.

The devices fabricated for the thermoelectric measurements consisted of a magnetic wire with adjacent parallel platinum heater stripes. The thermal gradient perpendicular to the wire was generated by means of Joule heating of the heater. The temperature increase at the wire was quantified by temperature resistance measurements and thermal finite element modelling. A thermovoltage was generated at the wire position due to the thermal gradient, and its amplitude was proportional to the average magnetization of the wire.

The new "two-heater" procedure developed in this work presents a technique to separate contributions to the thermovoltage rising from different componentes of the thermal gradients that are unavoidable but need to be separated for proper data analysis. After the calibration of the two heaters used in the methodology, the initial thermovoltage is separated into two components, which only depend on one component of the thermal gradient. The feasibility of this new procedure was demonstrated for a permalloy nanowire in saturation. In the future it could be applied in the area of spincaloritronics, where in some geometries, e.g. the spin Seebeck effect could be affected by unwanted thermal gradients.

The ANE effect was used to detect a single domain wall (DW) in the microwire. The device employed allowed to controllably nucleate a single DW at one end of the microwire, which could be moved from its nucleation position by two mechanism: magnetic field driven and spin-torque driven DW motion. At the same time as the DW was moved, the thermovoltage due to the ANE was recorded. The domain wall position could be obtained by applying a conversion from the thermovoltage measurements to the DW position. The obtained DW position was then verified by magneto optical Kerr effect microscopy. The results obtained show good agreement with the calculated values from

139

the ANE voltage measurements. Small changes in the position of the DW were also detected measuring the ANE voltage where the DW was moved by means of spin-torque. This allowed to detect defects where the DW gets pinned in the microwire, proving the spatial resolution of the measurement technique. Only with reliable techniques and high resolution tools the position of DW pinning centers can be accurately obtained.

In a further part of the thesis, the thermoelectrical signal of individual single skyrmions was experimentally characterized for the first time. The device used in the experiments was characterized and its ANE voltage dependence with the internal magnetization in the microwire was measured using a combination of ANE voltage measurements and magnetic force microscopy (MFM). The controllable nucleation of single skyrmions was performed by applying squared current pulses in the presence of a magnetic field. A small number of skyrmions could be nucleated in the microwire by choosing the right parameters of the current density of the pulse and the magnetic field. Subsequently, the skyrmions were controllably annihilated by using a novel approach employing a highly localized stray magnetic field provided by an MFM tip. This approach allowed to obtain the ANE voltage response as function of the number of skyrmions in the microwire leading to a thermoelectric signature of 4.6 nV per skyrmion. Furthermore, an analysis was performed to obtain the effective skyrmion area from the experimental obtained MFM phase signal of the single skyrmions. This allowed to not only show the ANE voltage as a function of the skyrmion area but also study the skyrmion area as a function of the magnetic field. Using the experimental data obtained from the ANE voltage measurements, an analysis was performed to obtain a possible topological Nernst effect (TNE) contribution. Based on the analysis, a four times smaller contribution in comparison to the ANE was found. Nevertheless, considering the total measurement uncertainty of our data, a TNE contribution cannot be ruled out. Considering the statistical uncertainty of the presented data, further studies are required to unambiguously conclude on the nature of the TNE signature of individual skyrmions.

Concluding, this work showed that by using a thermoelectric effect as the ANE allows for a unique non-invasive detection and counting of domain walls and skyrmions. This adds a new technique to the variety of techniques to detect, characterize and study non-trivial spin structures. Also, it sets a milestone that allows for further fundamental studies of topological thermoelectric effects.

A. Annex 1: Parameters of the clean room processes

According to the device fabrication explained in chapter 2 section 2.1 the fabrication process was divided in two steps, the fabrication of the wires and the fabrication of the heater and contacts. The details on the fabrication are explained next.

A.1. Fabrication of the wires

Cleaning Si-wafer "dummy" and of the magnetic material:

- The dummy is immersed in acetone in an ultrasonic bath, 5 min with power 6.

- The acetone is removed with isopropanol and the dummy is dried with nitrogen.

- The magnetic film is immersed in acetone in an ultrasonic bath, 5 min with power 6. The acetone is removed with isopropanol and the magnetic film is dried with nitrogen.

- Magnetic film is glued with TEM wax to the dummy.

Lift-off process and e-beam lithography:

- Spin coating of PMMA, AR-P 642.04 (Allresist GmbH) on to the wafer. Thickness of the film $\approx$ 106 nm, using 4000 rpm for 45 s.

- Baking of the wafer for 10 min at 160 °C.

- Spin coating of PMMA, AR-P 672.01 (Allresist GmbH) on to the wafer. Thickness of the film $\approx$ 32 nm, using 2000 rpm for 90 s.

- Baking of the wafer for 10 min at 160 °C.

- Exposure with the e-beam at 100 kV an area with a basis dose of 824 µC cm^{-2}.

- Developing using "glasgower" for 60 s. The developer "glasgower" is synthesized by mixing 10.0 mL Ethylmethylketon (MEK), 247.5 mL Methylisobutylketon (MIBK) and 742.5 mL isopropanol.

- The developing process is stopped by immersing the wafer 60 s in isopropanol.

- Al is evaporated at a rate of 0.2 nm s^{-1} at a base pressure of $\approx 2x10^{-6}$ mbar using a standard thermal evaporator. Depending on the thickness of the magnetic layer 50 nm or 60 nm of Al were evaporated.

- Removing the PMMA resist (lift-off) by immersing the wafer in acetone for 2 days. Then the wafer in the acetone is put in an ultrasonic bath, 5 min with power 6. This process removes the TEM wax that glues the magnetic film to the dummy. The acetone is removed with isopropanol and the magnetic film is dried with nitrogen.

Etch process and removing the Al-layer:

- The etching process was performed in an argon atmosphere with a base pressure of $\approx 2.6x10^{-4}$ mbar. The etching time for the permalloy was 8 min and for the Pt/Co/Ru multilayers 17 min. The parameters for the ion source (KDC 40 4-cm dc from Kaufman & Robinson) were:

    - Cathode 7.3 A

    - Discharge 40 V / 0.13 A

    - Beam 600 V / 6 mA

    - Acceleration 100 V / 1 mA

    - Neutralizer 8.2 V

    - Emission 6 mA

    - Argon 6 sccm

- By immersing the magnetic film in a developer (MAD-332 micro resist technology GmbH) for 5 min the Al-layer was removed. The developer is then removed by immersing the magnetic film 2 min in water.

A.2. Fabrication of the heater and contacts

E-beam lithography:

- Magnetic film is glued again with TEM wax to the dummy.

- Spin coating of PMMA, AR-P 642.09 (Allresist GmbH) on to the wafer. Thickness of the film ≈ 420 nm, using 4000 rpm for 45 s.

- Baking of the wafer for 10 min at 160 °C.

- Spin coating of PMMA, AR-P 672.03 (Allresist GmbH) on to the wafer. Thickness of the film ≈ 117 nm, using 4000 rpm for 45 s.

- Baking of the wafer for 10 min at 160 °C.

- Exposure with the e-beam at 100 kV an area with a basis of 941 µC cm^{-2}.

- Developing using "glasgower" for 90 s.

- The developing process is stopped by immersing the wafer 90 s in isopropanol.

Sputtering of the heater and contacts material and removing the resist:

- The sputtering process was performed in an argon atmosphere with a base pressure of ≈ $2.6x10^{-4}$ mbar.

- The parameters for the ion source (KDC 40 4-cm dc from Kaufman & Robinson) for the sputtering process were:

    - Cathode 8.3 A

    - Discharge 40 V / 0.84 A

    - Beam 666 V / 50 mA

    - Acceleration 120 V / 1.7 mA

    - Neutralizer 9 V

    - Emission 50 mA

    - Argon 6 sccm

- First the area where the heater and the contacts where etch for 20 s using the parameters described above in section A.1 in the etch process.

- Before the sputtering of the material the targets were cleaned for 2 min, by continuously sputtering on them. In this thesis two targets were used for the fabrication and Ta target and a Pt target.

- The first material sputtered was Ta with a thickness of 5 nm (sputtering time 1:22 min)

- The Pt target was cleaned again for 1 min.

- The Pt was sputtered with a thickness of 95 nm (sputtering time 13:54 min)

- The resist was removed by immersing the wafer in acetone for 2 days. Then, the wafer in the acetone is put in an ultrasonic bath, 5 min with power 6. This process removes the TEM wax that glues the magnetic film to the dummy. The acetone is removed with isopropanol and the magnetic film is dried with nitrogen.

144

B. Annex 2: COMSOL simulation parameters

The thermal modelling in this thesis was performed using the Joule heating module of COMSOL finite element [134]Ref[1]. The Joule heating module was implemented to estimate the temperature rise and thermal gradient. By using the thermal modelling an estimation of the temperature and the thermal gradient could be obtained for the heater and surroundings in the device topology. The geometries and dimensions of the modeled device match that of the real device. In all simulations the bottom temperature of the substrate (GaAs or Si, depending on the device) was set to ambient temperature according to the temperature in the experiments. Temperature dependent bulk material parameters, e.g. thermal conductivity κ and heat capacity C_p, were taken from different references (marked in the tables).

The temperature coefficient of the resistance in the simulation of the magnetic wire and the heater were calibrated by temperature dependent resistance measurements. These measurements were performed separately for each device.

It is important to mention that, when the materials are in form of thin film, the thermal conductivity might be lower due to additional interfaces. Also, impurities from sample fabrication could lower the thermal conductivity. The simulation thus provides low boundaries of the temperature and temperature gradients.

In table B.1A2.1 (Ga,Mn)(As,P) device) and table A2.2 (Pt/Co/Ru device) the material parameters which were used in the simulations are listed.

Material	C_p ($\mathrm{J\,kg^{-1}\,K^{-1}}$)	ρ ($\mathrm{kg\,m^{-3}}$)	κ ($\mathrm{W\,m^{-1}\,K^{-1}}$)	α ($\mathrm{K^{-1}}$)
GaAs	$C_{p,\mathrm{GaAs}}\,(T)$ [163]	5316	$\kappa_{\mathrm{GaAs}}\,(T)$ [135]	
Pt	$C_{p,\mathrm{Pt}}\,(T)$ [143]	21450		0.0015
(Ga,Mn)(As,P)	$C_{p,\mathrm{GaAs}}\,(T)$ [163]	5316	$\kappa_{\mathrm{GaAs}}\,(T)$ [135]	

Table B.1. – Material parameters used in the COMSOL simulations for the (Ga,Mn)(As,P) device.

Material	C_p ($\mathrm{J\,kg^{-1}\,K^{-1}}$)	ρ ($\mathrm{kg\,m^{-3}}$)	κ ($\mathrm{W\,m^{-1}\,K^{-1}}$)	α ($\mathrm{K^{-1}}$)
Si	$C_{p,\mathrm{Si}}\,(T)$ [139]	2329	$\kappa_{\mathrm{Si}}\,(T)$ [140]	
SiO$_2$	$C_{p,\mathrm{SiO_2}}\,(T)$ [141]	2203	$\kappa_{\mathrm{SiO_2}}\,(T)$ [142]	
Pt	$C_{p,\mathrm{Pt}}\,(T)$ [143]	21450		0.0015
Pt/Co/Ru multilayer	130	8000		$8.7x10^{-4}$

Table B.2. – Material parameters used in the COMSOL simulations for the Pt/Co/Ru device.

List of Symbols

α Gilberts damping parameter

β Molecular magnetic field constant

χ Magentic susceptibility

δA_{pixel} Pixel area

γ Gyromagnetic ratio

$\hat{\sigma}\left(\mathbf{k}\right)$ Effective magnetic charge distribution of the magnetic tip

κ Thermal conductivity

κ_{B} Boltzmann constant

$\mathbf{E}$ Electric field

$\hat{\mathrm{D}}$ Demagnetization tensor

$\widehat{\mathrm{m}}$ Magnetization unit vector

μ_0 Permeability of free space

μ_{B} Bohr magneton

∇T Temperature gradient

∇ Nabla operator

$\overline{\nabla T}$ Average temperature gradient

147

ρ Electrical resistivity

σ Electrical conductivitye

$\mathbf{H}_{\mathrm{D}}$ Stray magnetic field

$\mathbf{H}_{\mathrm{ext}}$ External magnetic field

$\mathbf{J}$ Charge current density

$\mathbf{Q}$ Heat current density

A Exchange stiffness constant

a Azimuthal angle

A_{sky} Skyrmion magnetization area

A_{tot} Total reversed skyrmion magnetization area

b Polar angle

C Curie constant

c Spring constant of the cantilever

D Effective Dzyaloshinskii-Moriya interaction constant

$DW_{position}$ Domain wall position

H Uniform magnetic field

H_{sample} Stray magnetic field of the sample

H_{w} Molecular magnetic field

H_c Coercive magnetic field

I Electrical current

148

$J_{i,j}$ Exchange constant between the two spins

K_c Cubic anisotropy

K_s surface anisotropy

K_u Uniaxial anisotropy

LCF Cantilever correction factor

M Magnetization

M_tip Local magnetic moment of a MFM tip

M_s Saturation magnetization

N_ANE Anomalous Nernst coefficient per magnetic moment

Q Quality factor

S Seebeck coefficient

S_N Nernst coefficient

T Temperature

T_C Curie Temperature

V Volume

v Velocity

V_ANE Anomalous Nerst effect voltage

V_ANE^{sky} Skyrmion anomalous Nernst effect voltage signature

$V_\mathrm{ANE}^\mathrm{max}$ Amplitude of the anomalous Nerst effect voltage

$V_\mathrm{ANE}^\mathrm{sat}$ Anomalous Nernst effect voltage when the magnetization is saturated

V_{max} Maximal amplitude of thermoeletric voltage

V_{thermo} Thermoelectric voltage

V_{TNE} Topological Nernst effect voltage

H1 Heater 1

H2 Heater 2

R Electrical resistance

Bibliography

[1] M. N. Baibich, J. M. Broto, A. Fert, F. Nguyen Van Dau, F. Petroff, P. Etienne, G. Creuzet, A. Friederich, and J. Chazelas. Giant Magnetoresistance of (001)Fe/(001)Cr Magnetic Superlattices. *Physical Review Letters*, 61(21):2472–2475, Nov 1988.

[2] T. McGuire and R. Potter. Anisotropic magnetoresistance in ferromagnetic 3d alloys. *IEEE Transactions on Magnetics*, 11(4):1018–1038, Jul 1975.

[3] I. Žutić, J. Fabian, and S. Das Sarma. Spintronics: Fundamentals and applications. *Reviews of Modern Physics*, 76(2):323–410, Apr 2004.

[4] G. E. W. Bauer, E. Saitoh, and B. J. van Wees. Spin caloritronics. *Nature Materials*, 11(5):391–399, Apr 2012.

[5] P. Krzysteczko, X. Hu, N. Liebing, S. Sievers, and H. W. Schumacher. Domain wall magneto-Seebeck effect. *Physical Review B*, 92(14):140405, Oct 2015.

[6] A. D. Avery, M. R. Pufall, and B. L. Zink. Observation of the Planar Nernst Effect in Permalloy and Nickel Thin Films with In-Plane Thermal Gradients. *Physical Review Letters*, 109(19):196602, Nov 2012.

[7] A. Slachter, F. L. Bakker, and B. J. van Wees. Anomalous Nernst and anisotropic magnetoresistive heating in a lateral spin valve. *Physical Review B*, 84(2):020412, Jul 2011.

[8] E. De Ranieri, P. E. Roy, D. Fang, E. K. Vehsthedt, A. C. Irvine, D. Heiss, A. Casiraghi, R. P. Campion, B. L. Gallagher, T. Jungwirth, and J. Wunderlich. Piezoelectric control of the mobility of a domain wall driven by adiabatic and non-adiabatic torques. *Nature Materials*, 12(9):808–814, Jun 2013.

[9] A. Yamaguchi, T. Ono, S. Nasu, K. Miyake, K. Mibu, and T. Shinjo. Real-Space Observation of Current-Driven Domain Wall Motion in Submicron Mag-

netic Wires. *Physical Review Letters*, 92(7), Feb 2004.

[10] S. Y. Huang, W. G. Wang, S. F. Lee, J. Kwo, and C. L. Chien. Intrinsic Spin-Dependent Thermal Transport. *Physical Review Letters*, 107(21):216604, Nov 2011.

[11] D. Meier, T. Kuschel, L. Shen, A. Gupta, T. Kikkawa, K. Uchida, E. Saitoh, J.-M. Schmalhorst, and G. Reiss. Thermally driven spin and charge currents in thin $NiFe_2O_4$/Pt films. *Physical Review B*, 87(5):054421, Feb 2013.

[12] M. Schmid, S. Srichandan, D. Meier, T. Kuschel, J. M. Schmalhorst, M. Vogel, G. Reiss, C. Strunk, and C. H. Back. Transverse Spin Seebeck Effect versus Anomalous and Planar Nernst Effects in Permalloy Thin Films. *Physical Review Letters*, 111(18):187201, Oct 2013.

[13] D. Meier, D. Reinhardt, M. van Straaten, C. Klewe, M. Althammer, M. Schreier, S. T. B. Goennenwein, A. Gupta, M. Schmid, C. H. Back, J. Schmalhorst, T. Kuschel, and G. Reiss. Longitudinal spin Seebeck effect contribution in transverse spin Seebeck effect experiments in Pt/YIG and Pt/NFO. *Nature Communications*, 6(1):8211, Sep 2015.

[14] O. Reimer, D. Meier, M. Bovender, L. Helmich, J. Dreessen, J. Krieft, A. S. Shestakov, C. H. Back, J. Schmalhorst, A. Hütten, G. Reiss, and T. Kuschel. Quantitative separation of the anisotropic magnetothermopower and planar Nernst effect by the rotation of an in-plane thermal gradient. *Scientific Reports*, 7(1):40586, Jan 2017.

[15] S. Bhatti, R. Sbiaa, A. Hirohata, H. Ohno, S. Fukami, and S.N. Piramanayagam. Spintronics based random access memory: a review. *Materials Today*, 20(9):530–548, Nov 2017.

[16] A. Neubauer, C. Pfleiderer, B. Binz, A. Rosch, R. Ritz, P. G. Niklowitz, and P. Böni. Topological Hall Effect in the *A* Phase of MnSi. *Physical Review Letters*, 102(18):186602, May 2009.

[17] S. Muhlbauer, B. Binz, F. Jonietz, C. Pfleiderer, A. Rosch, A. Neubauer, R. Georgii, and P. Boni. Skyrmion Lattice in a Chiral Magnet. *Science*, 323(5916):915–919, Feb 2009.

[18] A. Fert, N. Reyren, and V. Cros. Magnetic skyrmions: advances in physics and

potential applications. *Nature Reviews Materials*, 2(7):17031, Jun 2017.

[19] R. Tomasello, E. Martinez, R. Zivieri, L. Torres, M. Carpentieri, and G. Finocchio. A strategy for the design of skyrmion racetrack memories. *Scientific Reports*, 4(1):6784, Oct 2014.

[20] X. Zhang, G. P. Zhao, H. Fangohr, J. P. Liu, W. X. Xia, J. Xia, and F. J. Morvan. Skyrmion-skyrmion and skyrmion-edge repulsions in skyrmion-based racetrack memory. *Scientific Reports*, 5(1):7643, Jan 2015.

[21] K. Everschor-Sitte, J. Masell, R. M. Reeve, and M. Kläui. Perspective: Magnetic skyrmions—Overview of recent progress in an active research field. *Journal of Applied Physics*, 124(24):240901, Dec 2018.

[22] X. Zhang, M. Ezawa, and Y. Zhou. Magnetic skyrmion logic gates: conversion, duplication and merging of skyrmions. *Scientific Reports*, 5(1):9400, Mar 2015.

[23] C. Moreau-Luchaire, C. Moutafis, N. Reyren, J. Sampaio, C. A. F. Vaz, N. Van Horne, K. Bouzehouane, K. Garcia, C. Deranlot, P. Warnicke, P. Wohlhüter, J.-M. George, M. Weigand, J. Raabe, V. Cros, and A. Fert. Additive interfacial chiral interaction in multilayers for stabilization of small individual skyrmions at room temperature. *Nature Nanotechnology*, 11(5):444–448, Jan 2016.

[24] W. Jiang, P. Upadhyaya, W. Zhang, G. Yu, M. B. Jungfleisch, F. Y. Fradin, J. E. Pearson, Y. Tserkovnyak, K. L. Wang, O. Heinonen, S. G. E. te Velthuis, and A. Hoffmann. Blowing magnetic skyrmion bubbles. *Science*, 349(6245):283–286, Jun 2015.

[25] S. Woo, K. Litzius, B. Krüger, M. Im, L. Caretta, K. Richter, M. Mann, A. Krone, R. M. Reeve, M. Weigand, P. Agrawal, I. Lemesh, M. Mawass, P. Fischer, M. Kläui, and G. S. D. Beach. Observation of room-temperature magnetic skyrmions and their current-driven dynamics in ultrathin metallic ferromagnets. *Nature Materials*, 15(5):501–506, Feb 2016.

[26] W. Legrand, D. Maccariello, N. Reyren, K. Garcia, C. Moutafis, C. Moreau-Luchaire, S. Collin, K. Bouzehouane, V. Cros, and A. Fert. Room-Temperature Current-Induced Generation and Motion of sub-100 nm Skyrmions. *Nano Letters*, 17(4):2703–2712, Apr 2017.

[27] F. Büttner, I. Lemesh, M. Schneider, B. Pfau, C. M. Günther, P. Hessing, J. Geil-

hufe, L. Caretta, D. Engel, B. Krüger, J. Viefhaus, S. Eisebitt, and G. S. D. Beach. Field-free deterministic ultrafast creation of magnetic skyrmions by spin–orbit torques. *Nature Nanotechnology*, 12(11):1040–1044, Oct 2017.

[28] D. Maccariello, W. Legrand, N. Reyren, K. Garcia, K. Bouzehouane, S. Collin, V. Cros, and A. Fert. Electrical detection of single magnetic skyrmions in metallic multilayers at room temperature. *Nature Nanotechnology*, 13(3):233–237, Jan 2018.

[29] K. Zeissler, S. Finizio, K. Shahbazi, J. Massey, F. Al Ma'Mari, D. M. Bracher, A. Kleibert, M. C. Rosamond, E. H. Linfield, T. A. Moore, J. Raabe, G. Burnell, and C. H. Marrows. Discrete Hall resistivity contribution from Néel skyrmions in multilayer nanodiscs. *Nature Nanotechnology*, 13(12):1161–1166, Oct 2018.

[30] I. Lemesh, K. Litzius, M. Böttcher, P. Bassirian, N. Kerber, D. Heinze, J. Zázvorka, F. Büttner, L. Caretta, M. Mann, M. Weigand, S. Finizio, J. Raabe, M. Im, H. Stoll, G. Schütz, B. Dupé, M. Kläui, and G. S. D. Beach. Current-Induced Skyrmion Generation through Morphological Thermal Transitions in Chiral Ferromagnetic Heterostructures. *Advanced Materials*, 30(49):1805461, Oct 2018.

[31] M. Raju, A. Yagil, A. Soumyanarayanan, A. K. C. Tan, A. Almoalem, F. Ma, O. M. Auslaender, and C. Panagopoulos. The evolution of skyrmions in Ir/Fe/Co/Pt multilayers and their topological Hall signature. *Nature Communications*, 10(1):696, Mar 2019.

[32] W. Jiang, X. Zhang, G. Yu, W. Zhang, X. Wang, M. Benjamin Jungfleisch, John E. Pearson, X. Cheng, O. Heinonen, K. L. Wang, Y. Zhou, A. Hoffmann, and Suzanne G. E. te Velthuis. Direct observation of the skyrmion Hall effect. *Nature Physics*, 13(2):162–169, Sep 2016.

[33] K. Litzius, I. Lemesh, B. Krüger, P. Bassirian, L. Caretta, K. Richter, F. Büttner, K. Sato, O. A. Tretiakov, J. Förster, R. M. Reeve, M. Weigand, I. Bykova, H. Stoll, G. Schütz, G. S. D. Beach, and M. Kläui. Skyrmion Hall effect revealed by direct time-resolved X-ray microscopy. *Nature Physics*, 13(2):170–175, Dec 2016.

[34] Y. Shiomi, N. Kanazawa, K. Shibata, Y. Onose, and Y. Tokura. Topological Nernst effect in a three-dimensional skyrmion-lattice phase. *Physical Review B*,

154

88(6):064409, Aug 2013.

[35] Y. Hirokane, Y. Tomioka, Y. Imai, A. Maeda, and Y. Onose. Longitudinal and transverse thermoelectric transport in MnSi. *Physical Review B*, 93(1):014436, Jan 2016.

[36] R. Schlitz, P. Swekis, A. Markou, H. Reichlova, M. Lammel, J. Gayles, A. Thomas, K. Nielsch, C. Felser, and S. T. B. Goennenwein. All Electrical Access to Topological Transport Features in Mn1.8PtSn Films. *Nano Letters*, 19(4):2366–2370, Mar 2019.

[37] R. Iguchi, S. Kasai, K. Koshikawa, N. Chinone, S. Suzuki, and K. Uchida. Thermoelectric microscopy of magnetic skyrmions. *Scientific Reports*, 9(1):18443, Dec 2019.

[38] Y. P. Mizuta and F. Ishii. Large anomalous Nernst effect in a skyrmion crystal. *Scientific Reports*, 6(1):28076, Jun 2016.

[39] B. D. Cullity and C. D. Graham. *Introduction to Magnetic Materials*. John Wiley & Sons, Inc., New Jersey, 2008.

[40] R. Handley. *Modern magnetic materials: principles and applications*. Wiley, New York, 2000.

[41] Stöhr and Siegmann. *Magnetism*. Springer-Verlag Berlin Heidelberg, Heidelberg, 2006.

[42] S. Blundell. *Magnetism in Condensed Matter*. Oxford University Press, Oxford, 2001.

[43] G. Zhao J. P. Liu, Z. Zhang. *Skyrmions*. Taylor and Francis Ltd, Boca Raton, 2020.

[44] Niklas Liebing. *Thermoelektrische effekte in Magnetischen Tunnelbarrieren*. PhD thesis, Gottfried Wilhelm Leibniz Universität Hannover, 2015.

[45] A. Hubert and R. Schäfer. *Magnetic Domains*. Springer-Verlag Berlin Heidelberg, Heidelberg, 1998.

[46] M. T. Johnson, P. J. H. Bloemen, F. J. A. den Broeder, and J. J. de Vries. Magnetic anisotropy in metallic multilayers. *Reports on Progress in Physics*,

155

59(11):1409–1458, Nov 1996.

[47] S. Mark, P. Dürrenfeld, K. Pappert, L. Ebel, K. Brunner, C. Gould, and L. W. Molenkamp. Fully Electrical Read-Write Device Out of a Ferromagnetic Semiconductor. *Physical Review Letters*, 106(5):057204, Jan 2011.

[48] A. H. MacDonald, P. Schiffer, and N. Samarth. Ferromagnetic semiconductors: moving beyond (Ga,Mn)As. *Nature Materials*, 4(3):195–202, Mar 2005.

[49] T. Dietl. Zener Model Description of Ferromagnetism in Zinc-Blende Magnetic Semiconductors. *Science*, 287(5455):1019–1022, Feb 2000.

[50] E. Bhatia, Z. H. Barber, I. J. Maasilta, and K. Senapati. Domain wall induced modulation of low field H-T phase diagram in patterned superconductor-ferromagnet stripes. *AIP Advances*, 9(4):045107, Apr 2019.

[51] M. Kläui. Head-to-head domain walls in magnetic nanostructures. *Journal of Physics: Condensed Matter*, 20(31):313001, Jul 2008.

[52] O. Boulle, G. Malinowski, and M. Kläui. Current-induced domain wall motion in nanoscale ferromagnetic elements. *Materials Science and Engineering: R: Reports*, 72(9):159–187, Sep 2011.

[53] P. J. Metaxas, J. P. Jamet, A. Mougin, M. Cormier, J. Ferré, V. Baltz, B. Rodmacq, B. Dieny, and R. L. Stamps. Creep and Flow Regimes of Magnetic Domain-Wall Motion in Ultrathin Pt/Co/Pt Films with Perpendicular Anisotropy. *Physical Review Letters*, 99(21):217208, Nov 2007.

[54] N. L. Schryer and L. R. Walker. The motion of 180° domain walls in uniform dc magnetic fields. *Journal of Applied Physics*, 45(12):5406–5421, Dec 1974.

[55] A. Fert, V. Cros, and J. Sampaio. Skyrmions on the track. *Nature Nanotechnology*, 8(3):152–156, Mar 2013.

[56] T. H. R. Skyrme. A non-linear field theory. *Proceedings of the Royal Society of London A: Mathematical, Physical and Engineering Sciences*, 260(1300):127–138, Feb 1961.

[57] G. Finocchio, F. Büttner, R. Tomasello, M. Carpentieri, and M. Kläui. Magnetic skyrmions: from fundamental to applications. *Journal of Physics D: Applied Physics*, 49(42):423001, Sep 2016.

[58] R. Tomasello, K. Y. Guslienko, M. Ricci, A. Giordano, J. Barker, M. Carpentieri, O. Chubykalo-Fesenko, and G. Finocchio. Origin of temperature and field dependence of magnetic skyrmion size in ultrathin nanodots. *Physical Review B*, 97(6):060402, Feb 2018.

[59] F. Büttner, I. Lemesh, and G. S. D. Beach. Theory of isolated magnetic skyrmions: From fundamentals to room temperature applications. *Scientific Reports*, 8(1):4464, Mar 2018.

[60] A. Bernand-Mantel, L. Camosi, A. Wartelle, N. Rougemaille, M. Darques, and L. Ranno. The skyrmion-bubble transition in a ferromagnetic thin film. *SciPost Physics*, 4(5):27, May 2018.

[61] W. Legrand, N. Ronceray, N. Reyren, D. Maccariello, V. Cros, and A. Fert. Modeling the Shape of Axisymmetric Skyrmions in Magnetic Multilayers. *Physical Review Applied*, 10(6):064042, Dec 2018.

[62] A. Hrabec, J. Sampaio, M. Belmeguenai, I. Gross, R. Weil, S. M. Chérif, A. Stashkevich, V. Jacques, A. Thiaville, and S. Rohart. Current-induced skyrmion generation and dynamics in symmetric bilayers. *Nature Communications*, 8(1):15765, Jun 2017.

[63] L. Gravier, S. Serrano-Guisan, F. Reuse, and J. Ansermet. Thermodynamic description of heat and spin transport in magnetic nanostructures. *Physical Review B*, 73(2):024419, Jan 2006.

[64] F. L. Bakker, A. Slachter, J. P. Adam, and B. J. van Wees. Interplay of Peltier and Seebeck Effects in Nanoscale Nonlocal Spin Valves. *Physical Review Letters*, 105(13):136601, Sep 2010.

[65] F. L. Bakker, J. Flipse, and B. J. van Wees. Nanoscale temperature sensing using the Seebeck effect. *Journal of Applied Physics*, 111(8):084306, Apr 2012.

[66] H. Callen. *Thermodynamics and an introduction to thermostatistics*. Wiley, New York, 1985.

[67] William T. XIX. On the electro-dynamic qualities of metals:—Effects of magnetization on the electric conductivity of nickel and of iron. *Proceedings of the Royal Society of London*, 8:546–550, Dec 1857.

[68] J. Smit. Magnetoresistance of ferromagnetic metals and alloys at low tempera-

tures. *Physica*, 17(6):612–627, Jun 1951.

[69] N. F. Mott. The electrical conductivity of transition metals. *Proceedings of the Royal Society of London. Series A - Mathematical and Physical Sciences*, 153(880):699–717, Feb 1936.

[70] A. Fert and I. A. Campbell. Two-Current Conduction in Nickel. *Physical Review Letters*, 21(16):1190–1192, Oct 1968.

[71] N. Nagaosa, J. Sinova, S. Onoda, A. H. MacDonald, and N. P. Ong. Anomalous Hall effect. *Reviews of Modern Physics*, 82(2):1539–1592, May 2010.

[72] C. Chang and M. Li. Quantum anomalous Hall effect in time-reversal-symmetry breaking topological insulators. *Journal of Physics: Condensed Matter*, 28(12):123002, Mar 2016.

[73] J. E. Wegrowe, H. J. Drouhin, and D. Lacour. Anisotropic magnetothermal transport and spin Seebeck effect. *Physical Review B*, 89(9):094409, Mar 2014.

[74] L. Onsager. Reciprocal Relations in Irreversible Processes. I. *Physical Review*, 37(4):405–426, Feb 1931.

[75] L. Onsager. Reciprocal Relations in Irreversible Processes. II. *Physical Review*, 38(12):2265–2279, Dec 1931.

[76] J. Banhart and H. Ebert. First-Principles Theory of Spontaneous-Resistance Anisotropy and Spontaneous Hall Effect in Disordered Ferromagnetic Alloys. *Europhysics Letters (EPL)*, 32(6):517–522, Nov 1995.

[77] T. J. Seebeck. Ueber die magnetische Polarisation der Metalle und Erze durch Temperaturdifferenz. *Annalen der Physik*, 82(3):253–286, Mar 1826.

[78] O. Boffoué, A. Jacquot, A. Dauscher, B. Lenoir, and M. Stölzer. Experimental setup for the measurement of the electrical resistivity and thermopower of thin films and bulk materials. *Review of Scientific Instruments*, 76(5):053907, May 2005.

[79] J. Martin, T. Tritt, and C. Uher. High temperature Seebeck coefficient metrology. *Journal of Applied Physics*, 108(12):121101, Dec 2010.

[80] J. de Boor and E. Müller. Data analysis for Seebeck coefficient measurements.

158

Review of Scientific Instruments, 84(6):065102, Jun 2013.

[81] W. Thomson. 4. On a Mechanical Theory of Thermo-Electric Currents. *Proceedings of the Royal Society of Edinburgh*, 3:91–98, Jun 1857.

[82] J. Sakurai, M. Horie, S. Araki, H. Yamamoto, and T. Shinjo. Magnetic Field Effects on Thermopower of Fe/Cr and Cu/Co/Cu/Ni(Fe) Multilayers. *Journal of the Physical Society of Japan*, 60(8):2522–2525, Aug 1991.

[83] L. Gravier, A. Fábián, A. Rudolf, A. Cachin, J. E. Wegrowe, and J. Ph. Ansermet. Spin-dependent thermopower in Co/Cu multilayer nanowires. *Journal of Magnetism and Magnetic Materials*, 271(2-3):153–158, May 2004.

[84] von L. Nordheim and C.J. Gorter. Bemerkungen über Thermokraft und Widerstand. *Physica*, 2(1-12):383–390, Jan 1935.

[85] D. Xiao, Y. Yao, Z. Fang, and Q. Niu. Berry-Phase Effect in Anomalous Thermoelectric Transport. *Physical Review Letters*, 97(2):026603, Jul 2006.

[86] H. Hopster and H. P. Oepen, editors. *Magnetic Microscopy of Nanostructures*. Springer-Verlag Berlin Heidelberg, Heidelberg, 2005.

[87] M. Faraday and W. Collin. On the magnetization of light and the illumination of magnetic lines of force. *The Royal Society*, 1846.

[88] J. Kerr. XXIV. On reflection of polarized light from the equatorial surface of a magnet. *The London, Edinburgh, and Dublin Philosophical Magazine and Journal of Science*, 5(30):161–177, Mar 1878.

[89] J. McCord. Progress in magnetic domain observation by advanced magneto-optical microscopy. *Journal of Physics D: Applied Physics*, 48(33):333001, Jul 2015.

[90] W. Rave, R. Schäfer, and A. Hubert. Quantitative observation of magnetic domains with the magneto-optical Kerr effect. *Journal of Magnetism and Magnetic Materials*, 65(1):7–14, Feb 1987.

[91] G. Binnig, H. Rohrer, Ch. Gerber, and E. Weibel. Surface Studies by Scanning Tunneling Microscopy. *Physical Review Letters*, 49(1):57–61, Jul 1982.

[92] C. F. Quate G. Binnig and Ch. Gerber. Atomic Force Microscope. *Physical*

Review Letters, 56(9):930–933, Mar 1986.

[93] B. Voigtländer. *Scanning Probe Microscopy.* Springer-Verlag Berlin Heidelberg, Heidelberg, 2015.

[94] P. C. Braga and D. Ricci. *Atomic Force Microscopy.* Humana Press, New York, 2003.

[95] E. Meyer, H. J. Hug, and R. Bennewitz. *Scanning Probe Microscopy.* Springer-Verlag Berlin Heidelberg, Heidelberg, 2004.

[96] S. Porthun, L. Abelmann, and C. Lodder. Magnetic force microscopy of thin film media for high density magnetic recording. *Journal of Magnetism and Magnetic Materials*, 182(1-2):238–273, Feb 1998.

[97] Y. Martin and H. K. Wickramasinghe. Magnetic imaging by "force microscopy" with 1000 Å resolution. *Appl. Phys. Lett.*, 50(20):1455–1457, May 1987.

[98] O. Kazakova, R. Puttock, C. Barton, H. Corte-León, M. Jaafar, V. Neu, and A. Asenjo. Frontiers of magnetic force microscopy. *Journal of Applied Physics*, 125(6):060901, Feb 2019.

[99] Digital Instruments. *Magnetic Force Microscopy*, Support Note No. 229, Rev. B. edition, 1996.

[100] S. N. Magonov, V. Elings, and M. H. Whangbo. Phase imaging and stiffness in tapping-mode atomic force microscopy. *Surface Science*, 375(2-3):L385–L391, Apr 1997.

[101] M. Whangbo, G. Bar, and R. Brandsch. Description of phase imaging in tapping mode atomic force microscopy by harmonic approximation. *Surface Science*, 411(1-2):L794–L801, Aug 1998.

[102] K. Y. Yasumura, T. D. Stowe, E. M. Chow, T. Pfafman, T. W. Kenny, B. C. Stipe, and D. Rugar. Quality factors in micron- and submicron-thick cantilevers. *Journal of Microelectromechanical Systems*, 9(1):117–125, Mar 2000.

[103] J. Schwenk, M. Marioni, S. Romer, N. R. Joshi, and H. J. Hug. Non-contact bimodal magnetic force microscopy. *Applied Physics Letters*, 104(11):112412, Mar 2014.

[104] H. J. Hug, B. Stiefel, P. J. A. van Schendel, A. Moser, R. Hofer, S. Martin, H. J. Güntherodt, S. Porthun, L. Abelmann, J. C. Lodder, G. Bochi, and R. C. O'Handley. Quantitative magnetic force microscopy on perpendicularly magnetized samples. *Journal of Applied Physics*, 83(11):5609–5620, Jun 1998.

[105] P. J. A. van Schendel, H. J. Hug, B. Stiefel, S. Martin, and H. J. Güntherodt. A method for the calibration of magnetic force microscopy tips. *Journal of Applied Physics*, 88(1):435–445, Jul 2000.

[106] X. Hu, G. Dai, S. Sievers, A. Fernández Scarioni, V. Neu, M. Bieler, and H. W. Schumacher. Uncertainty Analysis of Stray Field Measurements by Quantitative Magnetic Force Microscopy. *IEEE Transactions on Instrumentation and Measurement*, pages 1–1, May 2020.

[107] X. Hu, G. Dai, S. Sievers, A. Fernández-Scarioni, H. Corte-León, R. Puttock, C. Barton, O. Kazakova, M. Ulvr, P. Klapetek, M. Havlíček, D. Nečas, Y. Tang, V. Neu, and H. W. Schumacher. Round robin comparison on quantitative nanometer scale magnetic field measurements by magnetic force microscopy. *Journal of Magnetism and Magnetic Materials*, 511:166947, Oct 2020.

[108] J. Schwenk. *Multi-modal and quantitative Magnetic Force Microscopy*. PhD thesis, Universität Basel, 2016.

[109] P. C. Hansen. The L-curve and its use in the numerical treatment of inverse problems. In *Invite Computational Inverse Problems in Electrocardiology*. WIT Press, Jan 2000.

[110] K. Uchida, S. Takahashi, K. Harii, J. Ieda, W. Koshibae, K. Ando, S. Maekawa, and E. Saitoh. Observation of the spin Seebeck effect. *Nature*, 455(7214):778–781, Oct 2008.

[111] K. Uchida, T. Ota, K. Harii, S. Takahashi, S. Maekawa, Y. Fujikawa, and E. Saitoh. Spin-Seebeck effects in films. *Solid State Communications*, 150(11-12):524–528, Mar 2010.

[112] K. Uchida, H. Adachi, T. Ota, H. Nakayama, S. Maekawa, and E. Saitoh. Observation of longitudinal spin-Seebeck effect in magnetic insulators. *Applied Physics Letters*, 97(17):172505, Oct 2010.

[113] K. Uchida, M. Ishida, T. Kikkawa, A. Kirihara, T. Murakami, and E. Saitoh.

161

Longitudinal spin Seebeck effect: from fundamentals to applications. *Journal of Physics: Condensed Matter*, 26(34):343202, Aug 2014.

[114] S. Bosu, Y. Sakuraba, K. Uchida, K. Saito, T. Ota, E. Saitoh, and K. Takanashi. Spin Seebeck effect in thin films of the Heusler compound Co2MnSi. *Physical Review B*, 83(22):224401, Jun 2011.

[115] C. M. Jaworski, J. Yang, S. Mack, D. D. Awschalom, J. P. Heremans, and R. C. Myers. Observation of the spin-Seebeck effect in a ferromagnetic semiconductor. *Nature Materials*, 9(11):898–903, Sep 2010.

[116] K. Uchida, J. Xiao, H. Adachi, J. Ohe, S. Takahashi, J. Ieda, T. Ota, Y. Kajiwara, H. Umezawa, H. Kawai, G. E. W. Bauer, S. Maekawa, and E. Saitoh. Spin Seebeck insulator. *Nature Materials*, 9(11):894–897, Sep 2010.

[117] D. Meier, D. Reinhardt, M. Schmid, C. H. Back, J. M. Schmalhorst, T. Kuschel, and G. Reiss. Influence of heat flow directions on Nernst effects in Py/Pt bilayers. *Physical Review B*, 88(18):184425, Nov 2013.

[118] A. B. Oliveira, S. M. Rezende, and A. Azevedo. Magnetization reversal in permalloy ferromagnetic nanowires investigated with magnetoresistance measurements. *Physical Review B*, 78(2):024423, Jul 2008.

[119] T. Böhnert, A. C. Niemann, A. Michel, S. Bäßler, J. Gooth, B. G. Tóth, K. Neuróhr, L. Péter, I. Bakonyi, V. Vega, V. M. Prida, and K. Nielsch. Magnetothermopower and magnetoresistance of single Co-Ni/Cu multilayered nanowires. *Physical Review B*, 90(16):165416, Oct 2014.

[120] A. Fernández Scarioni, P. Krzysteczko, S. Sievers, X. Hu, and H. W. Schumacher. Temperature dependence of the domain wall magneto-Seebeck effect: avoiding artifacts of lead contributions. *Journal of Physics D: Applied Physics*, 51(23):234004, May 2018.

[121] K. Y. Wang, K. W. Edmonds, A. C. Irvine, G. Tatara, E. De Ranieri, J. Wunderlich, K. Olejnik, A. W. Rushforth, R. P. Campion, D. A. Williams, C. T. Foxon, and B. L. Gallagher. Current-driven domain wall motion across a wide temperature range in a (Ga,Mn)(As,P) device. *Applied Physics Letters*, 97(26):262102, Dec 2010.

[122] A. W. Rushforth, M. Wang, N. R. S. Farley, R. P. Campion, K. W. Edmonds,

C. R. Staddon, C. T. Foxon, and B. L. Gallagher. Molecular beam epitaxy grown (Ga,Mn)(As,P) with perpendicular to plane magnetic easy axis. *Journal of Applied Physics*, 104(7):073908, Aug 2008.

[123] B. Hillebrands and K. Ounadjela, editors. *Spin Dynamics in Confined Magnetic Structures I.* Springer-Verlag Berlin Heidelberg, Heidelberg, Sep 2001.

[124] G. S. D. Beach, C. Nistor, C. Knutson, M. Tsoi, and J. L. Erskine. Dynamics of field-driven domain-wall propagation in ferromagnetic nanowires. *Nature Materials*, 4(10):741–744, Sep 2005.

[125] A. Kirilyuk, J. Ferré, V. Grolier, J.P. Jamet, and D. Renard. Magnetization reversal in ultrathin ferromagnetic films with perpendicular anisotropy. *Journal of Magnetism and Magnetic Materials*, 171(1-2):45–63, Jul 1997.

[126] R. P. Cowburn, D. A. Allwood, G. Xiong, and M. D. Cooke. Domain wall injection and propagation in planar Permalloy nanowires. *Journal of Applied Physics*, 91(10):6949, May 2002.

[127] R. Mansell, A. Beguivin, D. C. M. C. Petit, A. Fernández-Pacheco, J. H. Lee, and R. P. Cowburn. Controlling nucleation in perpendicularly magnetized nanowires through in-plane shape. *Applied Physics Letters*, 107(9):092405, Aug 2015.

[128] V. Novák, K. Olejník, J. Wunderlich, M. Cukr, K. Výborný, A. W. Rushforth, K. W. Edmonds, R. P. Campion, B. L. Gallagher, J. Sinova, and T. Jungwirth. Curie Point Singularity in the Temperature Derivative of Resistivity in (Ga,Mn)As. *Physical Review Letters*, 101(7):077201, Aug 2008.

[129] A. Brataas, A. D. Kent, and H. Ohno. Current-induced torques in magnetic materials. *Nature Materials*, 11(5):372–381, Apr 2012.

[130] D. Apalkov, B. Dieny, and J. M. Slaughter. Magnetoresistive Random Access Memory. *Proceedings of the IEEE*, 104(10):1796–1830, Oct 2016.

[131] S. S. P. Parkin, M. Hayashi, and L. Thomas. Magnetic Domain-Wall Racetrack Memory. *Science*, 320(5873):190–194, Apr 2008.

[132] J. P. Adam, N. Vernier, J. Ferré, A. Thiaville, V. Jeudy, A. Lemaître, L. Thevenard, and G. Faini. Nonadiabatic spin-transfer torque in (Ga,Mn)As with perpendicular anisotropy. *Physical Review B*, 80(19):193204, Nov 2009.

[133] J. Curiale, A. Lemaître, C. Ulysse, G. Faini, and V. Jeudy. Spin Drift Velocity, Polarization, and Current-Driven Domain-Wall Motion in (Ga,Mn)(As,P). *Physical Review Letters*, 108(7):076604, Feb 2012.

[134] COMSOL Multiphysics® v. 5.4. www.comsol.com. Stockholm, Sweden.

[135] R. O. Carlson, G. A. Slack, and S. J. Silverman. Thermal Conductivity of GaAs and $GaAs_{1-x}P_x$ Laser Semiconductors. *Journal of Applied Physics*, 36(2):505–507, Feb 1965.

[136] D. Khadka, S. Karayev, and S. X. Huang. Dzyaloshinskii–Moriya interaction in Pt/Co/Ir and Pt/Co/Ru multilayer films. *Journal of Applied Physics*, 123(12):123905, Mar 2018.

[137] S. Karayev, P. D. Murray, D. Khadka, T. R. Thapaliya, K. Liu, and S. X. Huang. Interlayer exchange coupling in Pt/Co/Ru and Pt/Co/Ir superlattices. *Physical Review Materials*, 3(4):041401, Apr 2019.

[138] W. Legrand, D. Maccariello, F. Ajejas, S. Collin, A. Vecchiola, K. Bouzehouane, N. Reyren, V. Cros, and A. Fert. Room-temperature stabilization of antiferromagnetic skyrmions in synthetic antiferromagnets. *Nature Materials*, 19(1):34–42, Sep 2019.

[139] A. S. Okhotin, A. S. Pushkarskii, and V. V. Gorbachev. *Thermophysical properties of semiconductors*. Atomizdat, Moscow, 1972.

[140] C. J. Glassbrenner and Glen A. Slack. Thermal Conductivity of Silicon and Germanium from 3°K to the Melting Point. *Physical Review*, 134(4A):A1058–A1069, May 1964.

[141] B. S. Hemingway. Quartz: heat capacities from 340 to 1000 K and revised values for the thermodynamic properties. *American Mineralogist*, 72(3-4):273–279, Apr 1987.

[142] Y. S. Touloukian and E. H. Buyco. Thermophysical properties of matter - the TPRC data series. Volume 4. Specific heat - metallic elements and alloys. (Reannouncement). Data book. Technical report, Jan 1971.

[143] G. T. Furukawa, M. L. Reilly, and J. S. Gallagher. Critical Analysis of Heat—Capacity Data and Evaluation of Thermodynamic Properties of Ruthenium, Rhodium, Palladium, Iridium, and Platinum from 0 to 300K. A Survey

of the Literature Data on Osmium. *Journal of Physical and Chemical Reference Data*, 3(1):163–209, Jan 1974.

[144] P. Krzysteczko, J. Wells, A. Fernández Scarioni, Z. Soban, T. Janda, X. Hu, V. Saidl, R. P. Campion, R. Mansell, J. Lee, R. P. Cowburn, P. Nemec, O. Kazakova, J. Wunderlich, and H. W. Schumacher. Nanoscale thermoelectrical detection of magnetic domain wall propagation. *Physical Review B*, 95(22):220410, Jun 2017.

[145] M. Stier, W. Häusler, T. Posske, G. Gurski, and M. Thorwart. Skyrmion–Anti-Skyrmion Pair Creation by in-Plane Currents. *Physical Review Letters*, 118(26):267203, Jun 2017.

[146] K. Everschor-Sitte, M. Sitte, T. Valet, A. Abanov, and J. Sinova. Skyrmion production on demand by homogeneous DC currents. *New Journal of Physics*, 19(9):092001, Sep 2017.

[147] S. Finizio, K. Zeissler, S. Wintz, S. Mayr, T. Weßels, A. J. Huxtable, G. Burnell, C. H. Marrows, and J. Raabe. Deterministic Field-Free Skyrmion Nucleation at a Nanoengineered Injector Device. *Nano Letters*, 19(10):7246–7255, Sep 2019.

[148] S. Zhang, J. Zhang, Q. Zhang, C. Barton, V. Neu, Y. Zhao, Z. Hou, Y. Wen, C. Gong, O. Kazakova, W. Wang, Y. Peng, D. A. Garanin, E. M. Chudnovsky, and X. Zhang. Direct writing of room temperature and zero field skyrmion lattices by a scanning local magnetic field. *Applied Physics Letters*, 112(13):132405, Mar 2018.

[149] A. Casiraghi, H. Corte-León, M. Vafaee, F. Garcia-Sanchez, G. Durin, M. Pasquale, G. Jakob, M. Kläui, and O. Kazakova. Individual skyrmion manipulation by local magnetic field gradients. *Communications Physics*, 2(1):145, Nov 2019.

[150] M. A. Marioni, M. Penedo, M. Baćani, J. Schwenk, and H. J. Hug. Halbach Effect at the Nanoscale from Chiral Spin Textures. *Nano Letters*, 18(4):2263–2267, Mar 2018.

[151] K. Meng, A. S. Ahmed, M. Baćani, A. Mandru, X. Zhao, N. Bagués, B. D. Esser, J. Flores, D. W. McComb, H. J. Hug, and F. Yang. Observation of Nanoscale Skyrmions in SrIrO$_3$/SrRuO$_3$ Bilayers. *Nano Letters*, 19(5):3169–3175, Apr 2019.

[152] W. Legrand, J. Chauleau, D. Maccariello, N. Reyren, S. Collin, K. Bouzehouane, N. Jaouen, V. Cros, and A. Fert. Hybrid chiral domain walls and skyrmions in magnetic multilayers. *Science Advances*, 4(7), July 2018.

[153] X. S. Wang, H. Y. Yuan, and X. R. Wang. A theory on skyrmion size. *Communications Physics*, 1(1):31, Jul 2018.

[154] A. Bocdanov and A. Hubert. The Properties of Isolated Magnetic Vortices. *physica status solidi (b)*, 186(2):527–543, Dec 1994.

[155] N. Romming, A. Kubetzka, C. Hanneken, K. von Bergmann, and R. Wiesendanger. Field-Dependent Size and Shape of Single Magnetic Skyrmions. *Physical Review Letters*, 114(17):177203, May 2015.

[156] K. Zeissler, M. Mruczkiewicz, S. Finizio, J. Raabe, P. M. Shepley, A. V. Sadovnikov, S. A. Nikitov, K. Fallon, S. McFadzean, S. McVitie, T. A. Moore, G. Burnell, and C. H. Marrows. Pinning and hysteresis in the field dependent diameter evolution of skyrmions in Pt/Co/Ir superlattice stacks. *Scientific Reports*, 7(1):15125, Nov 2017.

[157] F. Tejo, A. Riveros, J. Escrig, K. Y. Guslienko, and O. Chubykalo-Fesenko. Distinct magnetic field dependence of Néel skyrmion sizes in ultrathin nanodots. *Scientific Reports*, 8(1):6280, Apr 2018.

[158] K. Manna, Y. Sun, L. Muechler, J. Kübler, and C. Felser. Heusler, Weyl and Berry. *Nature Reviews Materials*, 3(8):244–256, Jul 2018.

[159] B. Binz and A. Vishwanath. Chirality induced anomalous-Hall effect in helical spin crystals. *Physica B: Condensed Matter*, 403(5-9):1336–1340, Apr 2008.

[160] A. Soumyanarayanan, M. Raju, A. L. Gonzalez Oyarce, A. K. C. Tan, M. Im, A. P. Petrović, P. Ho, K. H. Khoo, M. Tran, C. K. Gan, F. Ernult, and C. Panagopoulos. Tunable room-temperature magnetic skyrmions in Ir/Fe/Co/Pt multilayers. *Nature Materials*, 16(9):898–904, Jul 2017.

[161] H.Y.T. Nguyen, W.P. Pratt, and J. Bass. Spin-flipping in Pt and at Co/Pt interfaces. *Journal of Magnetism and Magnetic Materials*, 361:30–33, Jun 2014.

[162] M. Isasa, E. Villamor, L. E. Hueso, M. Gradhand, and F. Casanova. Temperature dependence of spin diffusion length and spin Hall angle in Au and Pt. *Physical Review B*, 91(2):024402, Jan 2015.

[163] J. S. Blakemore. Semiconducting and other major properties of gallium arsenide. *Journal of Applied Physics*, 53(10):R123–R181, May 1982.